JETP Letters, Vol. 76, No. 3, 2002, pp. 115–118. Translated from Pis'ma v Zhurnal Éksperimental'noĭ i Teoreticheskoĭ Fiziki, Vol. 76, No. 3, 2002, pp. 147–150.

Bending of a Strong-Explosion-Induced Shock Wave around a Density Singularity (as Applied to the Remnants of Hypernovae)

V. M. Kontorovich* and S. I. Shelyag

Institute of Radioastronomy, National Academy of Sciences of Ukraine, Kharkov, 61002 Ukraine

**e-mail: vkont@ira.kharkov.ua*

Received June 19, 2002

The remnants of hypernovae, which can correspond to cosmological gamma-ray bursts, are analyzed on the basis of the Kompaneets equation in the strong explosion approximation. Exact solutions to the Kompaneets equation are obtained, and the shape of shock-wave fronts from a noncentral point explosion in a medium whose density decreases quadratically with the distance from the density singularity and tends to a constant at large distances. The bending of the shock-wave front around a density singularity is discussed. The results are compared with data on X-ray sources that can correspond to hypernovae. © *2002 MAIK "Nauka/Interperiodica".*

PACS numbers: 52.35.Tc; 98.58.Mj; 98.70.Rz; 95.30.Qd

The discovery of the cosmological nature of γ bursts [1] means that explosions that are much more powerful than supernovae (with an energy of about 10^{53} erg) can occur in the Universe.[1] In its turn, this means that, like the remnants of supernovae that exist tens of thousands of years [2], the remnants of hypernovae can exist as well [3]. In particular, objects NGC5471B and MF83 are now considered as such candidates [4, 5]. The energy release of a hypernova is so high that the shock wave, remaining strong, can reach distant stars or dense clouds of the interstellar gas. In this case, the shock wave must bend around obstacles (stars and clouds), which should be manifested in the characteristic features in the image of the supposed remnant. As an example that describes this effect and allows an exact solution for the shock-wave front in the Kompaneets approximation [6], we consider a noncentral point explosion in a spherically stratified medium whose density decreases quadratically with the distance from the density singularity (similarly to the peripheral regions of the solar wind and interstellar gas clouds) and tends to a constant corresponding to the average density of the interstellar medium. With this aim, we transform the solution of the Kompaneets equation from a planar stratified medium to a spherically stratified medium.

The Kompaneets equations for a shock-wave front in the planar stratified and spherically stratified atmospheres have the form

$$\left(\frac{\partial r}{\partial y}\right)^2 - \frac{1}{\varphi(z)}\left[\left(\frac{\partial r}{\partial z}\right)^2 + 1\right] = 0 \qquad (1a)$$

and

$$\left(\frac{\partial \chi}{\partial y}\right)^2 - \frac{1}{\Psi(R)}\left[\left(\frac{\partial \chi}{\partial R}\right)^2 + \frac{1}{R^2}\right] = 0, \qquad (1b)$$

respectively, and are related by the transformation [7]

$$z = z_0 \ln(R/a), \quad r = z_0 \chi. \qquad (2)$$

The dimensionless densities $\varphi(z)$ and $\Psi(R)$ are related as

$$\Psi(R) = \varphi(z_0 \ln(R/a))\frac{z_0^2}{R^2}. \qquad (3)$$

Correspondence is known between the solutions of the Kompaneets equation [7, 8] for an exponential density distribution in the planar case [6] and for a power density distribution in the spherical case [8]. For our case of very large distances, this correspondence is insufficient, and a solution to the Kompaneets equation in a medium whose density varies exponentially and tends to a constant for negative z is required. Using Eqs. (2) and (3) and solutions for a planar stratified medium [9] with the density distribution[2]

$$\varphi(z) = \beta e^{\alpha z} + C, \qquad (4)$$

[1] The possibility of a collimated jet ejection toward the observer is also discussed [1]. In this case, the energy of the explosion can be lower; however, the search for its remnant still remains topical.

[2] See also review [10].

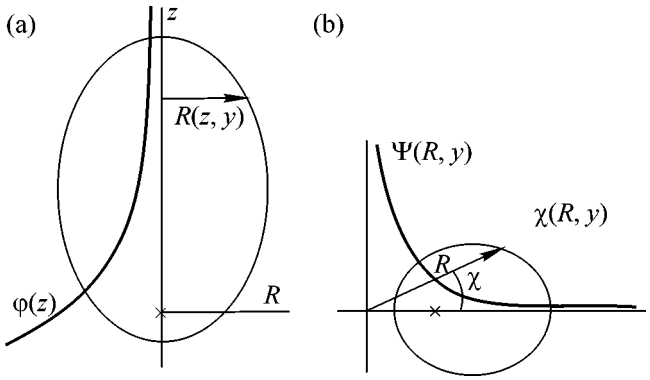

Fig. 1.

one can obtain solutions for a spherically stratified medium with the following bi-power dependence of the density on coordinates:

$$\Psi(R) = \frac{\beta z_0^2}{a^{\alpha z_0}} R^{(\alpha z_0 - 2)} + C z_0^2 \frac{1}{R^2}. \quad (5)$$

Equations (1) involve the Kompaneets "time"

$$dy = \sqrt{\frac{\lambda(\gamma^2 - 1)E}{2\rho_0}} \frac{dt}{\sqrt{V(t)}}, \quad (6)$$

where $V(t)$ is the volume of the cavity bounded by the shock-wave front, E is the explosion energy, t is the time since explosion, γ is the adiabatic index, λ is a phenomenological constant that takes into account the deviation of the pressure immediately behind the front from the average volume pressure, and ρ_0 is the medium density at the explosion point. For $\alpha z_0 = 2$, we obtain the desired coordinate dependence of the density in the form

$$\Psi(R) \propto \frac{R}{a^2} + \frac{C}{R^2}. \quad (7)$$

The general integral of Eq. (1a) [for density dependence (4)], which involves an arbitrary function $b(\xi)$, is constructed as[3]

$$\frac{\partial r}{\partial y} = \xi, \quad \frac{\partial r}{\partial z} = \pm\sqrt{\xi^2(\beta e^{\alpha z} + C) - 1},$$
$$r = \int_0^z \sqrt{\xi^2(\beta e^{\alpha z} + C) - 1}\, dz + \xi y + b(\xi), \quad (8a)$$

[3] The Kompaneets equation for the shock-wave front has the same structure as the eikonal equation or Hamilton–Jacobi equation. Therefore, the general integral is constructed by the same methods (see, e.g., [11]).

where $\xi = \xi(z, y)$ is the function calculated from the condition $\partial r/\partial \xi = 0$, i.e.,

$$\frac{\partial r}{\partial \xi} = 0 = y + \int_0^z \frac{\xi(\beta e^{\alpha z} + C)}{\sqrt{\xi^2(\beta e^{\alpha z} + C) - 1}} dz + \frac{db}{d\xi}. \quad (8b)$$

Integrating under the condition that the waves are spherical for small y and z ($b(\xi) = 0$) and applying transformation (3) to the above solutions, we find the following parametric expression for the shape of the shock-wave front with regard to the coordinate dependence of density (7) ($z_0 = 1$):

$$\chi(R, \xi) = \pm\frac{1}{\sqrt{1 - C\xi^2}}$$
$$\times\left(\arccos\sqrt{\frac{1 - C\xi^2}{\xi^2\beta}} - \arccos\left(\frac{a}{R}\sqrt{\frac{1 - C\xi^2}{\xi^2\beta}}\right)\right), \quad (9)$$
$$y = (R, \xi) = \pm\frac{1}{\xi}$$
$$\times\left(\sqrt{\xi^2(\beta + C) - 1} - \sqrt{\left(\xi\frac{R}{a}\right)^2\beta + C\xi^2 - 1}\right) + \chi C\xi,$$

where the upper and lower signs correspond to the regions

$$R \le R_-, \quad \frac{1}{\beta(R/a)^2 + C} \le \xi^2 < \infty,$$
$$y = \sqrt{\beta}\left(\sqrt{1 - \left(\frac{R_-}{a}\right)^2} + C\frac{a}{R_-}\arccos\frac{R_-}{a}\right), \quad (10)$$

and

$$R \ge R_+, \quad \frac{1}{\beta + C} \le \xi^2 < \infty,$$
$$y = \sqrt{\beta}\left(\sqrt{\left(\frac{R_+}{a}\right)^2 - 1} + C\arccos\frac{a}{R_+}\right), \quad (11)$$

respectively. The boundaries of the regions $R_\pm$ follow from the condition that solutions are real and continuous. In the general case,

$$\frac{1}{\beta + C} \le \xi^2 \text{ for } \frac{R}{a} \ge 1;$$
$$\frac{1}{\beta(R/a)^2 + C} \le \xi^2 \text{ for } \frac{R}{a} \le 1.$$

In the intermediate region $R_+ \ge R \ge R_-$, the shock-wave front is described by the solution with $b(\xi) \ne 0$, where $b(\xi)$ is calculated from the condition that χ and y

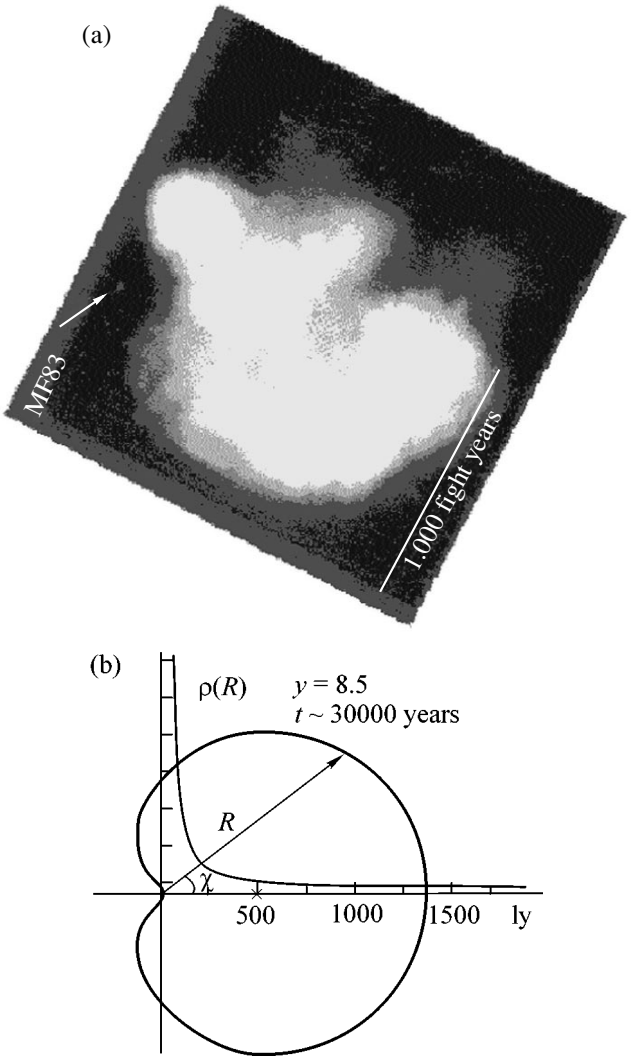

Fig. 2. (a) Image of the supposed remnant of the MF83 hypernova [13]; the arrow indicates an object that can correspond to the density singularity. (b) Calculated shape of the shock-wave front. The origin of coordinates corresponds to the density singularity. The shock-wave front bends around the density singularity. The cross is the explosion point located at a distance of 500 light years.

are continuous at the boundary R_- (cf. discussion in [7, 9]):

$$\xi(R,\xi) = \frac{1}{\sqrt{1-C\xi^2}} \times\left(\arccos\left(\frac{a}{R}\sqrt{\frac{1-C\xi^2}{\xi^2\beta}}\right)+\arccos\sqrt{\frac{1-C\xi^2}{\xi^2\beta}}\right), \quad (12)$$

$$y(R,\xi) = \frac{1}{\xi} \times\left(\sqrt{\xi^2(\beta+C)-1}+\sqrt{\left(\xi\frac{R}{a}\right)^2\beta+C\xi^2-1}\right)+\chi C\xi.$$

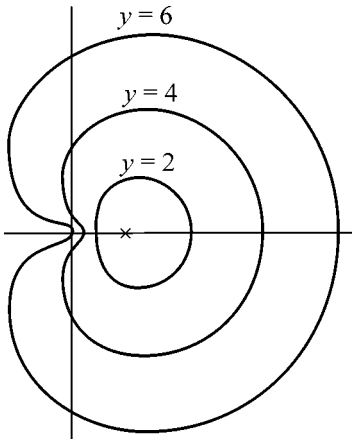

Fig. 3. Sections of the shock-wave front at three times *y*.

In the case of energies corresponding to a hypernova, an ultrarelativistic shock wave expanding with the speed of light arises at the initial stage of expansion. For this reason, solutions must be joined. This procedure is simple because both the joining fronts are spherical in the uniform area of wave propagation. The initial expansion is analyzed by using the Blandford–McKee formula [12], which describes the behavior of the ultrarelativistic shock-wave front in a uniform medium, $\Gamma^2 = E/\rho c^2 V$, where $V = (4\pi/3)(ct)^3$ is the volume bounded by the relativistic shock-wave front. In particular, the time t_{ur} taken for the ultrarelativistic stage of the expansion of the shock wave ($\Gamma^2 \geq 1$) is expressed in terms of the explosion energy; the medium density, as $t_{ur} = \sqrt[3]{3E/4\pi c^5\rho}$; and the total time taken for the expansion of the shock wave is the sum of the times of the ultrarelativistic and nonrelativistic stages:

$$t_t = t_{ur} + \sqrt{\frac{2\rho_0}{\lambda(\gamma^2-1)E}}\int_{y_{ur}}^{y}\sqrt{V(y)}dy, \quad (13)$$

where y_{ur} is the y value at which $V(y) = (4\pi/3)(ct_{ur})^3$.

Figure 2a shows the presumed remnant of an explosion of a hypernova [4, 5, 13, 14]. Figure 2b shows the shape of the shock-wave front calculated at an instant of "time" $y = 8.5$, which corresponds to the real time $t \sim 30000$ years since the explosion that had energy $E \sim 10^{48}$ J and occurred at a distance of 500 light years from the density singularity. It is seen that the shapes of shock-wave fronts bending around the singularity, which can correspond to the interstellar gas cloud with size $R \sim 0.5$ light years and density $\rho \sim 10^{-21}$ kg/m^3, are consistent with each other. Similar structures are also observed in the left-hand part of Fig. 3.[4]

[4] The self-intersection of the shock-wave front bending around a singularity was discussed in [7, 10].

This work was supported by INTAS, grant no. 00-00292.

REFERENCES

1. K. A. Postnov, Usp. Fiz. Nauk **169**, 545 (1999).
2. I. S. Shklovsky, *Supernovae* (Nauka, Moscow, 1976; Wiley, London, 1968).
3. B. Paczynski, astro-ph/9909048.
4. Q. Daniel Wang, Astrophys. J. **517**, L27 (1999).
5. S.-P. Lai *et al.*, Astrophys. J. **547**, 754 (2001).
6. A. S. Kompaneets, Dokl. Akad. Nauk SSSR **130**, 1001 (1960) [Sov. Phys. Dokl. **5**, 46 (1960)].
7. V. M. Kontorovich and S. F. Pimenov, Izv. Vyssh. Uchebn. Zaved., Radiofiz. **41**, 683 (1998).
8. D. G. Korykansky, Astrophys. J. **398**, 184 (1992).
9. S. A. Silich and P. I. Fomin, Dokl. Akad. Nauk SSSR **268**, 861 (1983) [Sov. Phys. Dokl. **28**, 157 (1983)].
10. A. D. Chernin and V. M. Kontorovich, New Astron. **5**, 327 (2000).
11. L. D. Landau and E. M. Lifshitz, *Course of Theoretical Physics*, Vol. 1: *Mechanics* (Nauka, Moscow, 1988; Pergamon, New York, 1988).
12. R. D. Blandford and C. F. McKee, Phys. Fluids **19**, 1130 (1976).
13. Energetic evidence for Hypernovae, Sky Telesc., July, 25 (1999).
14. G. S. Bisnovatyi-Kogan and S. A. Silich, Rev. Mod. Phys. **67**, 661 (1995).

Translated by R. Tyapaev

JETP Letters, Vol. 76, No. 3, 2002, pp. 119–126. From Pis'ma v Zhurnal Éksperimental'noĭ i Teoreticheskoĭ Fiziki, Vol. 76, No. 3, 2002, pp. 151–157.

Drell–Yan Representation for Vector-Meson Spin-Density Matrix Elements in Semi-Inclusive Electroproduction¶

G. I. Gakh and N. P. Merenkov

National Science Centre, Kharkov Institute of Physics and Technology, 61108 Kharkov, Ukraine

Received June 24, 2002

Polarized vector-meson production in semi-inclusive electron-nucleon scattering with longitudinally polarized electron beam has been investigated. A Drell–Yan-like representation for the spin-density matrix elements of a vector meson that takes into account the leading radiative corrections is derived. The calculations have been performed for two widely used reference systems, the Gottfried–Jackson and the helicity systems. © *2002 MAIK "Nauka/Interperiodica".*

PACS numbers: 13.60.-Le; 13.60.-Hb; 13.40.-f; 13.88.+e; 12.20.Ds

1. The investigation of the hadron final states in semi-inclusive deep-inelastic scattering (DIS) has become of topical theoretical interest, as diffractive vector-meson production at high Q^2 (Q^2 is the negative square of the virtual-photon 4-momentum) gives information on the relative contributions of hard and soft processes as well as on vacuum-exchange dynamics [1]. Measurements of exclusive vector-meson production in *ep* scattering at high energy

$$e^-(k_1) + p(p_1) \longrightarrow e^-(k_2) + V(p_2) + X(p_x) \qquad (1)$$

has led to considerable progress towards an understanding of diffraction in terms of QCD [2].

The measurement of spin observables gives very important information on the structure of strong interactions [3]. The polarization of the vector meson is experimentally accessible via decay angular distributions. In recent years, the vector-meson spin-density matrix elements in reaction (1) have been measured for the elastic electroproduction of ρ and ϕ mesons in the kinematic range $Q^2 > 2.5$ GeV^2 [4]. A discussion of recent results on the diffractive production of the vector mesons ρ^0, ϕ, and ω, reported by the H1 and ZEUS collaborations at HERA, can be found in [5]. Recently, the HERMES collaboration has found a significant (≈20%) double-spin asymmetry in vector-meson electroproduction [6]. This result is quite intriguing since it was not expected within the models of vector-meson production processes based on convenient mesonic and pomeron exchanges.

Standard data analysis requires taking into account all possible systematic uncertainties. One of the important sources of such uncertainties are the electromagnetic radiative effects caused by the physical processes that take place in higher orders of the perturbation theory with respect to electromagnetic interaction. In this paper, we calculate the model-independent QED radiative corrections (RC) by means of the electron structure function method [7]. Our approach is based on the covariant parametrization of the vector-meson spin 4-vector in terms of the 4-momenta of the particles in process (1) [8, 9] and the use of the Drell–Yan-like representation [10] in electrodynamics, which allows one to sum the leading-log model-independent RC in all orders.

2. We define the cross-section of the process (1), taking into account RC, in terms of the leptonic $L_{\mu\nu}$ and hadronic $H_{\mu\nu}$ tensor contraction

$$d\sigma = \frac{\alpha^2}{4V(2\pi)^3}\frac{L_{\mu\nu}H_{\mu\nu}}{q^4}\frac{d^3k_2}{\varepsilon_2}\frac{d^3p_2}{E_2}, \qquad (2)$$

where $V = 2k_1p_1$, ε_2 (E_2) is the energy of the scattered electron (detected vector meson), and q is the 4-momentum of the virtual photon. Note that only in the Born approximation does $q = k_1 - k_2$. The hadronic tensor can be expressed via the hadron electromagnetic current J_μ

$$H_{\mu\nu} = (2\pi)^3\sum_X \langle \tau, p_2; p_x|J_\mu(0)|p_1\rangle \times \langle \tau, p_2; p_x|J_\nu(0)|p_1\rangle^*\delta^{(4)}(q + p_1 - p_2 - p_x), \qquad (3)$$

where p_x is the total 4-momentum of the undetected hadron system, T is the polarization index of the vector meson, and the summation is done with respect to all the possible states in the undetected system X. The expressions for $H_{\mu\nu}(U)$ (the spin-independent part of the hadronic tensor) and $H_{\mu\nu}(V)$ (the part of the hadronic tensor depending on the vector polarization) can be found in [9]. The expression for $H_{\mu\nu}(T)$ (the part of

¶This article was submitted by the authors in English.

the hadronic tensor depending on the quadrupole-polarization tensor) is given in [11]. Thus, in the general case of a longitudinally polarized electron beam and an arbitrary polarization state of the vector meson produced, reaction (1) is characterized by 41 real structure functions. In the case of an unpolarized electron beam, only the symmetrical (in μ, ν indices) part of the hadronic tensor, which contains 28 structure functions (4 structure functions from $H_{\mu\nu}(U)$, 8 from $H_{\mu\nu}(V)$, and 16 from $H_{\mu\nu}(T)$), makes the contribution to the observables.

Let us represent the transition current $\gamma^* N \longrightarrow VX$ entering into Eq. (3) in the form

$$\langle \tau, p_2;\, p_x|J_\mu(0)|p_1\rangle = U_\rho^{(\tau)*}\langle p_2, p_x|J_\mu^\rho(0)|p_1\rangle, \quad (4)$$

where $U_\rho^{(\tau)}$ is the polarization 4-vector of the vector meson. We can define the following tensor

$$H_{\mu\nu}^{\rho\sigma} = (2\pi)^3\sum_X \langle p_2, p_x|J_\mu^\rho(0)|p_1\rangle \times \langle p_2, p_x|J_\nu^\sigma(0)|p_1\rangle^*\delta^{(4)}(q + p_1 - p_2 - p_x), \quad (5)$$

which will be used later for the calculation of spin-density matrix elements of the vector meson produced in reaction (1).

The hadronic tensor $H_{\mu\nu}^{\rho\sigma}$ must be constructed using 4-momenta p_1, p_2, 4-momentum of the virtual photon q, and completely antisymmetric pseudotensor $\epsilon_{\mu\nu\lambda\delta}$. It must be gauge invariant in μ, ν indices, and it does not contain $p_{2\rho}$, $p_{2\sigma}$ because of the condition $p_{2\rho}U_\rho^{(\tau)} = 0$. The P- and T-invariant form of this tensor satisfying the hermiticity condition is

$$\begin{aligned}
H_{\mu\nu}^{\rho\sigma} = \frac{1}{3}\{&-g_{\rho\sigma}[g_1\tilde g_{\mu\nu} + g_2\tilde p_{1\mu}\tilde p_{1\nu} + g_3\tilde p_{2\mu}\tilde p_{2\nu} \\
&+ g_4(\tilde p_1\tilde p_2)_{\mu\nu} + ig_5[\tilde p_1\tilde p_2]_{\mu\nu}] - \frac{i}{m}(\rho\sigma p_2 p_1)[g_6(\tilde p_1 N)_{\mu\nu} \\
&+ ig_7[\tilde p_1 N]_{\mu\nu} + g_8(\tilde p_2 N)_{\mu\nu} + ig_9[\tilde p_2 N]_{\mu\nu}] \\
&- \frac{i}{m}(\rho\sigma p_2 q)[g_{10}(\tilde p_1 N)_{\mu\nu} + ig_{11}[\tilde p_1 N]_{\mu\nu} + g_{12}(\tilde p_2 N)_{\mu\nu} \\
&+ ig_{13}[\tilde p_2 N]_{\mu\nu} - \frac{i}{m}(\rho\sigma p_2 N)[g_{14}\tilde g_{\mu\nu} + g_{15}\tilde p_{1\mu}\tilde p_{1\nu} \\
&+ g_{16}\tilde p_{2\mu}\tilde p_{2\nu} + g_{17}(\tilde p_1\tilde p_2)_{\mu\nu} + ig_{18}[\tilde p_1\tilde p_2]_{\mu\nu}] \\
&+ \left[q_\rho q_\sigma - \frac{1}{3}g_{\rho\sigma}\left(q^2 - \frac{(p_2 q)^2}{m^2}\right)\right][g_{19}\tilde g_{\mu\nu} + g_{20}\tilde p_{1\mu}\tilde p_{1\nu} \\
&+ g_{21}\tilde p_{2\mu}\tilde p_{2\nu} + g_{22}(\tilde p_1\tilde p_2)_{\mu\nu} + ig_{23}[\tilde p_1\tilde p_2]_{\mu\nu}] \\
&+ \left[p_{1\rho}p_{1\sigma} - \frac{1}{3}g_{\rho\sigma}\left(M^2 - \frac{(p_1 p_2)^2}{m^2}\right)\right][g_{24}\tilde g_{\mu\nu} + g_{25}\tilde p_{1\mu}\tilde p_{1\nu} \\
&+ g_{26}\tilde p_{2\mu}\tilde p_{2\nu} + g_{27}(\tilde p_1\tilde p_2)_{\mu\nu} + ig_{28}[\tilde p_1\tilde p_2]_{\mu\nu}] \\
&+ \left[p_{1\rho}q_\sigma + p_{1\sigma}q_\rho - \frac{2}{3}g_{\rho\sigma}\left(qp_1 - \frac{p_1 p_2 p_2 q}{m^2}\right)\right] \\
&\times [g_{29}\tilde g_{\mu\nu} + g_{30}\tilde p_{1\mu}\tilde p_{1\nu} + g_{31}\tilde p_{2\mu}\tilde p_{2\nu} + g_{32}(\tilde p_1\tilde p_2)_{\mu\nu} \\
&+ ig_{33}[\tilde p_1\tilde p_2]_{\mu\nu}] + (qN)_{\rho\sigma}[g_{34}(\tilde p_1 N)_{\mu\nu} + ig_{35}[\tilde p_1 N]_{\mu\nu} \\
&+ g_{36}(\tilde p_2 N)_{\mu\nu} + ig_{37}[\tilde p_2 N]_{\mu\nu}] \\
&+ (p_1 N)_{\rho\sigma}[g_{38}(\tilde p_1 N)_{\mu\nu} + ig_{39}[\tilde p_1 N]_{\mu\nu} \\
&+ g_{40}(\tilde p_2 N)_{\mu\nu} + ig_{41}[\tilde p_2 N]_{\mu\nu}]\}, \quad (6)
\end{aligned}$$

$$N_\mu = \epsilon_{\mu\nu\lambda\delta}p_{1\nu}p_{2\lambda}q_\delta = (\mu p_1 p_2 q),$$

$$(ab)_{\mu\nu} = a_\mu b_\nu + a_\nu b_\mu,$$

$$[ab]_{\mu\nu} = a_\mu b_\nu - a_\nu b_\mu, \quad \tilde g_{\mu\nu} = g_{\mu\nu} - \frac{q_\mu q_\nu}{q^2},$$

$$\tilde p_{i\mu} = p_{i\mu} - \frac{(qp_i)q_\mu}{q^2}, \quad i = 1, 2,$$

where m (M) is the vector-meson (target) mass and g_i (i = 1–41) are the real structure functions that describe in a model-independent way the process of vector-meson leptoproduction by longitudinally polarized electron beam. These functions depend, in general, on four invariants which can be taken as q^2, (qp_1), (qp_2), and (p_1p_2).

The hadronic tensors $H_{\mu\nu}$ and $H_{\mu\nu}^{\rho\sigma}$ are connected by the relation $H_{\mu\nu} = \rho_{\sigma\rho}H_{\mu\nu}^{\rho\sigma}$, where $\rho_{\sigma\rho}$ is the covariant spin-density matrix for the spin-one particle, which in our case is

$$\rho_{\mu\nu} = -\left(g_{\mu\nu} - \frac{p_{2\mu}p_{2\nu}}{m^2}\right) - \frac{3i}{2m}\epsilon_{\mu\nu\rho\sigma}s_\rho p_{2\sigma} + 3Q_{\mu\nu}, \quad (7)$$
$$Q_{\mu\nu} = Q_{\nu\mu}, \quad Q_{\mu\mu} = 0, \quad p_{2\mu}Q_{\mu\nu} = 0,$$

where s_ρ is the 4-vector of the vector polarization of the vector meson ($s^2 = -1$, $sp_2 = 0$) and $Q_{\mu\nu}$ is its quadrupole-polarization tensor. The parametrization of the hadronic tensor $H_{\mu\nu}^{\rho\sigma}$ is chosen so as to obtain previously used hadronic tensor $H_{\mu\nu}$ [9, 11] when convoluting hadronic tensor $H_{\mu\nu}^{\rho\sigma}$ with tensor $\rho_{\sigma\rho}$. At this point, we follow [12] very closely, where the matrix elements of the vector meson in reaction $e^+e^- \longrightarrow VX$ have been studied.

The model-independent RC exhibit themselves by means of the corrections to the leptonic tensor. The

expression for this tensor with regard to RC can be found in [8].

The spin-density matrix of the vector meson produced in reaction (1) can be defined as

$$\sigma^U\rho_{mn} = \frac{\alpha^2}{4V(2\pi)^3}\frac{L_{\mu\nu}H^{\rho\sigma}_{\mu\nu}U^{(m)*}_\rho U^{(n)}_\sigma}{q^4}\frac{d^3k_2}{\varepsilon_2}\frac{d^3p_2}{E_2}, \quad (8)$$

where σ^U is the differential cross section of reaction (1) for the case of all (except electron beam) unpolarized particles, and the 4-vectors $U^{(m)}_\rho$, $m = +1, -1, 0$, characterize the production of the vector meson with definite helicity m (in its rest system). In this system, the vector meson has three polarization states and its production can be completely characterized by the spin-density matrix ρ_{mn}, which may be obtained from experiment. It is convenient to discuss the angular distribution of the vector-meson decay in two widely used reference systems which differ in their choice of spin-quantization axis (z axis): the Gottfried–Jackson system, where the z axis is the direction of the incident photon in the vector-meson rest system and the helicity system, where the z axis is equal to the direction of flight of the vector meson produced in the overall y^*N center-of-mass system [13]. Depending on the production mechanism, the spin of the vector meson may be aligned along the z axis in one of these systems [14]. Then, the system that gives the simplest description of the vector meson is (1) the Gottfried–Jackson system for t-channel helicity conservation or (2) the helicity system for s-channel helicity conservation.

Combining equations for the cross-section (2) and spin-density matrix elements (8) and using the definitions of the radiatively corrected lepton [9] and hadron tensors, we can write the following representation for the unpolarized cross section of the process (1) and for the spin-density matrix elements

$$\sigma^U = \varepsilon_2 E_2\frac{d\sigma(k_1,k_2)}{d^3k_2d^3p_2}$$

$$= \iint\frac{dx_1dx_2}{x_2^2}D(x_1)D(x_2)\hat{\varepsilon}_2E_2\frac{d\sigma^B(\hat{k}_1,\hat{k}_2)}{d^3\hat{k}_2d^3p_2}, \quad (9)$$

$$\sigma^U\rho_{mn}(k_1,k_2) = \iint\frac{dx_1(x_2)}{x_2^2}D(x_1)D(x_2)\hat{\sigma}^U_B\rho^B_{mn}(\hat{k}_1,\hat{k}_2),$$

where $\hat{k}_1 = x_1k_1$, $\hat{k}_2 = k_2/x_2$, D is the electron structure function, index B means that the corresponding quantity is calculated in the Born approximation (for details, see [9]). In the discussion of the cross section, we omit the hadron 4-momenta. The cross section $\hat{\sigma}^U_B = \sigma^U_B(\hat{k}_1, \hat{k}_2)$ and $\sigma^U_B(k_1, k_2)$ can be derived substituting $\delta(x-1)$ instead of both D-functions in the first equation in (9).

In theoretical calculations, it is useful to parameterize the polarization state of the particle (specifically, the 4-vectors $U^{(m)}_\rho$) in terms of the particle 4-momenta [8, 9]. In our case, we have four 4-momenta to express any 4-vector $U^{(m)}_\rho$ in a such way that

$$U^{(m)}_\rho = U^{(m)}_\rho(k_1, k_2, p_1, p_2). \quad (10)$$

Let us imagine for a moment that the chosen parametrization on the right side of Eq. (10) is relatively stabilized by the substitution

$$k_1 \longrightarrow \hat{k}_1, \quad k_2 \longrightarrow \hat{k}_2,$$

$$U^{(m)}_\rho(k_1, k_2, p_1, p_2) = U^{(m)}_\rho(\hat{k}_1, \hat{k}_2, p_1, p_2).$$

Later, we will label this stabilized parametrization by the indices $\alpha = l, t$, and n. In this case, the expression for the spin-density matrix elements (taking into account RC) is just described by Eq. (9).

If the 4-vector $U^{(m)}_\rho$ is unstable under the above substitution, it can be expressed always in terms of a stabilized one by means of some linear combination

$$U^{(m)}_\rho(k_1, k_2, p_1, p_2) = A^{(m)}_\alpha(k_1, k_2, p_1, p_2)U^{(\alpha)}_\rho(\hat{k}_1, \hat{k}_2, p_1, p_2). \quad (11)$$

Using the last equation, we can write the master representation for the spin-density matrix elements of the vector meson produced in the process (1) in the following form:

$$\sigma^U\rho_{mn}(k_1, k_2, p_1, p_2) = A^{(m)*}_\alpha A^{(n)}_\beta\iint\frac{dx_1dx_2}{x_2^2} \times D(x_1)D(x_2)\hat{\sigma}^U_B\rho^B_{\alpha\beta}(\hat{k}_1, \hat{k}_2, p_1, p_2), \quad (12)$$

where we bear in mind the summation over indices α, $\beta = l, t, n$.

This representation is the electrodynamical analogue of the Drell–Yan equation, which is well known in QCD formula [10] and was applied earlier to calculate QED RC for various processes [9]. It is obvious that in the framework of the leading accuracy one needs to find adequate parametrizations of the stabilized 4-vectors $U^{(\alpha)}_\rho$, calculate the coefficients $A^{(m)}_\alpha$, and derive the spin-density matrix elements in the Born approximation for a given parametrization $U^{(\alpha)}_\rho$.

3. The following set of invariant variables completely describe process (1):

$$z = \frac{2p_1p_2}{V}, \quad z_{1,2} = \frac{2k_{1,2}p_2}{V}, \quad y = \frac{2p_1q}{V}, \quad x = \frac{-q^2}{2p_1q}, \quad q = k_1 - k_2. \tag{13}$$

Therefore, to calculate RC we have to find a set of stabilized axes and to write them in covariant form in terms of 4-momenta of the particles participating in the reaction. Further we will use the following stabilized set of the 4-vectors [9]:

$$S_\mu^{(l)} = \frac{zp_{2\mu} - 2\tau_2 p_{1\mu}}{md_1},$$

$$S_\mu^{(t)} = \frac{d_1^2 k_{1\mu} + (2z_1\tau_1 - z)p_{2\mu} + (2\tau_2 - zz_1)p_{1\mu}}{d_2},$$

$$S_\mu^{(n)} = \frac{2\varepsilon_{\mu\lambda\rho\sigma}k_{1\lambda}p_{1\rho}p_{2\sigma}}{d_3}, \tag{14}$$

$$d_1^2 = z^2 - 4\tau_1\tau_2, \quad d_2^2 = V\psi d_1^2, \quad \psi = zz_1 - \tau_2 - \tau_1 z_1^2,$$

$$d_3^2 = \psi V^3, \quad \tau_1 = \frac{M^2}{V}, \quad \tau_2 = \frac{m^2}{V}.$$

One can verify that the set $S_\mu^{(l,t,n)}$ remains stabilized under the scale transformation and

$$S_\mu^{(\alpha)}S_\mu^{(\beta)} = -\delta_{\alpha\beta}, \quad S_\mu^{(\alpha)}p_{2\mu} = 0, \quad \alpha, \beta = l, t, n.$$

Any vector-meson polarization 4-vector $U_\mu^{(m)}$ corresponding to a certain helicity m can be expanded over the stabilized set of the 4-vectors $S_\mu^{(\alpha)}$ ($\alpha = l, t, n$). Let us define such an expansion

$$U_\rho^{(m)} = A_l^{(m)}S_\rho^{(l)} + A_t^{(m)}S_\rho^{(t)} + A_n^{(m)}S_\rho^{(n)}. \tag{15}$$

Then the spin-density matrix elements ρ_{mn} (in the helicity representation) can be expressed in terms of the spin-density matrix elements $\rho_{\alpha\beta}$ (in the representation of the stabilized set)

$$\rho_{mn} = \sum_{\alpha,\beta} A_\alpha^{(m)*}A_\beta^{(n)}\rho_{\alpha\beta}, \quad \alpha, \beta = l, t, n, \tag{16}$$

where

$$\sigma^U\rho_{\alpha\beta} = \frac{\alpha^2}{4V(2\pi)^3}\frac{L_{\rho\sigma}H_{\rho\sigma}^{\mu\nu}S_\mu^{(\alpha)}S_\nu^{(\beta)}}{q^4}\frac{d^3k_2}{\varepsilon_2}\frac{d^3p_2}{E_2}.$$

The spin-density matrix elements in the Born approximation can be represented as

$$\rho_{ll} = \frac{1}{3H_1}\left\{H_1 + \frac{V}{12\tau_2}\left[H_3\left(3\frac{\psi_1^2}{d_1^2} - 4xy\tau_2 - (z_2 - z_1)^2\right) + 2d_1^2H_4 + 4\psi_1H_5\right]\right\},$$

$$\rho_{lt} = \frac{d_1V^2}{12d_2H_1}\left\{\frac{\psi_1}{md_1^2}\left(\eta_3H_3 - \frac{\eta}{4}d_1^2V^2G_3\right) + \frac{1}{m}\left(\eta_3H_5 - \frac{\eta}{4}d_1^2V^2G_4\right) + i(\eta G_2 + \eta_3H_2)\right\},$$

$$\rho_{ln} = \frac{V^3}{12md_1d_3H_1}\left\{\psi_1\left(\eta H_3 + \frac{\eta_3}{4}V^2G_3\right) + d_1^2\left(\eta H_5 + \frac{\eta_3}{4}V^2G_4\right) + im(\eta d_1^2H_2 - \eta_3G_2)\right\},$$

$$\rho_{tt} = \frac{1}{3H_1}\left\{H_1 - \frac{\eta\eta_3}{8\psi}V^3G_3 + \frac{V}{12\tau_2}\right. \tag{17}$$

$$\left.\times\left[H_3\left(3\frac{\tau_2\eta_3^2}{\psi d_1^2} - 4xy\tau_2 - (z_1 - z_2)^2\right) - d_1^2H_4 - 2\psi_1H_5\right]\right\},$$

$$\rho_{nn} = \frac{1}{3H_1}\left\{H_1 + \frac{\eta\eta_3}{8\psi}V^3G_3 + \frac{V}{12\tau_2}\right.$$

$$\left.\times\left[H_3\left(3\frac{\tau_2\eta^2}{\psi} - 4xy\tau_2 - (z_1 - z_2)^2\right) - d_1^2H_4 - 2\psi_1H_5\right]\right\},$$

$$\rho_{tn} = \frac{V^3}{12d_2d_3H_1}\left\{\eta\eta_3H_3 + \frac{V^2}{4}(\eta_3^2 - d_1^2\eta^2)G_3 + i\frac{\psi}{m}V(d_1^2G_1 + \psi_1G_2)\right\},$$

$$\rho_{nt} = \rho_{tn}^*, \quad \rho_{nl} = \rho_{ln}^*, \quad \rho_{tl} = \rho_{lt}^*,$$

where the following notations are used

$$H_1 = -\frac{2xy}{V}g_1 + (1 - y - xy\tau_1)g_2 + (z_1z_2 - xy\tau_2)g_3 + (z_2 + z_1(1 - y) - xyz)g_4 - \lambda\eta g_5,$$

$$H_2 = H_1(g_i \longrightarrow g_{i+13}), \quad H_3 = H_1(g_i \longrightarrow g_{i+18}),$$

$$H_4 = H_1(g_i \longrightarrow g_{i+23}), \quad H_5 = H_1(g_i \longrightarrow g_{i+28}),$$

$$G_1 = -\eta[(2-y)g_6 + (z_1+z_2)g_8] - \lambda(\eta_1 g_7 + \eta_2 g_9),$$

$$G_2 = G_1(g_i \longrightarrow g_{i+4}), \quad G_3 = G_1(g_i \longrightarrow g_{i+28}),$$

$$G_4 = G_1(g_i \longrightarrow g_{i+32}),$$

$$\eta = \mathrm{sgn}[(p_1p_2k_1k_2)]\sqrt{\frac{16}{V^4}(p_1p_2k_1k_2)^2},$$

$$(p_1p_2k_1k_2) = \epsilon_{\mu\nu\rho\sigma}p_{1\mu}p_{2\nu}k_{1\rho}k_{2\sigma},$$

$$\frac{16(p_1p_2k_1k_2)^2}{V^4} = x^2y^2(4\tau_1\tau_2 - z^2)$$

$$+ 2xy[z(z_2 + z_1(1-y)) - 2z_1z_2\tau_1 - 2(1-y)\tau_2]$$

$$-(z_2 - z_1(1-y))^2,$$

$$\eta_1 = y[z_2 - z_1(1-y) - xz(2-y) + 2x(z_1+z_2)\tau_1],$$

$$\eta_2 = (z_1 - z_2)(z_2 - z_1(1-y))$$

$$+ xyz(z_1+z_2) - 2xy(2-y)\tau_2,$$

$$\psi_1 = z(z_1 - z_2) - 2y\tau_2,$$

$$\eta_3 = -yzz_1 + 2z_1(z_1 - z_2)\tau_1 - \psi_1 - xy(z^2 - 4\tau_1\tau_2),$$

where the quantity λ is the degree of longitudinal polarization of the electron beam. One can see that the condition $\rho_{ll} + \rho_{tt} + \rho_{nn} = 1$ is satisfied.

Let us consider the two reference systems mentioned above.

The helicity system. The z axis is opposite to the direction of the system X produced in the vector-meson rest system (i.e., equal to the direction of flight of the vector meson in the overall γ^*N c.m.s.). Then, the vector-meson wave functions $U_\mu^{(m)}$ with definite helicity m can be represented as

$$U_\mu^{(0)} = \frac{1}{md}[(z + z_1 - z_2)p_{2\mu} - 2\tau_2(p_1 - q)_\mu],$$

$$d^2 = (z + z_1 - z_2)^2 - 4\tau_2[y(1-x) + \tau_1],$$

$$U_\mu^{(\pm1)} = \mp\frac{1}{\sqrt{2}}(U_\mu^{(x)} \pm iU_\mu^{(y)}), \quad U_\mu^{(y)} = \frac{\epsilon_{\mu\lambda\rho\sigma}q_\lambda p_{2\rho}p_{1\sigma}}{D},$$

$$U_\mu^{(x)} = \frac{1}{D_1}(a_1p_{1\mu} + a_2p_{2\mu} + a_3q_\mu),$$

$$D^2 = \frac{V^3}{4} \tag{18}$$

$$\times[xy(z^2 - 4\tau_1\tau_2) + yz(z_1 - z_2) - y^2\tau_2 - \tau_1(z_1 - z_2)^2],$$

$$a_1 = (z_1 - z_2)(z + z_1 - z_2) + 2y\tau_2(2x - 1),$$

$$a_2 = yz(1-2x) - (y + 2\tau_1)(z_1 - z_2),$$

$$a_3 = -z(z + z_1 - z_2) + 2\tau_2(y + 2\tau_1),$$

$$D_1^2 = -V\{\tau_1a_1^2 + \tau_2a_2^2 + ya_3(a_1 - xa_3)$$

$$+ a_2[(z_1 - z_2)a_3 + za_1]\}.$$

Then, the coefficients in the expansion of the vector-meson wave function with definite helicity over the stabilized set of the 4-vectors (see Eq. (15)) can be represented as follows:

$$A_l^{(0)} = -\frac{a_3}{dd_1}, \quad A_t^{(0)} = \frac{V\tau_2\eta_3}{mdd_2}, \quad A_n^{(0)} = \frac{V^2\tau_2\eta}{mdd_3},$$

$$A_l^{(\pm1)} = \pm4\sqrt{2}\frac{mD^2}{d_1D_1V^3},$$

$$A_t^{(\pm1)} = \pm\frac{V}{4\sqrt{2}d_2}\left(2\eta_3\frac{a_3}{D_1} \pm i\eta V\frac{d_1^2}{D}\right), \tag{19}$$

$$A_n^{(\pm1)} = \pm\frac{V^2}{4\sqrt{2}d_3}\left(2\eta\frac{a_3}{D_1} \mp iV\frac{\eta_3}{D}\right).$$

The wave functions $U_\mu^{(m)}$ have the following form in the vector-meson rest system:

$$U_\mu^{(0)} = (0, \mathbf{l}), \quad U_\mu^{(x)} = (0, \mathbf{t}), \quad U_\mu^{(y)} = (0, \mathbf{n}),$$

$$\mathbf{l} = -\frac{\mathbf{p_x}}{|\mathbf{p_x}|}, \quad \mathbf{n} = \frac{\mathbf{p_x}\times\mathbf{q}}{|\mathbf{p_x}\times\mathbf{q}|}, \tag{20}$$

$$\mathbf{t} = \frac{[\mathbf{q}\cdot\mathbf{p_x}\mathbf{p_1} - \mathbf{p_1}\cdot\mathbf{p_x}\mathbf{q}]}{|\mathbf{q}\cdot\mathbf{p_x}\mathbf{p_1} - \mathbf{p_1}\cdot\mathbf{p_x}\mathbf{q}|},$$

where $\mathbf{q}$, $\mathbf{p_1}$, and $\mathbf{p_x}$ are the momenta of the virtual photon, the target, and the undetected system X, respectively. Choosing the coordinate axes as follows: $z \parallel \mathbf{l}$, $y \parallel \mathbf{n}$, and $x \parallel \mathbf{t}$, we get for the wave functions the following expressions:

$$U_\mu^{(0)} = (0, 0, 0, 1), \quad U_\mu^{(\pm1)} = \mp\frac{1}{\sqrt{2}}(0, 1, \pm i, 0). \tag{21}$$

The Gottfried–Jackson system. In the Gottfried–Jackson system, the z axis coincides with the direction of flight of the incoming photon in the vector-meson rest system. Then, the vector-meson wave functions $U_\mu^{(m)}$ with definite helicity m can be represented as

$$U_\mu^{(0)} = \frac{1}{r}[2\tau_2q_\mu - (z_1 - z_2)p_{2\mu}],$$

$$r^2 = V\tau_2[4xy\tau_2 + (z_1 - z_2)^2],$$

$$U_\mu^{(\pm1)} = \mp\frac{1}{\sqrt{2}}(U_\mu^{(x)} \pm iU_\mu^{(y)}), \quad U_\mu^{(y)} = \frac{\epsilon_{\mu\lambda\rho\sigma}q_\lambda p_{2\rho}p_{1\sigma}}{D},$$

$$U_\mu^{(x)} = \frac{1}{R_1}(b_1 p_{1\mu} + b_2 p_{2\mu} + b_3 q_\mu),$$
$$b_1 = -(z_1 - z_2)^2 - 4xy\tau_2,$$
$$b_2 = y(z_1 - z_2 + 2xz), \quad b_3 = \psi_1,$$
$$R_1^2 = -V\{\tau_1 b_1^2 + \tau_2 b_2^2 + b_1(yb_3 + zb_2) + b_3[(z_1 - z_2)b_2 - xyb_3]\}. \tag{22}$$

Then, the coefficients in the expansion of the vector-meson wave function with definite helicity over the stabilized set of the 4-vectors (see Eq. (15)) can be represented as follows:

$$A_l^{(0)} = -\frac{V\tau_2\psi_1}{mrd_1}, \quad A_t^{(0)} = -\frac{V\tau_2\eta_3}{rd_2},$$
$$A_n^{(0)} = -\frac{V^2\tau_2\eta}{rd_3}, \quad A_l^{(\pm 1)} = \mp\frac{4\sqrt{2\tau_2}D^2}{d_1R_1V^{5/2}},$$
$$A_t^{(\pm 1)} = \pm\frac{V}{2\sqrt{2}d_2}\left\{\frac{\psi_1\eta_3}{R_1} \pm i\frac{V\eta d_1^2}{2D}\right\},$$
$$A_n^{(\pm 1)} = \pm\frac{V^2}{2\sqrt{2}d_3}\left(\eta\frac{b_3}{R_1} \mp i\frac{V\eta_3}{2D}\right). \tag{23}$$

In the vector-meson rest system, the wave functions $U_\mu^{(m)}$ (22) have the same form as given by Eq. (20). But for the Gottfried–Jackson system the vectors **l**, **n**, and **t** are

$$\mathbf{l} = \frac{\mathbf{q}}{|\mathbf{q}|}, \quad \mathbf{n} = \frac{\mathbf{p_x}\times\mathbf{q}}{|\mathbf{p_x}\times\mathbf{q}|}, \quad \mathbf{t} = \frac{[\mathbf{lp_1}\cdot\mathbf{l} - \mathbf{p_1}]}{|\mathbf{lp_1}\cdot\mathbf{l} - \mathbf{p_1}|}.$$

Choosing the coordinate axes as follows: $z \parallel \mathbf{l}$, $y \parallel \mathbf{n}$, and $x \parallel \mathbf{t}$, we get for the wave functions in the vector-meson rest system the form given by Eq. (21).

4. Let us expand the spin-density matrix elements into the terms according to the polarization state of the virtual photon. This expansion is the standard procedure when analyzing the cross section and polarization observables for inelastic lepton scattering. The form of this expansion for the case of a longitudinally polarized electron beam is

$$\sigma_B^U\rho_{mn}^B = \rho_{mn}^U + \varepsilon\cos(2\phi)\rho_{mn}^T + \varepsilon\sin(2\phi)\rho_{mn}^{TP} + \varepsilon\rho_{mn}^L + \sqrt{2\varepsilon(1+\varepsilon)}\cos\phi\rho_{mn}^I + \sqrt{2\varepsilon(1+\varepsilon)}\sin\phi\rho_{mn}^{IP} + \lambda\sqrt{1-\varepsilon^2}\rho_{mn}^{TP'} + \lambda\sqrt{2\varepsilon(1-\varepsilon)}\cos\phi\rho_{mn}^{IP'} + \lambda\sqrt{2\varepsilon(1-\varepsilon)}\sin\phi\rho_{mn}^{I}, \tag{24}$$

where $\varepsilon^{-1} = 1 - 2(\mathbf{q_L^2}/q^2)\tan^2(\theta_e/2)$ and θ_e and $\mathbf{q}_L$ are the electron scattering angle and virtual-photon 3-momentum in the laboratory system. The quantity ε represents the degree of virtual-photon linear polarization. The angle ϕ is the angle between the electron scattering plane and the plane ($\mathbf{q}$, $\mathbf{p_2}$) (vector-meson production plane). This expansion is a consequence of the one-photon exchange approximation and the validity of the conservation of the electromagnetic current describing the $\gamma^*N \longrightarrow VX$ transition and the *P*-invariance of the hadron electromagnetic interaction as well. The meaning of the indices is the following: *U* (*L*) is determined by the transverse (longitudinal) current component, *T* is caused by the transverse current component and determines the asymmetry due to the linear polarization of the virtual photon, *I* is determined by the interference of the transverse and longitudinal current components, and *P* (') means that this term is due to the vector-meson (electron beam) polarization.

For the stabilized set of 4-vectors $S_\mu^{(\alpha)}$, where $\alpha = l, t, n$, we have in the Born approximation

$$\rho_{ll}^U = \frac{N_k}{3}\times\left\{R_3 + \frac{V}{12\tau_2}\left[\left(3\frac{\psi_1^2}{d_1^2} - \psi_2\right)R_{21} + 2d_1^2R_{26} + 4\psi_1R_{31}\right]\right\},$$
$$\rho_{tt}^U = L_1 + \frac{\eta_3^2VN_k}{12\psi d_1^2}R_{21},$$
$$\rho_{nn}^U = L_1 + \frac{\eta^2VN_k}{12\psi}R_{21}, \quad \rho_{lt}^U = \rho_2N_kL_2,$$
$$\rho_{ln}^U = \rho_3N_kL_2, \quad \rho_{nt}^U = \rho_1N_kR_{21},$$
$$\rho_{\alpha\beta}^T = e_1^2\rho_{\alpha\beta}^U(e_1 = 1, g_1 = g_{19} = g_{24} = g_{29} = 0),$$
$$\rho_{\alpha\beta}^I = 2\frac{e_4\sqrt{-q^2}}{e_1q_0}\rho_{\alpha\beta}^T(g_i \longrightarrow g_{i+2}),$$
$$\rho_{ll}^{IP} = 0, \quad \rho_{tt}^{IP} = -\gamma_1\rho_1Vd_1P_{34}, \quad \rho_{nn}^{IP} = -\rho_{tt}^{IP},$$
$$\rho_{lt}^{IP} = -\gamma_1\frac{\eta Vd_1}{6d_2}L_3, \quad \rho_{ln}^{IP} = \gamma_1\frac{\eta_3V^2}{6d_1d_3}L_3,$$
$$\rho_{nt}^{IP} = \gamma_1\frac{V}{6d_1}\times\left[-\frac{i}{m}(d_1^2P_6 + \psi_1P_{10}) + \frac{V}{4\psi}(\eta_3^2 - d_1^2\eta^2)P_{34}\right],$$
$$\rho_{\alpha\beta}^{IP'} = \rho_{\alpha\beta}^{IP}(g_i \longrightarrow g_{i+1}),$$
$$\rho_{\alpha\beta}^{TP} = \rho_{\alpha\beta}^{IP}(\gamma_1 \longrightarrow \gamma_2, g_i \longrightarrow g_{i+2}, e_2 = 0, e_4 = 1),$$

$$\rho^{TP'}_{\alpha\beta} = \rho^{TP}_{\alpha\beta}(g_i \longrightarrow g_{i+1}),$$

$$\rho^{I}_{ll} = \frac{e_1\gamma_1}{3e_3}$$

$$\times\left\{V_3 + \frac{V}{12\tau_2}\left[\left(3\frac{\psi_1^2}{d_1^2} - \psi_2\right)V_{21} + 2d_1^2V_{26} + 4\psi_1V_{31}\right]\right\},$$

$$\rho^{I}_{tt} = L_4 + \gamma_1\frac{\eta_3^2Ve_1}{12\psi e_3d_1^2}V_{21}, \quad \rho^{I}_{nn} = L_4 + \gamma_1\frac{\eta^2Ve_1}{12\psi e_3}V_{21},$$

$$\rho^{I}_{lt} = \rho_2\gamma_1\frac{e_1}{e_3}L_5, \quad \rho^{I}_{ln} = \gamma_1\rho_3\frac{e_1}{e_3}L_5, \quad \rho^{I}_{nt} = \gamma_1\rho_1\frac{e_1}{e_3}V_{21},$$

$$\rho^{L}_{ll} = \frac{\gamma_3}{3}$$

$$\times\left\{Q_1 + \frac{V}{12\tau_2}\left[\left(3\frac{\psi_1^2}{d_1^2} - \psi_2\right)Q_{19} + 2d_1^2Q_{24} + 4\psi_1Q_{29}\right]\right\},$$

$$\rho^{L}_{tt} = L_6 + \gamma_3\frac{\eta_3^2V}{12\psi d_1^2}Q_{19}, \quad \rho^{L}_{nn} = L_6 + \gamma_3\frac{\eta^2V}{12\psi}Q_{19},$$

$$\rho^{L}_{lt} = \rho_2\gamma_3\left(imQ_{14} + \frac{\psi_1}{d_1^2}Q_{19} + Q_{29}\right), \qquad (25)$$

$$\rho^{L}_{ln} = \rho_3\gamma_3\left(imQ_{14} + \frac{\psi_1}{d_1^2}Q_{19} + Q_{29}\right), \quad \rho^{L}_{nt} = \gamma_3\rho_1Q_{19},$$

$$L_1 = \frac{N_k}{3}\left[R_3 - \frac{V}{12\tau_2}(\psi_2R_{21} + d_1^2R_{26} + 2\psi_1R_{31})\right],$$

$$L_2 = imR_{16} + \frac{\psi_1}{d_1^2}R_{21} + R_{31},$$

$$L_3 = -iP_{10} + \frac{V^2}{4m}(\psi_1P_{34} + d_1^2P_{38}),$$

$$L_4 = \frac{e_1\gamma_1}{3e_3}\left[V_3 - \frac{V}{12\tau_2}(\psi_1V_{21} + d_1^2V_{26} + 2\psi_1V_{31})\right],$$

$$L_5 = imV_{16} + \frac{\psi_1}{d_1^2}V_{21} + V_{31},$$

$$L_6 = \frac{\gamma_3}{3}\left[Q_1 - \frac{V}{12\tau_2}(\psi_2Q_{19} + d_1^2Q_{24} + 2\psi_1Q_{29})\right],$$

$$R_i = e_1^2g_i - 2g_{i-2}, \quad P_i = e_4g_i + e_2g_{i+2},$$

$$V_i = e_2g_i + e_4g_{i+1},$$

$$Q_i = -\frac{q_0^2}{q^2}g_i + e_4^2q_{i+1} + 2e_2e_4g_{i+3} + e_2^2g_{i+2},$$

$$\rho_1 = \frac{\eta\eta_3V}{12d_1\psi}, \quad \rho_2 = \frac{\eta_3V^2d_1}{12md_2}, \quad \rho_3 = \frac{\eta V^3d_1}{12md_3},$$

$$\psi_2 = 4xy\tau_2 + (z_1 - z_2)^2, \quad \gamma_1 = -2e_3\frac{\sqrt{-q^2}}{q_0}N_k,$$

$$\gamma_2 = 2e_1e_3N_k, \quad \gamma_3 = -2\frac{q^2}{q_0^2}N_k,$$

$$N_k = \frac{\alpha^2}{4}\frac{1}{(2\pi)^3VQ^2(1-\varepsilon)}\frac{d^3k_2}{\varepsilon_2}\frac{d^3p_2}{E_2},$$

$$e_1 = |\mathbf{p_2}|\sin\theta, \quad e_2 = |\mathbf{p_2}|\cos\theta + \frac{z_1 - z_2}{2xy}|\mathbf{q}|,$$

$$e_3 = -W|\mathbf{p_2}||\mathbf{q}|\sin\theta, \quad e_4 = -\frac{W^2 - M^2 + q^2}{2q^2}|\mathbf{q}|,$$

where W is the invariant mass of the VX system.

To use the Drell–Yan representation, we have to express all the variables and quantities in both sides of Eqs. (24) and (25) through invariant variables. The corresponding formulae read

$$W = \sqrt{V(\tau_1 + y - xy)}, \quad |\mathbf{p}_2| = \frac{d}{2}\sqrt{\frac{V}{(\tau_1 + y - xy)}},$$

$$\mathbf{q}^2 = \frac{Vy(y + 4x\tau_1)}{4(\tau_1 + y - xy)}, \quad q^2 = -xyV,$$

$$q_0 = \frac{1 - 2x}{2}\sqrt{\frac{Vy^2}{\tau_1 + y(1-x)}},$$

$$\varepsilon = \frac{2(1 - y - xy\tau_1)}{1 + (1-y)^2 + 2xy\tau_1},$$

$$\cos\theta = \frac{yz(1-2x) - (z_1 - z_2)(y + 2\tau_1)}{d\sqrt{y(y + 4x\tau_1)}}, \qquad (26)$$

and the azimuthal angle ϕ can be obtained from the equation

$$\sin\phi = -\frac{\eta}{d\sin\theta}\sqrt{\frac{\tau_1 + y(1-x)}{xy(1 - y - xy\tau_1)}}.$$

Note in conclusion that we obtain a rather compact formula for taking into account the leading-order RC for the process of semi-inclusive vector-meson electroduction. The results obtained do not depend on the particular choice of model for the process investigated. All the dynamics of the reaction under consideration is contained in the structure functions g_i.

REFERENCES

1. J. A. Crittenden, hep-ex/9704009.

2. C. Adloff, V. Andreev, *et al.* (H1 Collab.), hep-ex/0203022.
3. R. L. Jaffe, hep-ph/0101280.
4. C. Adloff *et al.*, Eur. Phys. J. C **13**, 371 (2000); J. Breitweg *et al.*, Eur. Phys. J. C **12**, 393 (2000).
5. J. A. Crittenden, hep-ex/0110040.
6. A. Airapetian *et al.*, Phys. Lett. B **513**, 301 (2001).
7. V. N. Gribov and L. N. Lipatov, Yad. Fiz. **15**, 808 (1972) [Sov. J. Nucl. Phys. **15**, 451 (1972)]; Yad. Fiz. **15**, 1218 (1972) [Sov. J. Nucl. Phys. **15**, 675 (1972)]; L. N. Lipatov, Yad. Fiz. **20**, 94 (1974) [Sov. J. Nucl. Phys. **20**, 48 (1975)]; G. Altarelli and G. Parisi, Nucl. Phys. B **126**, 298 (1977).
8. G. I. Gakh and N. P. Merenkov, Pis'ma Zh. Éksp. Teor. Fiz. **73**, 659 (2001) [JETP Lett. **73**, 579 (2001)].
9. E. Kuraev and V. Fadin, Yad. Fiz. **41**, 733 (1985) [Sov. J. Nucl. Phys. **41**, 466 (1985)]; Yad. Fiz. **47**, 1593 (1988) [Sov. J. Nucl. Phys. **47**, 1009 (1988)].
10. S. D. Drell and T. M. Yan, Phys. Rev. Lett. **25**, 316 (1970).
11. G. I. Gakh and N. P. Merenkov, Pis'ma Zh. Éksp. Teor. Fiz. **75** (12), 734 (2002) [JETP Lett. **75**, 610 (2002)].
12. G. N. Khachatryan and Yu. G. Shakhnazaryan, Yad. Fiz. **26**, 1258 (1977) [Sov. J. Nucl. Phys. **26**, 664 (1977)].
13. K. Schilling, P. Seyboth, and G. Wolf, Nucl. Phys. B **15**, 397 (1970).
14. T. H. Bauer, R. D. Spital, D. R. Yennie, and F. M. Pipkin, Rev. Mod. Phys. **50**, 261 (1978).

JETP Letters, Vol. 76, No. 3, 2002, pp. 127–130. From Pis'ma v Zhurnal Éksperimental'noĭ i Teoreticheskoĭ Fiziki, Vol. 76, No. 3, 2002, pp. 158–161.

Mass of the Higgs versus Fourth Generation Masses¶

V. A. Novikov*, L. B. Okun*, A. N. Rozanov, and M. I. Vysotsky***

** Institute of Theoretical and Experimental Physics, Moscow, 117218 Russia*

*** CPPM, IN2P3, CNRS, Universite Mediteranee, Marseilles, France*

e-mail: novikov@heron.itep.ru; okun@heron.itep.ru; rozanov@cppm.in2p3.fr; vysotsky@heron.itep.ru

Received June 13, 2002; in final form, July 11, 2002

The predicted value of the higgs mass m_H is analyzed assuming the existence of the fourth generation of leptons (N, E) and quarks (U, D). The steep and flat directions are found in the five-dimensional parameter space: m_H, m_U, m_D, m_N, m_E. The LEPTOP fit of the precision electroweak data is compatible (in particular) with $m_H \sim$ 300 GeV, $m_N \sim 50$ GeV, $m_E \sim 100$ GeV, $m_U + m_D \sim 500$ GeV, and $|m_U - m_D| \sim 75$ GeV. The quality of fits drastically improves when the data on b- and c-quark asymmetries and new NuTeV data on deep inelastic scattering are ignored. © *2002 MAIK "Nauka/Interperiodica".*

PACS numbers: 12.60.Fr; 14.80.Bn; 12.15.Lk

It is well known that, in the framework of the Standard Model, the fit of electroweak precision data results in the prediction of light higgs, the central value of its mass being lower than the direct lower limit set by LEP II [1]. One possible way to raise the predicted value of m_H is to assume the existence of the fourth generation of leptons and quarks [2, 3]. Implications of extra quark–lepton generations for precision data were studied in a number of papers [2–7]. Leptons of the fourth generation (E, N) should be very weakly mixed with the ordinary ones, while in the quark sector (U, D) mixing is limited only by the unitarity of the 3×3 CKM matrix. In particular, it was noticed in [2] that the predicted mass of the higgs could be as high as 500 GeV. That conclusion was based on a sample of 10000 random inputs of masses of fourth-generation leptons and quarks. However, the sets of the lepton and quark masses were presented independently (see Fig. 7 in [2]). Thus, it is not clear how they were combined.

In this letter, we try to develop a systematic approach to the problem by using our LEPTOP code [8] to find steep and flat directions in the five-dimensional parameter space: m_H, m_U, m_D, m_E, m_N. For each point in this space we perform a three-parameter fit (m_t, α_s, $\bar{\alpha}$) and calculate the χ^2 of the fit. It turns out that the $\chi^2_{\min}$ depends weakly on $m_U + m_D$ and m_H, while its dependence on $m_U - m_D$, m_E and m_N is strong. We limit ourselves to the values of m_N larger than 50 GeV because, according to the experimental data from LEP II on the emission of initial state bremsstrahlung photons, $m_N >$ 50 GeV at 95% c.l. [9, 10].

We analyzed Summer 2001 precision data ([1], which are also given in Table 1 in [3]). Figures 1–4 show $\chi^2_{\min}$ (crosses) and constant χ^2 lines corresponding to $\Delta\chi^2 = 1, 4, 9, 16, \ldots$ on the plane m_N, $m_U - m_D$ for fixed values of $m_U + m_D = 500$ GeV, $m_H = 120$ (Figs. 1, 3) and 500 GeV (Figs. 2, 4) and $m_E = 100$ (Figs. 1, 2) and 300 GeV (Figs. 3, 4). We also performed fits for $m_H = 300$ GeV.

The above choice of masses is based on a large number of fits covering a broad space of parameters: 300 GeV $< m_U + m_D <$ 800 GeV; 0 GeV $< m_U - m_D <$ 400 GeV; 100 GeV $< m_E <$ 500 GeV; 50 GeV $< m_N <$ 500 GeV; 120 GeV $< m_H <$ 500 GeV. Concerning quarks, $m_U + m_D$ is bounded from below by the limit of direct searches, while from above, by triviality arguments. Since the χ^2 dependence on $m_U + m_D$ is very weak, our choice of the intermediate value $m_U + m_D =$ 500 GeV represents a typical, almost general case. For this choice, $|m_U - m_D|$ cannot be larger than ~200 GeV because of the limit of direct searches mentioned above.

Concerning the charged lepton, its mass is taken above the LEP II bound. We present fits at two values of m_E (100 GeV and 300 GeV), and one can see how the fit worsens as m_E goes up.

Concerning the value of m_H, we vary it from the lower LEP II limit up to the triviality bound, and, since the dependence of observables on m_H is flat, one can get the χ^2 behavior from two limiting points: $m_H = 120$ and 500 GeV.

For $m_E = 100$ GeV, we have a minimum of χ^2 at $m_N \simeq 50$ GeV and

for $m_H = 120$ GeV:

$$|m_U - m_D| \sim 50 \text{ GeV}, \quad \chi^2_{\min}/n_{d.o.f} = 20.6/12;$$

¶This article was submitted by the authors in English.

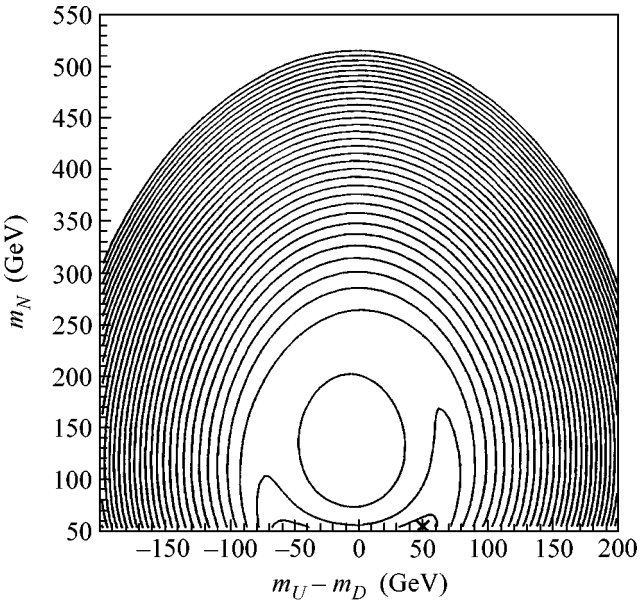

Fig. 1. Exclusion plot on the plane m_N, $m_U - m_D$ for fixed values of m_H = 120 GeV, $m_U + m_D$ = 500 GeV, and m_E = 100 GeV. $\chi^2_{\min}$ shown by two crosses corresponds to $\chi^2/n_{d.o.f.}$ = 20.6/12. (The left-hand cross is slightly below m_N = 50 GeV.) Borders of regions show domains allowed at the level $\Delta\chi^2$ = 1, 4, 9, 16, etc. The plot was based on the old NuTeV data. The new NuTeV data preserve the pattern of the plot but lead to $\chi^2_{\min}/n_{d.o.f.}$ = 27.7/12. If A^b_{FB} and A^c_{FB} uncertainties are multiplied by factor 10, we get $\chi^2_{\min}/n_{d.o.f.}$ = 19.1/12 for new NuTeV, and $\chi^2_{\min}/n_{d.o.f.}$ = 11.3/12 for old NuTeV with practically the same pattern of the plot.

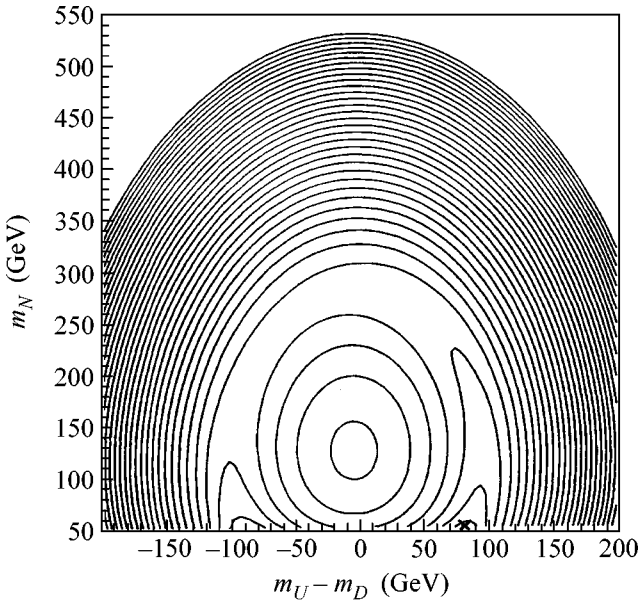

Fig. 2. Exclusion plot on the plane m_N, $m_U - m_D$ for fixed values of m_H = 500 GeV, $m_U + m_D$ = 500 GeV, and m_E = 100 GeV. $\chi^2_{\min}$ shown by two crosses corresponds to $\chi^2/n_{d.o.f.}$ = 21.4/12. (The left-hand cross is slightly below m_N = 50 GeV.) Borders of regions show domains allowed at the level $\Delta\chi^2$ = 1, 4, 9, 16, etc. The plot was based on the old NuTeV data. The new NuTeV data preserve the pattern of the plot but lead to $\chi^2_{\min}/n_{d.o.f.}$ = 28.3/12. If A^b_{FB} and A^c_{FB} uncertainties are multiplied by a factor 10, we get $\chi^2_{\min}/n_{d.o.f.}$ = 21.2/12 for new NuTeV, and $\chi^2_{\min}/n_{d.o.f.}$ = 13/12 for old NuTeV with practically the same pattern of the plot.

for m_H = 300 GeV:

$$|m_U - m_D| \sim 75 \text{ GeV}, \quad \chi^2_{\min}/n_{d.o.f.} = 20.8/12;$$

and for m_H = 500 GeV:

$$|m_U - m_D| \sim 85 \text{ GeV}, \quad \chi^2_{\min}/n_{d.o.f.} = 21.4/12.$$

Thus, we have two lines ($m_U > m_D$ and $m_U < m_D$) in the ($m_U - m_D$, m_H) space that correspond to the best fit of the data. Along these lines, the quality of the fit is only slightly better for the light higgs ($m_H \sim$ 120 GeV) than for the heavy one ($m_H \sim$ 300–500 GeV).

Note that the $n_{d.o.f.}$ is 12, unlike the case of the Standard Model, where it was 13 [3]. This change occurs because in the present paper m_H is a fixed rather than fitted parameter (hence, 13 becomes 14), while m_N and $m_U - m_D$ are two additional fitted parameters (hence, 14 becomes 12). (As is well known, $n_{d.o.f.}$ is equal to the number of experimentally measured observables minus the number of fitted parameters.)

For m_E = 300 GeV, we have a minimum of χ^2 at $m_U - m_D \simeq$ 25 GeV and
for m_H = 120 GeV:

$$m_N \sim 200 \text{ GeV}, \quad \chi^2_{\min}/n_{d.o.f.} = 23.0/12;$$

for m_H = 300 GeV:

$$m_N \sim 170 \text{ GeV}, \quad \chi^2_{\min}/n_{d.o.f.} = 24.0/12;$$

and for m_H = 500 GeV:

$$m_N \sim 150 \text{ GeV}, \quad \chi^2_{\min}/n_{d.o.f.} = 24.4/12.$$

Thus, the best fit of the data corresponds to the light $m_E \simeq$ 100 GeV and $m_N \simeq$ 50 GeV. The significance of light m_N (around 50 GeV) was first stressed in [5]. An increase in m_E leads to an increase in m_N and to the fast worsening of $\chi^2_{\min}$.

Although the inclusion of one extra generation improves the quality of the fit (compare $\chi^2/n_{d.o.f.}$ =

23.8/13 for the SM from [3] and $\chi^2_{\min}/n_{d.o.f.} = 20.6/12$ from Fig. 1), it remains pretty poor. The poor quality of the fit is due to the 3.3σ discrepancy in $s_l^2 \equiv \sin^2\theta_{\text{eff}}$ extracted from leptonic decays and from $A_{FB}^{b,c}$ [11]. If one multiplies the experimental errors in A_{FB}^b and A_{FB}^c by a factor of 10, one gets a good quality SM fit [3, 11] but with extremely light higgs, having only a small (few percent) likelihood of being consistent with the lower limit from direct searches. We prove that the fourth generation allows one to have higgs as heavy as 500 GeV with a perfect quality of the fit: $\chi^2_{\min}/n_{d.o.f.} = 13/12$, if one uses the old NuTeV data (see caption to Fig. 2).

To qualitatively understand the dependence of $m_U - m_D$ on m_H in the case of $m_E = 100$ GeV at $\chi^2_{\min}$, let us recall how radiative corrections to the ratio m_W/m_Z and to g_A and $R = g_V/g_A$ (the axial and the ratio of vector and axial couplings of Z-boson to charged leptons) depend on these quantities [6]:

$$\delta V^i \approx \left[-\begin{pmatrix} \frac{11}{9}s^2 \\ s^2 \\ s^2 + \frac{1}{9} \end{pmatrix} \ln\left(\frac{m_H}{m_Z}\right)^2 + \frac{4}{3}\frac{(m_U - m_D)^2}{m_Z^2} + \begin{pmatrix} \frac{16}{9}s^2\frac{m_U - m_D}{m_U + m_D} \\ 0 \\ \frac{2}{9}\frac{m_U - m_D}{m_U + m_D} \end{pmatrix} \right], \quad (1)$$

where $i = m, A, R$, while $s^2 \simeq 0.23$. Corrections to other observables can be calculated in terms of δV^i. In the vicinity of $\chi^2_{\min}$, the third term in brackets is much smaller than the second one. This fact determines the smallness of the left–right asymmetry in the plots in Figs. 1 and 2. Since $\frac{11}{9}s^2 \approx s^2 + \frac{1}{9} \approx s^2$, the increase in m_H is compensated by an increase in $|m_U - m_D|$, and we have a valley of $\chi^2_{\min}$.

Captions to Figs. 1 and 2 reflect the recent change in NuTeV data (from $m_W = 80.26 \pm 0.11$ GeV [12] to $m_W = 80.14 \pm 0.08$ GeV [13]), which results in a drastic worsening of the fit even in the presence of the fourth generation.

Thus, we see that the 4th family scenario is better than the Standard Model, because the latter can produce a good fit only when the mass of the higgs is much lower than the lower limit of LEP II, even when experimental data on heavy quark asymmetries and new NuTeV data are ignored.

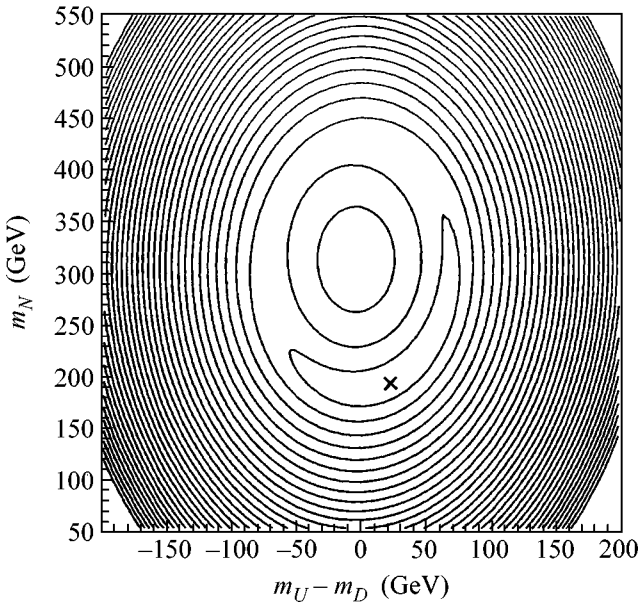

Fig. 3. Exclusion plot on the plane m_N, $m_U - m_D$ for fixed values of $m_H = 120$ GeV, $m_U + m_D = 500$ GeV, and $m_E = 300$ GeV. $\chi^2_{\min}$ shown by the cross corresponds to $\chi^2_{\min}/n_{d.o.f.} = 23.0/12$. Borders of regions show domains allowed at the level $\Delta\chi^2 = 1, 4, 9, 16$, etc.

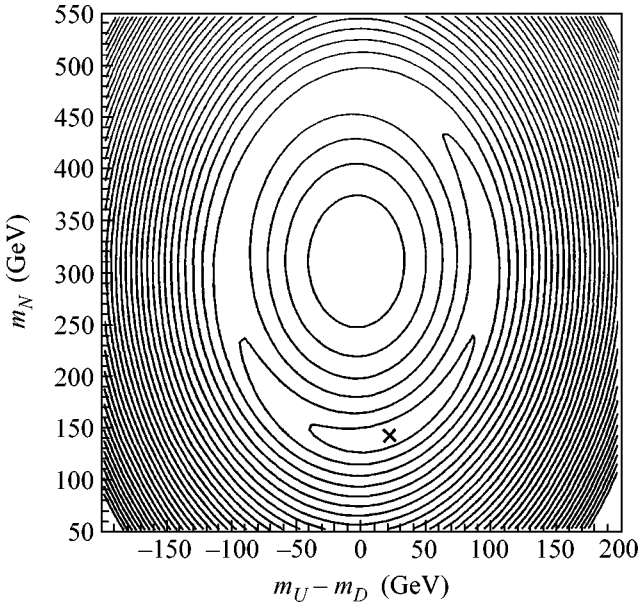

Fig. 4. Exclusion plot on the plane m_N, $m_U - m_D$ for fixed values of $m_H = 500$ GeV, $m_U + m_D = 500$ GeV, and $m_E = 300$ GeV. $\chi^2_{\min}$ shown by the cross corresponds to $\chi^2_{\min}/n_{d.o.f.} = 24.4/12$. Borders of regions show domains allowed at the level $\Delta\chi^2 = 1, 4, 9, 16$, etc.

Note that the parameters *S*, *T*, and *U* originally introduced in [14] are not adequate for the above analysis, because they assume that all particles of the fourth generation are much heavier than m_Z, while in our case the best fit corresponds to $m_N \sim m_Z/2$. In paper [2], modified definitions of *S* and *U* were used in order to deal with new particles with masses comparable to m_Z. However, let us stress that both original and modified definitions of *S*, *T*, and *U* take into account the radiative corrections from the "light" 4th neutrino only approximately, while the threshold effects, which are so important for $m_N \simeq 50$ GeV, can be adequately described in the framework of functions V^i.

In conclusion, let us stress that, in the framework of SUSY with three generations, the radiative corrections due to loops with superpartners also shift the mass of the higgs upward in the case of not too heavy squarks (300–400 GeV, see Table 1 in [15]) or light sneutrinos (55–80 GeV, see [16]).

V.N., L.O., and M.V. were partly supported by the RFBR grant no. 00-15-96562; V.N. was partly supported by the INTAS OPEN grant no. 2000-110 as well. We are grateful to M. Chanowitz for his comments.

REFERENCES

1. The LEP Collab., the LEPEWWG and the SLD Heavy Flavour and Electroweak working groups, CERN-EP/2001-098, hep-ex/0112021 (2001), Table 13.1.
2. H.-J. He, N. Polonsky, and S. Su, Phys. Rev. D **64**, 053004 (2001); hep-ph/0102144.
3. V. A. Novikov, L. B. Okun, A. N. Rozanov, and M. I. Vysotsky, Phys. Lett. B **529**, 111 (2002); hep-ph/0111028.
4. N. Evans, Phys. Lett. B **340**, 81 (1994); P. Bamert and C. P. Burgess, Z. Phys. C **66**, 495 (1995); T. Inami, T. Kawakami, and C. S. Lim, Mod. Phys. Lett. A **10**, 1471 (1995); A. Masiero, F. Feruglio, S. Rigolin, and R. A. Strocchi, Phys. Lett. B **355**, 329 (1995); V. A. Novikov, L. B. Okun, A. N. Rozanov, *et al.*, Mod. Phys. Lett. A **10**, 1915 (1995); Erratum: **11**, 687 (1996); J. Erler and P. Langacker, Eur. Phys. J. C **15**, 95 (2000), Chapter 10.6.
5. M. Maltoni, V. A. Novikov, L. B. Okun, *et al.*, Phys. Lett. B **476**, 107 (2000).
6. V. A. Novikov, L. B. Okun, A. N. Rozanov, and M. I. Vysotsky, Rep. Prog. Phys. **62**, 1275 (1999); M. Maltoni, Thesis, unpublished (1999); hep-ph/0002143.
7. J. I. Silva-Marcos, hep-ph/0204217; Phys. Rev. D **59**, 091301 (1999); hep-ph/9811381.
8. V. A. Novikov, L. B. Okun, A. N. Rozanov, and M. I. Vysotsky, Preprint ITEP 19-95; Preprint CPPM-1-95; http://cppm.in2p3.fr./leptop/intro leptop.html.
9. V. A. Ilyin, M. Maltoni, V. A. Novikov, *et al.*, Phys. Lett. B **503**, 126 (2001); hep-ph/0006324.
10. The ALEPH Collaboration, ALEPH 2001-010; CONF 2001-007 (2001); DELPHI Collab. (P. Abreu *et al.*), Eur. Phys. J. C **16**, 53 (2000); L3 Collab. (M. Acciari *et al.*), Phys. Lett. B **470**, 268 (1999); OPAL Collab. (G. Abbiendi *et al.*), Eur. Phys. J. C **14**, 73 (2000); see also the contributions to the Summer 2001 Conferences.
11. M. S. Chanowitz, Phys. Rev. Lett. **87**, 231802 (2001); hep-ph/0104024.
12. NuTeV Collab. (R. A. Johnson *et al.*), hep-ex/9904028 (1999).
13. NuTeV Collab. (G. P. Zeller *et al.*), hep-ex/0110059 (2001).
14. M. Peskin and T. Takeuchi, Phys. Rev. Lett. **65**, 964 (1990); Phys. Rev. D **46**, 381 (1992).
15. I. V. Gaidaenko, A. V. Novikov, V. A. Novikov, *et al.*, Phys. Rep. **320**, 119 (1999); hep-ph/9812346.
16. G. Altarelli, F. Caravaglios, G. F. Giudice, *et al.*, JHEP **0106**, 018 (2001); hep-ph/0106029.

JETP Letters, Vol. 76, No. 3, 2002, pp. 131–134. From Pis'ma v Zhurnal Éksperimental'noĭ i Teoreticheskoĭ Fiziki, Vol. 76, No. 3, 2002, pp. 162–165.

On the Depolarization of Ultracold Neutrons in Traps¶

Yu. N. Pokotilovski[1]

Joint Institute for Nuclear Research, Dubna, Moscow region, 141980 Russia

Received February 14, 2002; in final form, June 24, 2002

Mechanisms of the depolarization of ultracold neutrons in traps reflecting from the trap wall are considered. One is due to neutron spin-flip elastic or quasielastic incoherent scattering from protons of surface hydrogen contaminations. According to the second one, significant depolarization may take place because of a sudden change in the neutron trajectory on reflection from the wall when the neutron moves even at large adiabaticity parameters in nonuniform magnetic field. © *2002 MAIK "Nauka/Interperiodica".*

PACS numbers: 14.20.Dh; 13.88.+e; 25.40.Dn

1. An investigation of angular correlation coefficients in neutron beta decay is important for determining the fundamental coupling constants of weak interactions [1]. It is important to improve the accuracy of these measurements with the aim of searching for new physics beyond the Standard Model with increased sensitivity [2]. One of serious difficulties in increasing the precision of these measurements is the reliable determination (with a high accuracy) of the polarization of decaying neutrons.

It was proposed [3] that significant progress can be made by the use of polarized ultracold neutrons (UCN) [4] stored in closed volumes or flowing through the decay region. Neutrons transmitted through a sufficiently high magnetic potential barrier must have a perfect 100% polarization in the direction opposite to the magnetic field. The first experimental data on neutron depolarization in traps were published in [5]. A surprisingly large depolarization ($\sim 10^{-5}$ per UCN collision with the wall) was observed for all tested surface materials, and it was shown in a special experiment that this value of depolarization hardly depended on the UCN loss coefficient, which was changed by additionally depositing a water layer on the cooled surface. It was also stated that the depolarization due to the large gradient of the magnetic field was impossible, which was confirmed by numerical evaluations.

The objective of this paper is to consider the possible mechanisms of the depolarization of UCN in traps without having in mind an exact quantitative interpretation of the existing experimental data.

2. The obvious and trivial reason for UCN depolarization in traps is neutron spin-flip scattering from hydrogen. The most promising materials for UCN chambers, namely, Be, C, glass, and fluoropolymers, do not contain nuclei with a significant spin-flip cross section. UCN upscattering from hydrogen contaminations of the trap surface is the usual and the main reason for the abnormally large losses of UCN from the traps [4]. The UCN cross section for upscattering from a bound proton of a room temperature sample is $\sigma_{ups} \simeq (4\text{–}7)b \times 2200/v$ (m/s)[6], depending on the chemical bond of the hydrogen atom (v is the UCN velocity). The elastic (or quasielastic in the case of diffusing protons or/and in the presence of the hyperfine splitting of the hydrogen atom) spin-flip scattering cross section $\sigma_{el} \simeq \frac{2}{3} \times 80b$. Therefore, the ratio of spin-flip to UCN–hydrogen upscattering loss probabilities is $\sim(1.5\text{–}3) \times 10^{-2}$. In a trap with UCN, the loss probability due to upscattering from hydrogen equals $\sim 4 \times 10^{-5}$ (rather good value), and the spin-flip probability is $\sim 10^{-6}$, which is not quite satisfactory for the neutron decay correlation coefficient.

The energy splitting of magnetic sublevels in paramagnetic atoms is usually much larger than the UCN energy. Therefore, after spin-flip paramagnetic scattering, neutrons must leave the storage chamber. Anyway, the cross section of paramagnetic scattering is of the order of 1 b, and the probability of spin-flip on reflection from the wall is $\sim 10^{-7}$ even in the case when all atoms of the wall are paramagnetic. This is hardly possible for typical wall materials.

3. The effect of magnetic field inhomogeneities on the spin relaxation of neutral particles with magnetic moment was considered in [7, 8]. It was assumed in these works that the applied magnetic field is a superposition of a weak spatially varying field upon a much stronger homogeneous field, and the problem was solved with the use of the perturbation method. According to [3], this is not the case when UCN are polarized by transmission through a magnetic potential barrier and then are stored in an experimental chamber. The fluctuations of the magnetic field for a slow neutron moving in the chamber are not random and small in this case, but the adiabaticity parameter—the ratio of Lar-

¶ This article was submitted by the author in English.

[1] e-mail: pokot@nf.jinr.ru

mor frequency to frequency of rotation of magnetic field in the neutron reference frame—can be large enough, so that the spin relaxation probability for a freely moving neutron must be exponentially small. It will be shown here that, nevertheless, the depolarization may be significant, because the time derivative of the magnetic field is discontinuous if the wall collision takes place in a time that is short compared to the period of Larmor precession.

Let a neutral particle with a magnetic moment (in particular, an ultracold neutron) move in a nonuniform magnetic field inside a trap, reflecting from the trap walls. We place the neutron reference frame at the reflection point, so that the x axis is along the magnetic field line.

With constant $H_x \neq 0$, $H_y = 0$, $H_z = t\dot{H}$, $\dot{H} > 0$ and following the paper by V.V. Vladimirsky [9], we obtain the equation for the spin wave function

$$i\dot{\psi} + \omega\sigma_x\psi + at\sigma_z\psi = 0, \tag{1}$$

where $\omega = \mu H_x/\hbar$, $a = \mu\dot{H}/\hbar$, and μ is the magnetic moment of a neutron.

The equations for each spinor component look as follows:

$$\begin{aligned}\ddot{\phi} + (\omega^2 - ia + a^2t^2) &= 0,\\ \ddot{\chi} + (\omega^2 + ia + a^2t^2)\chi &= 0.\end{aligned} \tag{2}$$

Substituting $\phi = e^{-z/2}u$, $\chi = e^{-z/2}v$, $z = -iat^2$, and introducing $\alpha = \omega^2/4ia$, transform (2) to the confluent hypergeometric equations

$$\begin{aligned}zu'' + \left(\frac{1}{2} - z\right)u' - \alpha u &= 0,\\ zv'' + \left(\frac{1}{2} - z\right)v' - \left(\alpha + \frac{1}{2}\right)v &= 0.\end{aligned} \tag{3}$$

The solutions of these equations are

$$\begin{aligned}\phi(t) = e^{iat^2/2}[&c_1F(\alpha, 1/2, -iat^2)\\ &+ c_2i\omega tF(\alpha + 1/2, 3/2, -iat^2)],\end{aligned} \tag{4}$$

and

$$\begin{aligned}\chi(t) = e^{iat^2/2}[&c_1i\omega tF(\alpha + 1, 3/2, -iat^2)\\ &+ c_2F(\alpha + 1/2, 1/2, -iat^2)],\end{aligned} \tag{5}$$

where $F(\alpha, \gamma, z)$ are Kummer functions.

Asymptotics at $t \longrightarrow \pm\infty$ are

$$\begin{aligned}\phi(t) &= \sqrt{\pi}e^{-\pi\omega^2/8a}\\ &\times\left[\frac{c_1}{\Gamma(1/2-\alpha)} + \frac{i\omega}{2\sqrt{ia}}\frac{c_2}{\Gamma(1-\alpha)}\frac{t}{|t|}\right](at^2)^{-\alpha}e^{iat^2/2}\end{aligned} \tag{6}$$

and

$$\begin{aligned}\chi(t) &= \sqrt{\pi}e^{-\pi\omega^2/8a}\\ &\times\left[\frac{i\omega}{2\sqrt{-ia}}\frac{c_1}{\Gamma(1+\alpha)}\frac{t}{|t|} + \frac{c_2}{\Gamma(1/2+\alpha)}\right](at^2)^{\alpha}e^{-iat^2/2}.\end{aligned} \tag{7}$$

If the z-component of the magnetic field varies according to $H_z = -t\dot{H}$, $\dot{H} > 0$, the equations and solutions for spin components interchange.

On reflection from the surface at $t = 0$, the particle suddenly changes its trajectory and then follows on with a different value of the gradient of the z-component of the magnetic field. The condition that this transition is "sudden" is fulfilled if the reflection time is much smaller than any characteristic time parameter of the problem: $t_{\text{refl}} \ll T_{\text{Larmor}}$. It will be shown below that the typical value for ultracold neutrons $t_{\text{refl}} \approx 10^{-9}$ s, which is sufficient for any practical case.

Now, we match the solutions with different values of a at $t = 0$ corresponding to different trajectories of a particle in a magnetic field before and after the reflection from the wall. When the signs of dH_z/dt are the same, the matching means $\phi(\alpha)_{t=0} = \phi(\alpha')_{t=0}$, when the signs are different, we use $\phi(\alpha)_{t=0} = \chi(\alpha')_{t=0}$. We put $\chi(-\infty) = 0$, $|\phi(-\infty)|^2 = 1$ (initially, the particle is polarized opposite to the z axis) and obtain the expressions for $|\phi(+\infty)|^2$

$$\begin{aligned}|\phi(+\infty)|^2 &= \pi^2e^{-\frac{\pi\omega^2}{4}\left(\frac{1}{\alpha}+\frac{1}{\alpha'}\right)}\\ &\times\left|\frac{1}{\Gamma(1/2+\alpha)\Gamma(1/2-\alpha')} - \frac{\omega^2}{4\sqrt{aa'}}\frac{1}{\Gamma(1+\alpha)\Gamma(1-\alpha')}\right|^2\end{aligned} \tag{8}$$

for the cases when the signs of the change in the $H_z(t)$ component of the magnetic field are the same before and after the particle reflection from the wall, and

$$\begin{aligned}|\phi(+\infty)|^2 &= \pi^2e^{-\frac{\pi\omega^2}{4}\left(\frac{1}{\alpha}+\frac{1}{\alpha'}\right)}\\ &\times\left|\frac{1}{\Gamma(1/2+\alpha)\Gamma(1/2+\alpha')} - \frac{i\omega^2}{4\sqrt{aa'}}\frac{1}{\Gamma(1+\alpha)\Gamma(1+\alpha')}\right|^2\end{aligned} \tag{9}$$

when these signs are different; e.g., the particle returns after the reflection from the wall to the region of the magnetic field of the same sign of H_z. In these expressions, α' corresponds to the particle motion after the reflection.

When in Eq. (8) $\alpha = \alpha'$, we get $|\phi(+\infty)|^2 = e^{-\pi\omega^2/a}$, which corresponds to the result of [9] for the probability of spin reversal when the particle moves freely without changing its trajectory. For ultracold neutrons, the adiabaticity parameter $|\alpha| \gg 1$, $|\phi(+\infty)|^2 \longrightarrow 0$ (exponentially small) practically in all cases, and the neutron spin follows the direction of the magnetic field. The calculation according to Eqs. (8) and (9) show that this is

not the case when the particle reflects from the wall. The probability of spin reversal with respect to the magnetic field increases drastically. Fig. 1 shows the results of a computation of this probability for different cases of reflection as a function of $|\alpha'|$.

In practice, it is difficult to calculate the probability according to Eqs. (8) and (9) for $|\alpha'| \gg 1$. Using asymptotic formulas for the gamma function makes it possible in this case to obtain for Eq. (8)

$$|\phi(+\infty)|^2 \simeq \frac{9}{4}(\xi - \xi')^2, \tag{10}$$

and for Eq. (9)

$$|\phi(+\infty)|^2 \simeq 1 - 11(\xi^2 + \xi'^2) - 18\xi\xi', \tag{11}$$

where $\xi = 1/24|\alpha|$, $\xi' = 1/24|\alpha'|$.

Figure 2 shows the results of calculations according to these formulas in terms of the probability of spin reversal as a function of the gradient of H_z. The neutron velocity along the z axis was taken to be equal to 300 cm/s, $H_x = 5$ Oe.

4. The interaction time of a particle reflecting from a potential wall can be calculated in the spirit of the Baz' [10, 11] idea by introducing a fictitious infinitesimal magnetic field in the interaction region and calculating the rotation angle of the magnetic moment of the particle due to the interaction. The reflection time in our case is determined as a ratio of rotation angle to Larmor frequency of precession of the magnetic moment in this magnetic field. Let the incident wave polarized in the x-direction reflect from half-space $z \geq 0$, in which the magnetic field is directed along z axis. The Schrödinger equation is

$$\left(\Delta + u_0 - \frac{2m}{\hbar^2}\mu H\sigma_z\right)\psi = k^2\psi, \tag{12}$$

where $u_0 = 2mU_0/\hbar^2$, U_0 is the height of the potential wall, k is the incident wave vector, and H is the value of the magnetic field in the half-space $z \geq 0$. The incident wave is

$$\psi_0 = \frac{1}{\sqrt{2}}\begin{pmatrix}1\\1\end{pmatrix}e^{i(\boldsymbol{\kappa}\boldsymbol{\rho} + k_z z)}. \tag{13}$$

The reflected wave is

$$\psi = e^{i\varphi_0}\left[\begin{pmatrix}1\\1\end{pmatrix} + i\Delta\varphi\sigma_z\begin{pmatrix}1\\1\end{pmatrix}\right]e^{i(\boldsymbol{\kappa}\boldsymbol{\rho} - k_z z)}. \tag{14}$$

It follows [10] that

$$\Delta\varphi = \frac{d\varphi}{du_0}\left(\frac{2m}{\hbar^2}\mu H\right), \tag{15}$$

and, as it is easy to show, that

$$\frac{d\varphi}{du_0} = \frac{k_z}{u_0 K}, \tag{16}$$

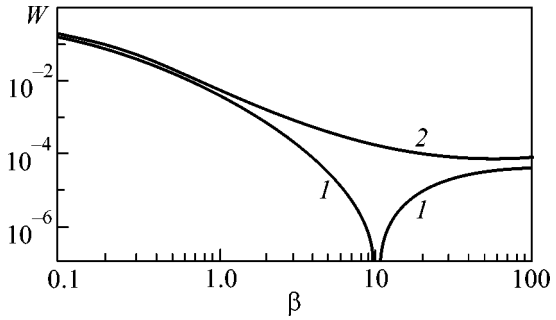

Fig. 1. Probability of UCN spin reversal on reflection from the trap wall as a function of the adiabaticity parameter $\beta = |\alpha'|$ after the reflection (before the reflection, $\beta = |\alpha| = 10$): (*1*) the signs of the time dependence of $H_z(t)$ are the same before and after the reflection and (*2*) these signs are opposite.

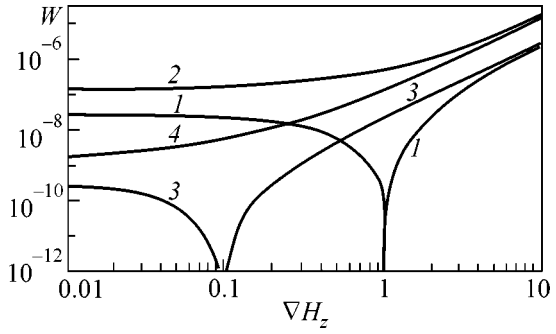

Fig. 2. Probability of UCN spin reversal on reflection from the trap wall as a function of dH_z/dz after the reflection: before the reflection $dH_z/dz = 0.1$ Oe/cm, (*1*) signs of the time dependence of $H_z(t)$ are the same before and after reflection, (*2*) these signs are opposite; before reflection $dH_z/dz = 1$ Oe/cm, (*3*) signs of time dependence of $H_z(t)$ are the same before and after reflection, (*4*) these signs are opposite; in both cases $v_z = 300$ cm/s, $H_x = 5$ Oe.

where $K = \sqrt{u_0 - k_z^2}$, we obtain from $\omega = 2\mu H/\hbar$ and $\omega m k_z/\hbar u_0 K = \omega\Delta t$ the reflection time

$$\Delta t = \frac{\hbar}{U_0}\frac{k_z}{K} \sim \frac{\hbar}{U_0}, \tag{17}$$

which at $U_0 \sim 10^{-7}$ eV gives $\Delta t \sim 10^{-9}$ s.

REFERENCES

1. B. G. Erozolimsky, Nucl. Instrum. Methods Phys. Res. A **440**, 491 (2000).
2. H. Abele, Nucl. Instrum. Methods Phys. Res. A **440**, 499 (2000).
3. A. P. Serebrov *et al.*, Preprint LNPI-1391 (Gatchina, 1988); Preprint PNPI-1835 (Gatchina, 1992); T. Bowles *et al.*, *A letter of intent for an accurate measurement of*

the neutron spin-electron angular coefficient in polarized neutron beta-decay with UCN, LANL (Los Alamos, 1997); S. J. Seestrom, in *Proceedings of the International Seminar on Interaction of Neutrons with Nuclei, ISINN-6, Dubna, 1998*, p. 89.

4. A. Steyerl, Springer Tracts Mod. Phys. **80**, 57 (1977); R. Golub and J. M. Pendlebury, Rep. Prog. Phys. **42**, 439 (1979); V. K. Ignatovich, *The Physics of Ultracold Neutrons* (Nauka, Moscow, 1986; Clarendon, Oxford, 1990); R. Golub, D. J. Richardson, and S. Lamoreaux, *Ultracold Neutrons* (Adam Hilger, Bristol, 1991).
5. A. Serebrov, A. Vasiliev, M. Lasakov, *et al.*, Nucl. Instrum. Methods Phys. Res. A **440**, 717 (2000); A. P. Serebrov, J. Butterworth, V. E. Varlamov, *et al.*, Preprint PNPI-2438 (Gatchina, 2001).
6. K. Knopf and W. Waschkowski, J. Neutron Res. **5**, 147 (1997).
7. D. Kleppner, H. M. Goldenberg, and N. F. Ramsey, Phys. Rev. **126**, 603 (1962).
8. L. D. Shearer and G. K. Walters, Phys. Rev. **139**, A1398 (1965).
9. V. V. Vladimirskiĭ, Zh. Éksp. Teor. Fiz. **39**, 1062 (1960) [Sov. Phys. JETP **12**, 740 (1960)].
10. A. I. Baz', Zh. Éksp. Teor. Fiz. **47**, 1874 (1964) [Sov. Phys. JETP **20**, 1261 (1964)].
11. V. F. Rybachenko, Yad. Fiz. **5**, 685 (1967) [Sov. J. Nucl. Phys. **5**, 484 (1967)].

JETP Letters, Vol. 76, No. 3, 2002, pp. 135–138. Translated from Pis'ma v Zhurnal Éksperimental'noĭ i Teoreticheskoĭ Fiziki, Vol. 76, No. 3, 2002, pp. 166–170.

Bose Condensate Drag in a System of Two Coupled Traps

M. V. Demin, Yu. E. Lozovik*, and V. A. Sharapov

Institute of Spectroscopy, Russian Academy of Sciences, Troitsk, Moscow region, 142190 Russia

** e-mail: lozovik@isan.troitsk.ru*

Received June 28, 2002

A system of two plane traps disposed one above the other and confined atomic Bose condensate is considered. The possibility of entraining atoms of one of the traps by the atoms of the other trap upon the rotation of the latter is studied. The average angular momentum induced by the rotation of the first trap is found for the atoms in the second trap. © *2002 MAIK "Nauka/Interperiodica".*

PACS numbers: 03.75.Fi; 34.50.Ez

The discovery of the Bose condensation of trap-cooled atoms [1–3] has motivated the study of a number of new physical phenomena (see reviews [4, 5]). A system of two adjacent traps is an interesting physical object. In particular, this system offers promise for the Josephson effect, etc. In this work, the effect of atomic drag in a system of two plane spatially separated traps situated one above the other and confining the atomic Bose condensate. We assume that these traps are separated by a distance for which the interatomic interaction in different traps cannot be ignored (vertically coupled traps). The two-dimensionality of traps signifies that the separation between the size-quantization levels ($\hbar\omega_z$) along the smaller size far exceeds the characteristic energies of a two-dimensional Bose gas such as chemical potential μ_{2D}, kT, etc. In terms of characteristic lengths, this implies that the characteristic atomic de Broglie wavelength $\lambda = \hbar/\sqrt{mE}$, where E is the above-mentioned characteristic energies (μ_{2D} and kT), is larger than the trap vertical size $l_z = \sqrt{\hbar/m\omega_z}$. The confining potential in the two-dimensional traps can be written as

$$V_{j\text{ext}}(x, y) = \frac{m\omega_{jx}^2 x^2}{2} + \frac{m\omega_{jy}^2 y^2}{2}, \quad j = 1, 2. \qquad (1)$$

Two drag mechanisms may be considered for two adjacent traps.

(1) The drag effect, where only the normal component in the second trap is entrained by the atomic movement in the first trap.[1]

(2) Let the confining potential of the (for definiteness) lower trap be anisotropic in the *xy* plane. Let us rotate the confining potential of the lower anisotropic trap (with an angular velocity Ω). Let Ω be so small that no vortices appear in this trap. Under adiabatic conditions, the atomic density has the symmetry of the rotating trap. The essence of the predicted effect becomes more clear when it is assumed that the confining potential of the second trap is isotropic. It is shown below that, due to the interatomic interaction between the different traps, an anisotropic effective confining potential appears in the upper trap with the same angular velocity as the lower anisotropic trap. This gives rise to the rotation of the upper atomic system, i.e., to the induced angular momentum $M_{2z} = J_{21}\Omega$. Our goal is to calculate the drag coefficient J_{21} ("mutual moment of inertia") as a linear response of the upper trap to the rotation of the lower trap. Interestingly, both the superfluid and the normal components should be entrained in the anisotropic case considered.

In this work, we consider the above-mentioned second effect, i.e., the effect of entrainment due to the anisotropy of Bose gas in the first trap and *induced* anisotropy in the second trap. Let the Bose gas be rotated about the *z* axis in anisotropic trap *1* and the confining potential in trap *2* is isotropic in the *xy* plane, and let the gas in this trap be initially at rest. For a distance between the traps larger than between the minima of interatomic potentials, the interatomic interactions between the different traps can be described by the van der Waals potential

$$U(\mathbf{r} - \mathbf{r}') = -\frac{\alpha_6}{[(\mathbf{r} - \mathbf{r}')^2 + D^2]^3}. \qquad (2)$$

For the typical experimental situation of a rarefied Bose gas at a temperature lower than the Bose-condensation temperature, the number of atoms in the trapped Bose condensates far exceeds the number of noncondensed particles. We also assume that the trapped atoms obey the Thomas–Fermi approximation.

The Gross–Pitaevski-type equation for the condensate (initially quiescent) in the second trap interacting

[1] This effect may occur for an arbitrary trap shape and will be considered elsewhere.

with the first trap is written as[2]

$$i\hbar\frac{\partial\Phi}{\partial t} = \left[-\frac{\hbar^2\nabla^2}{2m} + V_{2\text{ext}} - \mu_2 + gn_c + 2g\tilde{n} + \hat{U}_1\right]\Phi, \quad (3)$$

where

$$\hat{U}_1(\mathbf{r}) = \int\psi_1^\dagger(\mathbf{r}')U(\mathbf{r}-\mathbf{r}')\psi_1(\mathbf{r}')d\mathbf{r}', \quad (4)$$

$\psi_1^\dagger$ and ψ_1 are the field operators for the first (rotating) trap, μ_2 is the chemical potential, n_c is the condensate density, and $\tilde{n}$ is the density of noncondensed particles. The effective interaction constant g (and the ground state) in the two-dimensional Bose gas were studied in [6, 7]; the value of g is

$$g = \frac{2\sqrt{2\pi}\hbar^2}{m}\left[l_z/a - \frac{1}{\sqrt{2\pi}}\ln(\pi p_{12}^2 l_z^2)\right]^{-1}, \quad (5)$$

where $\mathbf{p}_{12} = (\mathbf{p}_1 - \mathbf{p}_2)/2$ is the relative momentum of two atoms, a is the s-scattering 3D amplitude, and $l_z = \sqrt{\hbar/m\omega_z}$. It was shown in [8] that the dependence on the relative momentum can be ignored in a rarefied Bose gas and the effective scattering length

$$\frac{2\pi\hbar^2}{m}\tilde{a} = \frac{2\sqrt{2\pi}\hbar^2}{m}a/l_z \quad (6)$$

can be introduced.

One can see from Eq. (3) that the influence of atoms of the first trap (where gas is rotated) on the second trap is reduced to the appearance of an auxiliary effective potential $U_1(\mathbf{r})$, which, in our approximation, is reduced to an addition to the confining potential $V_{2\text{ext}}$. To understand the character of the change in the state of the Bose condensate in the second trap, one should find the effective potential in explicit form. In the Thomas–Fermi approximation, it is written as

$$\hat{U}_1(\mathbf{r}) = \int n_{TF}(\mathbf{r}', t)U(\mathbf{r}-\mathbf{r}')d\mathbf{r}', \quad (7)$$

where

$$n_{TF}(\mathbf{r}', t) = \frac{\mu_1 - V_{1\text{ext}}(\mathbf{r}', t)}{g}. \quad (8)$$

As is seen from the formula for the density n_{TF}, the integration is over the region $V_{1\text{ext}}(\mathbf{r}, t) \le \mu$, which depends on t. To calculate this integral, let us pass to the rotating system of coordinates, where the first trap is at rest. As a result, the integration region is fixed in time, and the time dependence transfers to the interaction potential $U(\mathbf{r}-\mathbf{r}')$. Equation (7) can be rewritten in the following form:

$$\hat{U}_1(\tilde{x}, \tilde{y}) = \iint\frac{\alpha_6}{2g}\frac{(2\mu_1 - m\omega_{1x}^2x'^2 - m\omega_{1y}^2y'^2)}{((x'-\tilde{x})^2 + (y'-\tilde{y})^2 + D^2)^3}dxdy, \quad (9)$$

where $\tilde{x} = x\cos\Omega t - y\sin\Omega t$ and $\tilde{y} = x\sin\Omega t + y\cos\Omega t$. Since the interaction potential between the traps at a distance of $|\mathbf{r}-\mathbf{r}'| = D$ decreases almost by an order of magnitude: $U(0)/U(D) = 8$, it can be changed to a more convenient form,

$$U(\mathbf{r}-\mathbf{r}') = \begin{cases}\dfrac{\alpha_6}{D^5}, & \text{at } |\mathbf{r}-\mathbf{r}'| \le D\\ 0, & \text{at } |\mathbf{r}-\mathbf{r}'| > D.\end{cases} \quad (10)$$

Let the longitudinal size of the rotating trap be larger than the size of the second trap (in other cases, the results are qualitatively the same) and $D \ll R_{\text{tr}}$, where R_{tr} is the horizontal trap size. By calculating the induced potential (9), one obtains

$$\hat{U}_1(\tilde{x}, \tilde{y}) = \frac{\pi\alpha_6}{D^4 2g} \times\left[2\mu_1 - \frac{mD^2(\omega_{1x}^2 + \omega_{1y}^2)}{4} - m(\omega_{1x}^2\tilde{x}^2 + \omega_{1y}^2\tilde{y}^2)\right]. \quad (11)$$

Therefore, we see that the effect of the first trap U_1 changes both the chemical potential of the Bose gas and the effective confining potential in the second trap:

$$\mu_2^{\text{eff}} = \mu_2 + \frac{\pi\alpha_6}{D^4 2g}\left[2\mu_2 - \frac{mD^2(\omega_{1x}^2 + \omega_{1y}^2)}{4}\right], \quad (12)$$

$$V_{2\text{ext}}^{\text{eff}}(x, y) = \frac{m\omega_{2x}^2x^2}{2} + \frac{m\omega_{2y}^2y^2}{2} - \frac{\pi\alpha_6}{D^4 2g}[m(\omega_{1x}^2\tilde{x}^2 - \omega_{1y}^2\tilde{y}^2)]. \quad (13)$$

As a result, the equation for the Bose condensate in the second trap takes the form

$$i\hbar\frac{\partial\Phi}{\partial t} = \left[-\frac{\hbar^2\nabla^2}{2m} + V_{2\text{ext}}^{\text{eff}}(\mathbf{r}) - \mu_2^{\text{eff}} + gn_c + 2g\tilde{n}\right]\Phi. \quad (14)$$

Let us study the effective potential $V_{2\text{ext}}^{\text{eff}}(\mathbf{r})$ in more detail. It is quadratic with respect to x and y:

$$V_{2\text{ext}}^{\text{eff}}(x, y) = \frac{m}{2}(ax^2 + bxy + cy^2), \quad (15)$$

[2] Equation (3) is obtained from the set of two Gross–Pitaevski coupled equations for coupled traps. The influence of the second trap on the first rotating trap is negligible because the induced anisotropy of the second trap is small compared to its initial value.

where

$$a = \omega_{2x}^2 - \gamma(\omega_{1x}^2\cos^2\Omega t + \omega_{1y}^2\sin^2\Omega t),$$
$$c = \omega_{2y}^2 - \gamma(\omega_{1x}^2\sin^2\Omega t + \omega_{1y}^2\cos^2\Omega t),$$
$$b = \gamma(\omega_{1x}^2 - \omega_{1y}^2)\sin 2\Omega t,$$
$$\gamma = \pi\alpha_6/D^4 g.$$

Let us now consider the potential as a function of trap parameters.

I. Let both traps be isotropic; i.e., $\omega_{2x} = \omega_{2y} = \omega_2$ and $\omega_{1x} = \omega_{1y} = \omega_1$. Then, after substituting these parameters in Eq. (15), we obtain

$$V_{2\text{ext}}^{\text{eff}}(x, y) = \frac{m}{2}(\omega_2^2 - \gamma\omega_1^2)(x^2 + y^2). \quad (16)$$

Therefore, we see that the effective confining potential is merely deformed as $\omega_2^{\text{eff}} = \sqrt{\omega_2^2 - \gamma\omega_1^2}$. No drag effect occurs. This is what is expected, because the distribution of atoms in the rotating Bose condensate is not anisotropic.

II. If $\omega_{1x} \neq \omega_{1y}$, the effect is basically different. Let us turn our system of coordinates in such a way that the cross product disappears. The rotation angle φ can be found from the equation $\tan 2\varphi = b/(c - a)$. The effective confining potential in the new system of coordinates has the form

$$V_{2\text{ext}}^{\text{eff}}(\tilde{x}, \tilde{y}) = \frac{m}{2}(\tilde{\omega}_{2x}^2\tilde{x}^2 + \tilde{\omega}_{2y}^2\tilde{y}^2), \quad (17)$$

where

$$\tilde{\omega}_{2x}^2 = a\cos^2\varphi + c\sin^2\varphi - b\cos\varphi\sin\varphi,$$
$$\tilde{\omega}_{2y}^2 = a\sin^2\varphi + c\cos^2\varphi + b\cos\varphi\sin\varphi. \quad (18)$$

Thus,

$$\tan 2\varphi = \frac{\sin 2\Omega t}{\beta + \cos 2\Omega t}, \quad (19)$$

where $\beta = (\omega_{2y}^2 - \omega_{2x}^2)/\gamma(\omega_{1y}^2 - \omega_{1x}^2)$. Let us consider two cases.

(a) If $\omega_{2x} = \omega_{2y} = \omega_2$, then $\beta = 0$. Then, we obtain the expressions for the rotation angle φ of the system of coordinates and the angular velocity $\Omega_2 = \dot{\varphi}$ of the second trap: $\varphi = \Omega t$ and $\Omega_2 = \Omega$. One can then see that, if the second trap is initially isotropic in the *xy* plane, then its effective confining potential (17) is deformed (with the coefficients $\tilde{\omega}_{2x} = \sqrt{\omega_2^2 - \gamma\omega_{1x}^2}$ and $\tilde{\omega}_{2y} = \sqrt{\omega_2^2 - \gamma\omega_{1y}^2}$) due to the effect of the first trap, becomes anisotropic, and rotates with the angular velocity of the first trap.

Let us now find the drag coefficient (mutual moment of inertia) J_{21}. The moment of inertia of a gas, in accordance with the theory of linear response, characterizes the response to the perturbation $-\Omega\hat{J}_z$ in the Hamiltonian of the system and is determined by the relation

$$\Theta = \frac{\langle\hat{J}_z\rangle}{\Omega}, \quad (20)$$

between the mean angular momentum $\langle\hat{J}_z\rangle$ and angular velocity Ω. In [9], it was found that, at small angular velocities Ω and in the absence of noncondensed component (i.e., at $T = 0$), the moment of inertia of the trap is

$$\Theta = \left[\frac{\omega_x^2 - \omega_y^2}{\omega_x^2 + \omega_y^2}\right]^2\Theta_{\text{rig}}, \quad (21)$$

where $\Theta_{\text{rig}} = mN\langle x^2 + y^2\rangle$ is the moment of inertia of a solid body with the trap parameters ω_x, ω_y. Substituting into this formula the effective frequencies of the confining potential of the second trap, we obtain

$$J_{21} = \gamma^2\left[\frac{\omega_{1x}^2 - \omega_{1y}^2}{2\omega_2^2 - \gamma(\omega_{1x}^2 + \omega_{1y}^2)}\right]^2\Theta_{\text{rig}}. \quad (22)$$

At $\gamma \ll 1$, the mutual drag coefficient is

$$J_{21} = \gamma^2\frac{[\omega_{1x}^2 - \omega_{1y}^2]^2}{4\omega_2^4}\Theta_{\text{rig}}. \quad (23)$$

(b) If $\omega_{2x} \neq \omega_{2y}$, i.e., the upper (second) trap is initially anisotropic, then $\beta \neq 0$. This signifies that the angular velocity Ω_2 of the upper trap and the parameters $\tilde{\omega}_{2x}$ and $\tilde{\omega}_{2y}$ of the effective confining potential depend on time. Let us consider the possible values of β.

(b1) At $\beta > \beta_0$, the motion of the confining potential of the second trap is oscillatory. The value of β_0 is found from the condition $\tilde{\omega}_{2x}(t) > \tilde{\omega}_{2y}(t)$. Hence, $\beta_0 = \sqrt{2}$. The angle of rotation φ changes within the limits

$$-\frac{1}{2}\arctan\left(\frac{1}{\sqrt{\beta^2 - 1}}\right) < \phi < \frac{1}{2}\arctan\left(\frac{1}{\sqrt{\beta^2 - 1}}\right). \quad (24)$$

The time dependence of angle $\varphi(t)$ is shown in Fig. 1. The parameters of the effective confining potential change in accordance with Eqs. (18). The quantities $\tilde{\omega}_{2x}(t)$ and $\tilde{\omega}_{2y}(t)$ depend on time periodically with the rotation period of the lower trap $T = 2\pi/\Omega$ (Fig. 2).

(b2) At $0 < \beta < \beta_0$, the motion is more complicated; the effective confining potential of the lower trap rotates with a variable angular velocity $\Omega_2(t)$, and its parameters $\tilde{\omega}_{2x}(t)$ and $\tilde{\omega}_{2y}(t)$ also oscillate (out of phase) with frequency Ω about their mean values.

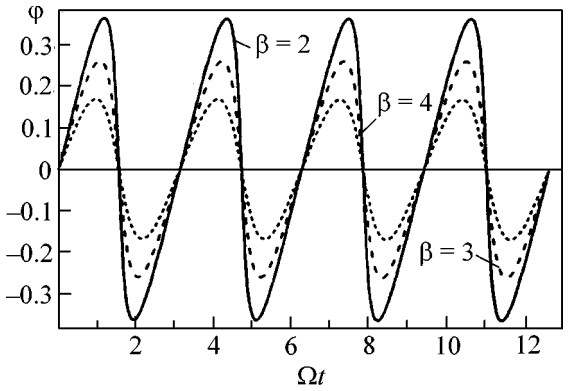

Fig. 1. The trap rotation angle as a function of time for different β = 2, 3, and 4.

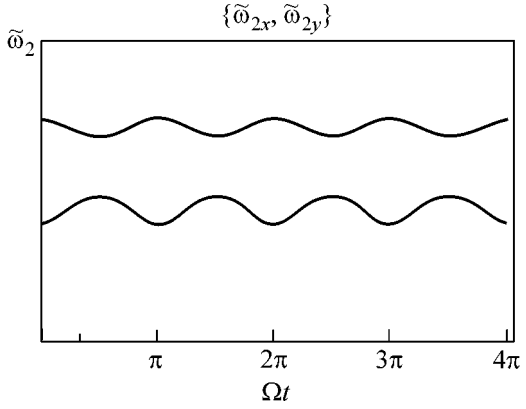

Fig. 2. The effective frequencies of confining potential as a function of time for β ~ 4.

Thus, one can distinguish four rotation regimes of the confining potential for the lower trap:

I. β = 0 (the lower trap is initially isotropic); the atoms in the lower trap rotate with a constant velocity and time-independent parameters.

II. $\beta \ll 1$ (weak anisotropy of the lower trap); the atoms in the lower trap rotate with the angular velocity $\Omega_2(t) = \Omega[1 - \beta\cos(2\Omega t)]$.

III. $\beta \gg 1$ (strong anisotropy of the lower trap); the atoms in the lower trap rotate following the law $\varphi(t) = \frac{1}{2}\frac{\sin(2\Omega t)}{\beta}$.

IV. Other values of β correspond to the intermediate regime.

Let us now make numerical estimates for the coefficient γ. Take Na^{23} atoms as an example, for which the *s*-scattering length is $a = 2.8$ nm.[3] For $\hbar\omega_0 = 7$ nK (this corresponds to the frequency of the confining potential in the *xy* plane $\omega_0 = 2\pi \times 145$ rad/s) and $\omega_z = 10^3\omega_0$, the effective scattering length is $\tilde{a} = 0.041$. The van der Waals interaction constant for Na is $\alpha_6 \approx 3000$ au, where 1 au = 1 a.e. $= e^2 a_0^5 = 0.903 \times 10^{-60}$ erg cm. Then, the coefficient γ is

$$\gamma = 1.2 \times 10^{-24}/D^4. \quad (25)$$

For distances on the order of $D \sim 10^{-5}$ cm, $\gamma \sim 10^{-4}$.

This work was supported by the Russian Foundation for Basic Research and INTAS.

REFERENCES

1. M. H. Anderson *et al.*, Science **269**, 198 (1995).
2. C. C. Bradley *et al.*, Phys. Rev. Lett. **75**, 1687 (1995).
3. K. B. Davis *et al.*, Phys. Rev. Lett. **75**, 3969 (1995).
4. F. Dalfovo, S. Giorgini, L. P. Pitaevskii, and S. Stringari, Rev. Mod. Phys. **71**, 463 (1999).
5. L. P. Pitaevskiĭ, Usp. Fiz. Nauk **168**, 641 (1998) [Phys. Usp. **41**, 569 (1998)].
6. Yu. E. Lozovik and V. I. Yudson, Physica A (Amsterdam) **3**, 493 (1978).
7. D. S. Petrov, M. Holzmann, and G. V. Shlyapnikov, Phys. Rev. Lett. **84**, 2551 (2000).
8. B. P. van Zyl, R. K. Bhaduri, and J. Sigetich, cond-mat/0106410.
9. F. Zambelli and S. Stringari, Phys. Rev. A **63**, 033602 (2001).

Translated by V. Sakun

[3] Similar effects can occur for the excitonic traps (the corresponding exciton confinement may occur in a system of quantum dots, due to inhomogeneous strain, to special potential profile, etc.).

JETP Letters, Vol. 76, No. 3, 2002, pp. 139–142. Translated from Pis'ma v Zhurnal Éksperimental'noĭ i Teoreticheskoĭ Fiziki, Vol. 76, No. 3, 2002, pp. 171–175.

Generation of High-Energy Negative Hydrogen Ions upon the Interaction of Superintense Femtosecond Laser Radiation with a Solid Target

R. V. Volkov[1], V. M. Gordienko[1], I. M. Lachko[1], P. M. Mikheev[1], B. V. Mar'in[2], A. B. Savel'ev[1]*, and O. V. Chutko[1]

[1] *International Laser Center, Faculty of Physics, Moscow State University, Moscow, 119992 Russia*
**e-mail: savelev@femto.phys.msu.su*
[2] *Nuclear Physics Institute, Moscow State University, Vorob'evy gory, Moscow, 119992 Russia*
Received June 24, 2002

The formation of a high-energy (~35 keV) beam of negative hydrogen ions was observed in the expanding femtosecond laser plasma produced at the surface of a solid target by radiation with an intensity of up to 2×10^{16} W/cm^2. The energy spectra of the H^+ and H^--ions show a high degree of correlation. © *2002 MAIK "Nauka/Interperiodica".*

PACS numbers: 52.50.Jm; 79.20.Ds; 52.70.Nc

1. In recent years, there has been extensive discussion on the possibility of obtaining high-intensity ion (primarily proton) beams using laser plasma produced upon the interaction of femtosecond pulses with solid targets [1–6]. Such beams can be used for isotope separation, the initiation of nuclear and fusion reactions, etc. [7]. The energy of protons accelerated at the plasma–vacuum boundary equals [1, 7]

$$E \approx m_e c^2 \pi \sqrt{Q\delta r/\lambda} \qquad (1)$$

[δ is the hot-electron conversion ratio, $Q = I\lambda^2/(5.48 \times 10^{18}$ W/cm^2 μm^2), λ is the laser wavelength, m_e is the electron mass, and r is the radius of focal spot] and can be as high as 10 MeV for intensities higher than 10^{20} W/cm^2 [2]. Ions with energies of tens of kiloelectronvolts are observed even at "moderate" pulse intensities $I < 2 \times 10^{16}$ W/cm^2 [3, 4].

This work reports on the observation of high-energy negative hydrogen ions from plasma produced at the surface of an Si target by laser pulses with intensities of up to 2×10^{16} W/cm^2.

2. The experimental scheme is shown in Fig. 1. Laser radiation (wavelength 616 nm and pulse duration 200 fs) was focused onto a target by lens *1* with $F/D \sim 6$ providing an intensity of 2×10^{16} W/cm^2 [8]. The vacuum chamber consisted of two sectors joined together by a tube: interaction chamber *3* and recording chamber *4*. Residual pressure in the chamber was less than 10^{-5} torr. The accuracy of focusing laser radiation onto the target and the temperature of the hot electronic plasma component were monitored by the hard X-ray plasma radiation yield using a set of photomultipliers with a NaJ scintillator [4].

The plasma ion and electron currents were measured by an energy-resolving time-of-flight spectrometer [9] placed in the recording chamber normally to the target surface at a distance of 50 cm. The spectrometer was a cylindrical capacitor with a deflection angle of 180° and an average radius of 8 cm. The potential difference U between the capacitor plates was smoothly varied from –8 to 8 keV, allowing the detection of either positively or negatively charged particles. The acceptance angle was 5×10^{-4} sr. The particle flow pulse passed through the spectrometer was detected using a VEU-7 multiplier, whose signal was fed through a load

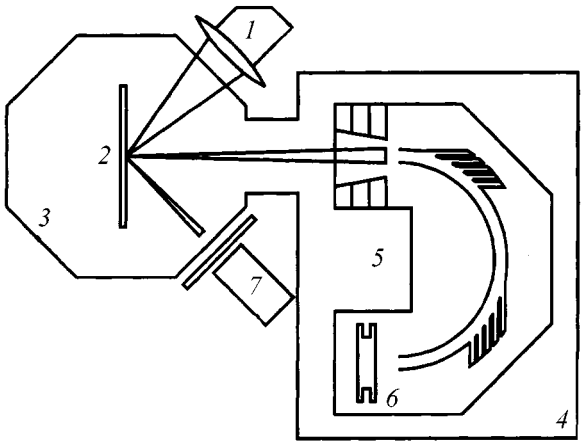

Fig. 1. Schematic of experimental setup; (*1*) lens, (*2*) target, (*3*) interaction chamber, (*4*) recording chamber, (*5*) spectrometer, (*6*) VEU-7, and (*7*) photomultiplier set.

0021-3640/02/7603-0139$22.00

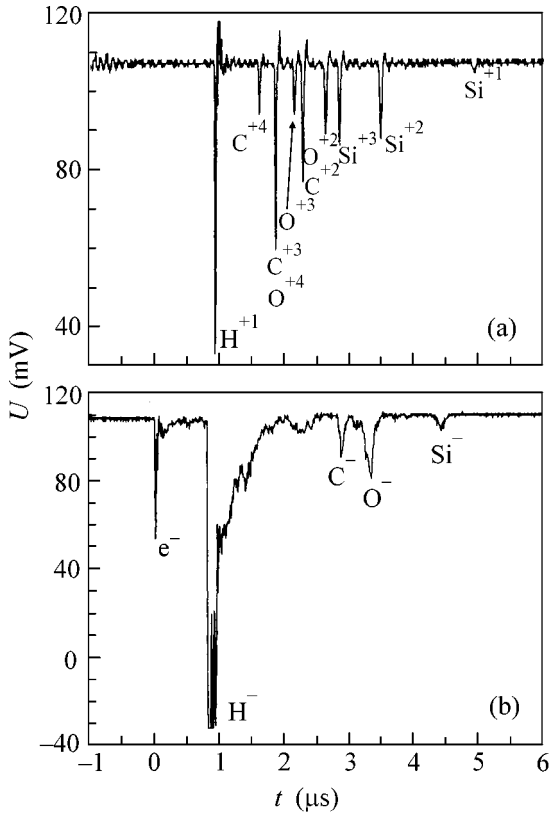

Fig. 2. Time dependence of the arrival instant for (a) positively and (b) negatively charged plasma components with energy of, respectively, 2.8*Z* keV and 3.5*Z* keV.

of 50 Ω, into a digital oscillograph with a time resolution of 10 ns.

The spectrometer was calibrated using an electron gun emitting a quasi-monoenergetic electron beam. Measurements were made in the electron-energy range up to 4 keV and demonstrated that the electron energy *E* depended linearly on the voltage *U*, with the proportionality coefficient

$$k = 0.23 \pm 0.005 \quad [\text{V/eV}], \qquad (2)$$

and the spectrometer resolution was $\Delta E/2E = 4\%$. Therefore, the spectrometer could detect charged particles with an energy of up to 35*Z* keV (*Z* is the particle charge).

The typical form of a signal recorded in the regime of measuring positively and negatively charged plasma components is given in Fig. 2a ($E = 2.8Z$ keV) and Fig. 2b ($E = 3.5Z$ keV), respectively. It is worth noting that for the current of negatively charged particles the voltage on VEU-7 increased from 1.2 to 2.5 keV, which corresponded to an increase in gain of no less than 10^3 times. As was expected, at positive values of *U*, the signal showed several peaks, each corresponding to ions with a different charge-to-mass ratio *Z*/*M* but the same energy per charge unit *E*/*Z*. Indeed, at a fixed *U*, the time between particle arrival and plasma ignition is

$$t = l\sqrt{M/Z}\sqrt{k/2U},$$

where *l* is the length of time-of-flight base, *M* is the ion mass, *Z* is the ion charge in units of electron charge. The first and most pronounced peak appears at times on the order of 1 μs after plasma ignition. It is formed by proton current, for which *Z*/*M* is maximal. This is confirmed by the estimate of the entire ion flight length *l* from the arrival time *t* of the first peak as a function of potential difference *U*: $l \sim 73 \pm 0.7$ cm, with the expected $l = 72$ cm. The presence of protons in the expanding laser plasma is due to the presence of hydrogen-containing impurities (in particular, water) at the surface of the silicon target. The next peaks are due to the heavier Si, O, and C ions of different state of ionization. The presence of the O and C ions can be due to the ingress of organic compounds and oil vapor from the vacuum pump into the chamber.

As the potential *U* increases, the number of fast protons with energies of up to 35 keV becomes noticeable. To construct the proton energy spectra, we measured plasma current over a wide range of *U* values. The resulting proton maxima were integrated over a peak and normalized to the absolute transmission energy width proportional to the deflecting voltage *U*. The maximal proton energy was as high as 35 keV and determined by the spectrometer range. At energies higher than 3 keV, the proton spectrum is well approximated by the exponential function with a "temperature" of 8 keV, in accordance with a temperature of 4.5 ± 0.8 keV estimated for hot electrons by measuring the hard X-ray plasma radiation yield [4]. Therefore, the proton acceleration is primarily due to the presence of a hot electron component in plasma. Note that the estimation of proton energy by Eq. (1) gives 9 keV ($\delta = 0.01$, $r = 1.5$ μm, $Q = 0.0014$).

As is mentioned above, the typical signal shape for negative particles leaving plasma is shown in Fig. 2b. The first signal, which is at times smaller than 100 ps, corresponds to the arrival of the electron at the detector. We also observed the subsequent peaks corresponding to other negative particles with a delay time longer than 100 ns.

A detailed analysis of the amplitude and time position of the second peak as functions of voltage *U* (Fig. 2b) suggests that this peak coincides in time with the proton peak for the same, though positive value of *U*. Thus, the *Z*/*M* ratio for this peak equals –1; i.e., it is due to the negative hydrogen ions. At the same time, with allowance made for an increase in the VEU-7 gain, the peak amplitude is substantially lower than for the proton peak. The maximum energy of the negative ions H^{-1} was equal to 35 keV, as for protons.

The energy spectrum of negative hydrogen ions, as obtained by analogy with the proton spectrum, is shown in Fig. 3. It is characterized by a high degree of correlation with the proton energy spectrum. The temperature of negative ions is also equal to 8 keV, their maxi-

mal energy is the same, etc. This suggests that the negative hydrogen ions appear upon the recombination of rapidly cooled expanding plasma. Note that the ionic flow of negative plasma particles (Fig. 2b) also shows peaks corresponding to singly charged silicon, oxygen, and carbon ions.

The experiments with lower laser intensities demonstrated that the number of negative ions rapidly increases with increasing intensity. The negative ions were not detected by our spectrometer at an intensity of 10^{14} W/cm^2. At the same time, the proton signal was detected with certainty at this intensity, and the maximum proton energy was found to be 2 keV.

3. The formation of negative ions in the expanding laser plasma jet was earlier observed in [10, 11] in experiments with irradiation of solid targets by nanosecond pulses with an intensity of less than 10 GW/cm^2. Under these conditions, the equilibrium plasma temperature $T \approx 1$ eV corresponds to the electron affinity ϵ_A for an atom (for hydrogen, $\epsilon_A \approx 0.75$ eV [12]) and provides the efficient formation of negative ions. However, because of the low initial plasma temperature, the kinetic energy of negative ions appearing in plasma is lower than 4 eV. As the intensity of the nanosecond laser pulse increases, the kinetic energy of the negative ions increases and they are formed less efficiently [10]. The maximal velocity of the negative ions detected in this interaction regime does not exceed 10^5 cm/s.

A different situation occurs in plasma formed by a femtosecond pulse ($I \sim 10^{16}$ W/cm^2). In this case, the plasma electrons are heated with a rate of 1–10 keV/ps, whereupon the plasma layer is rapidly cooled as a result of expansion into vacuum and heat outflow into the target [13]. In this case, the plasma expansion velocity may be as high as $v_a \approx 5 \times 10^7$ cm/s, and the ion kinetic energy increases to 1–10 keV/nucleon. Since the radius r of a plasma spot is much greater than its thickness H, the expansion at the initial stage has a one-dimensional character. This expansion regime becomes three-dimensional at times $\tau = 2r/v_a \approx 10$ ps, when the plasma becomes equilibrium. Calculations with the one-dimensional model showed [14] that the plasma cools down in this time interval to a temperature on the order of 30–100 eV. Thus, the metastable negative ions can appear only at longer times.

The dynamics of three-dimensional plasma expansion can be described using the self-similar solution for the adiabatic expansion of a gaseous sphere into vacuum [15]. In this case, the particle concentration n at any time instant is

$$n = n_0(R_0/R)^3, \tag{3}$$

where n_0 and R_0 are, respectively, the initial concentration and radius of the plasma sphere and $R = t\sqrt{2ZT_0/M}$ is its characteristic size (t is time and T_0 is the initial plasma temperature). The temperature T depends on time as

$$T(t) = T_0(R_0/R(t))^{3(\gamma-1)} \tag{4}$$

($\gamma = c_p/c_v$).

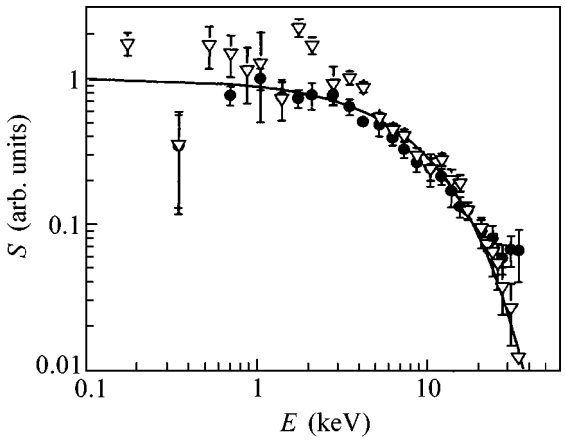

Fig. 3. Normalized spectra of (●) protons and (▽) negative hydrogen ions and (solid line) their exponential approximation with an exponent of 8 keV.

Because we consider the formation of negative ions in a hot ($T_0 \sim 100$ eV) laser plasma expanding into vacuum, the necessary conditions for the formation and existence of negative ions occur at rather long times when the plasma temperature drops to several electron-volts. In turn, the recombination of negative ions is decelerated because of the low concentration of electrons and positive ions in expanding plasma. For low plasma temperatures ($T \ll 2$ eV), the recombination rate in collisions with ions is given by the formula [16]

$$k_i \approx 7 \times 10^{-10} n_i/\sqrt{\epsilon_A T\mu} \ \text{ s}^{-1}, \tag{5}$$

where T and ϵ_A are in electron-volts, μ is the reduced mass of colliding ions in units of proton mass, and n_i is the concentration of positive ions. The recombination rate in electron collisions can be estimated using the modified Seaton formula for the electron-impact ionization rate [17]

$$k_e \approx 2 \times 10^{-6} Z n_i \frac{T}{\epsilon_A^2} \exp\left(-\frac{\epsilon_A}{T}\right) \ \text{s}^{-1}. \tag{6}$$

The dependences of k_i and k_e on the distance to the target, as obtained according to Eqs. (3)–(6) on the assumption that the initial plasma temperature is 100 eV and the initial ion concentration in plasma is 5×10^{22} cm^{-3}, are given in Fig. 4. The left boundary on the abscissa axis corresponds to the time instant at which the plasma temperature becomes lower than 2 eV. One can see from the figure that the negative hydrogen ions mainly recombine in the collisions with silicon ions, and the recombination rate becomes lower than 10^6 s^{-1}

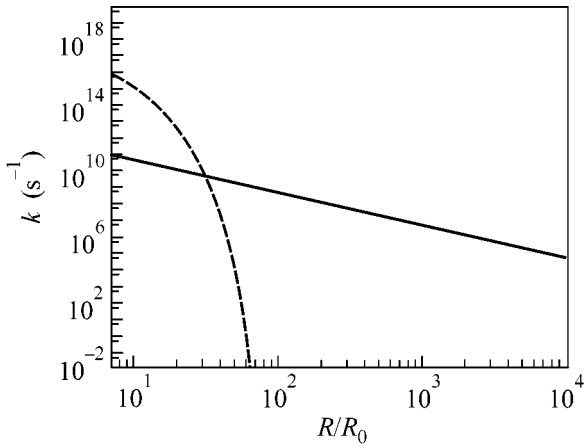

Fig. 4. Recombination rate of negative ions as a function of the distance from the target, according to Eqs. (5) and (6). The solid line corresponds to k_i; the dashed line, to k_e.

at distances of $2 \times 10^3 R_0$; for $R_0 \sim 10$ μm, this is equal to several centimeters.

Therefore, the interaction of a femtosecond laser pulse with a target surface at a pulse intensity higher than 10^{15} W/cm^2 gives rise at times on the order of 1 ns to a plasma jet with ion velocities higher than 10^7 cm/s, a plasma temperature on the order of 1 eV, and a negative-ion lifetime of tens and hundreds of microseconds. The reasons for the increase in the efficiency of generating negative ions with increasing intensity may be the following. At low pulse intensity, the initial equilibrium plasma temperature is not high, and, hence, the "optimal" temperature for the formation of negative ions is achieved at the earlier expansion stage with higher electron and ion densities, when the lifetimes of negative ions are substantially shorter than 1 μs. By the time instant when the plasma density becomes sufficiently low, the temperature becomes lower than 0.1 eV and the formation efficiency of the negative ions is reduced. A detailed analysis of the formation of negative ions in an expanding plasma jet produced by a femtosecond pulse should be carried out within the framework of a consistent three-dimensional plasma-expansion model taking into account a number of processes such as the recombination, heat conductivity, etc.

4. In summary, femtosecond laser plasma is a unique source of fast negative ions. The energy of negative hydrogen ions can be as high as 35 keV at a laser intensity of 2×10^{16} W/cm^2. The spectra of negative ions also have singly charged ions of other atoms: oxygen, carbon, and silicon. The effect substantially depends on the conditions for the formation of a hot dense plasma, because the negative ions are detected only at intensities higher than the threshold of femtosecond plasma formation (10^{15} W/cm^2). In this connection, of great interest is the study of this effect for laser intensities approaching the relativistic limit 5×10^{18} cm^{-3}, because the energy of negative ions may achieve a value of MeV/nucleon. At the same time, the plasma heating, cooling, and recombination dynamics greatly changes at such intensities; this can also affect the formation of negative ion beams. It also seems that the observed effect holds promise for the creation of primary ion beam in particle accelerators [18] and in the evaporation of superthin films, nanostructures [19], etc.

This work was supported by the Russian Foundation for Basic Research (project nos. 00-02-17302, 02-02-16659, 02-02-06104, and 02-02-06236) and the State Scientific and Technical Program "Fundamental Metrology."

REFERENCES

1. A. Maksimchuk, S. Gu, K. Flippo, and D. Umstadter, Phys. Rev. Lett. **84**, 4108 (2000).
2. M. D. Perry, J. A. Sefcick, T. Cowan, *et al.*, Rev. Sci. Instrum. **70**, 265 (1999).
3. J. Badziak, W. Woryna, P. Parys, *et al.*, Phys. Rev. Lett. **87**, 215001 (2001).
4. R. V. Volkov, D. M. Golishnikov, V. M. Gordienko, *et al.*, Kvantovaya Élektron. (Moscow) **31**, 241 (2001).
5. E. L. Clark, K. Krushelnik, M. Zepf, *et al.*, Phys. Rev. Lett. **85**, 1654 (2000).
6. S. C. Wilks, A. B. Langdon, T. E. Cowan, *et al.*, Phys. Plasmas **8**, 542 (2001).
7. A. V. Andreev, V. M. Gordienko, and A. B. Savel'ev, Kvantovaya Élektron. (Moscow) **31**, 941 (2001).
8. R. V. Volkov, V. M. Gordienko, M. S. Dzhidzhoev, *et al.*, Kvantovaya Élektron. (Moscow) **24**, 1114 (1997).
9. N. G. Basov, Yu. A. Zakharenkov, A. A. Rupasov, *et al.*, *Diagnostics of Dense Plasma* (Nauka, Moscow, 1989).
10. Yu. A. Bykovskiĭ, V. I. Romanyuk, and S. M. Sil'nov, Pis'ma Zh. Tekh. Fiz. **14**, 927 (1988) [Sov. Tech. Phys. Lett. **14**, 410 (1988)].
11. S. V. Latyshev, Zh. Tekh. Fiz. **67** (7), 117 (1997) [Tech. Phys. **42**, 828 (1997)].
12. B. M. Smirnov, *Negative Ions* (Atomizdat, Moscow, 1973; McGraw-Hill, New York, 1982).
13. V. T. Platonenko, Laser Phys. **2**, 852 (1992).
14. V. M. Gordienko, M. A. Joukov, and A. B. Savel'ev, in *Application of High Field and Short Wavelength Sources*, Ed. by L. DiMauro, M. Murnane, and A. H'Huiller (Plenum, New York, 1998), p. 155.
15. Ya. B. Zel'dovich and Yu. P. Raizer, *Physics of Shock Waves and High-Temperature Hydrodynamic Phenomena* (Nauka, Moscow, 1966; Academic, New York, 1966).
16. B. M. Smirnov, *Ions and Excited Atoms in Plasma* (Atomizdat, Moscow, 1974).
17. I. I. Sobelman, L. A. Vainshtein, and E. A. Yukov, *Excitation of Atoms and Broadening of Spectral Lines* (Nauka, Moscow, 1979; Springer-Verlag, Berlin, 1981).
18. G. I. Dimov, Rev. Sci. Instrum. **67**, 3393 (1996).
19. G. Korschinek and T. Henkelman, Rev. Sci. Instrum. **63**, 2672 (1992).

Translated by V. Sakun

JETP Letters, Vol. 76, No. 3, 2002, pp. 143–146. Translated from Pis'ma v Zhurnal Éksperimental'noĭ i Teoreticheskoĭ Fiziki, Vol. 76, No. 3, 2002, pp. 176–180.

Electromagnetically Induced Acoustic Transparency and Absorption

S. V. Sazonov

Kaliningrad State University, Kaliningrad, 236041 Russia

** e-mail: sazonov@phys.tsu.ru, nst@alg.kaliningrad.ru*

Received June 6, 2002

The possibility of controlling the passage (from transmission to absorption) of a hypersound through a low-temperature paramagnet using the resonance electromagnetic pumping of lower frequency is substantiated. The effect has a quantum nature and is analogous to (though somewhat different from) the optical phenomenon of electromagnetically induced transparency. © *2002 MAIK "Nauka/Interperiodica".*

PACS numbers: 43.35.Gk; 42.50.Gy

An analysis of the physics of coherent processes indicates that microwave and optical coherent effects have found acoustic analogues several years after their discovery. This conclusion is confirmed, e.g., by quantum acoustic phenomena such as acoustic paramagnetic resonance (APR) [1] [analogue of electron paramagnetic resonance (EPR)], phonon echo [2], and acoustic self-induced transparency [3–5]. Acoustic fields usually act on electron and nuclear spins at low and superlow temperatures [6, 7]. At liquid helium temperatures ($T \sim 1$ K), the self-absorption of hypersound with a frequency of ~10 GHz due to anharmonicity, defects, etc., is appreciably lower than the resonance absorption [1] and, hence, can be ignored.

The discovery of electromagnetically induced transparency (EIT) [8, 9] consisting in a sharp bleaching of a three-level resonance medium for a weak optical signal at the center of absorption line and in an appreciable decrease in its group velocity in the presence of a powerful optical pumping has given impetus to the vigorous development of fundamental and applied areas of research associated with this effect [10, 11].

On the basis of this parallel, one can conclude that a search for the effect of acoustic induced transparency (AIT) in a system of electron (or) nuclear spins is also reasonable. Considering that both EPR and APR transitions can occur between the Zeeman sublevels in an external magnetic field, one can assume that AIT may occur upon the combined (electromagnetic and acoustic) action on a crystal. Note that, contrary to optical transitions, the resonance absorption line profile for Zeeman transitions is mainly due to inhomogeneous broadening [6]. This fact, in turn, should cause certain distinctions between AIT and EIT, which will be established below.

It is well known that Group VIII paramagnetic ions with spin $S = 1$ interact with lattice vibrations the most strongly [1, 6]. Due to the Zeeman effect in an external magnetic field $\mathbf{B}_0$, a three-level equidistant quantum state is formed. The equidistance can be eliminated, e.g., by applying a static strain $\epsilon_{zz}^{(0)}$ along $\mathbf{B}_0$ (z axis) [1, 12]. Below, we consider a system of such ions diluted as impurities in a cubic crystal. Let $\mathbf{B}_0$ be directed along one of the fourfold symmetry axes. In this case, the longitudinal hypersound signal propagates perpendicularly to $\mathbf{B}_0$ (along the x axis, which is also a fourfold axis) and the electromagnetic microwave pumping proceeds along $\mathbf{B}_0$ (Fig. 1).

Then, the Hamiltonian of a spin interacting with the acoustic and electromagnetic fields can be written as [1, 3, 6, 12]

$$\hat{H}_s = \hbar\omega_0\hat{S}_z + \frac{3}{2}G_{11}(\hat{S}_z^2\epsilon_{zz}^{(0)} + \hat{S}_x^2\epsilon_{xx}) - g\mu_B(\hat{S}_xB_x + \hat{S}_yB_y), \quad (1)$$

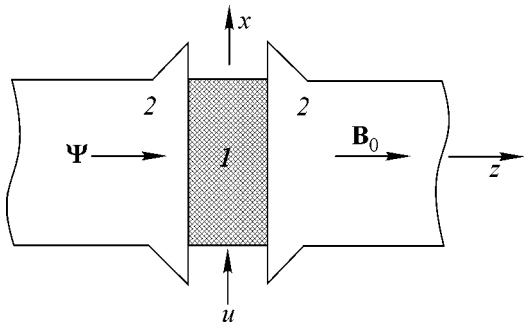

Fig. 1. Geometry of the assumed experiment. (*1*) Paramagnetic sample, (*2*) dielectric material (transparent to the electromagnetic pumping) producing static strain; $u \longrightarrow$ and $\psi \longrightarrow$ indicate the propagation directions for the hypersound and electromagnetic pumping, respectively.

where $\hbar$ is the Planck's constant, μ_B is the electron Bohr magneton, g is the Lande splitting factor, $\omega_0 = g\mu_B B_0/\hbar$ is the Zeeman frequency in the field $\mathbf{B}_0$, G_{11} is the tensor component of the spin–phonon interaction connecting the paramagnetic ion with the longitudinal strain component [1, 3, 6], $\epsilon_{xx} = \partial u/\partial x$ is the relative crystal strain caused by the hypersound, u is the corresponding displacement of lattice sites, B_x and B_y are the components of a magnetic field of microwave pumping, and the expressions for spin matrices in this geometry are

$$\hat{S}_x = \frac{1}{2}\begin{pmatrix} 0 & 1 & 0 \\ 1 & 0 & 1 \\ 0 & 1 & 0 \end{pmatrix}, \quad \hat{S}_y = \frac{i}{\sqrt{2}}\begin{pmatrix} 0 & -1 & 0 \\ 1 & 0 & -1 \\ 0 & 1 & 0 \end{pmatrix}, \quad \hat{S}_z = \begin{pmatrix} 1 & 0 & 0 \\ 0 & 0 & 0 \\ 0 & 0 & -1 \end{pmatrix}. \tag{2}$$

Note that the spin–phonon interaction that is linear in spin for $S = 1$ is one or two orders of magnitude weaker than the quadratic interaction [6] and is ordinarily ignored.

Hamiltonian (1) should be supplemented by the Hamiltonian of classical hypersound field

$$H_a = \frac{1}{2}\int [p^2/\rho + \rho a^2(\partial u/\partial x)^2]d^3\mathbf{r}, \tag{3}$$

where ρ is the average crystal density, a is the velocity of longitudinal sound in the absence of paramagnetic impurities, and p is the momentum density of the oscillating crystal sites.

In accordance with the semiclassical approach [12–14], the equations of motion for the acoustic field can be written as

$$\dot{u} = \delta H/\delta p, \quad \dot{p} = -\delta H/\delta u, \qquad H = H_a + \sum_j \langle \hat{H}_s \rangle, \tag{4}$$

where $\langle \hat{H}_s \rangle = \mathrm{Sp}(\hat{\rho}\hat{\xi}_s)$ is the quantum average of $\hat{H}_s$ and $\hat{\rho}$ is the density matrix of effective spin with dimensionality 3×3; the summation is over all paramagnetic ions [the index j in Eq. (1) is omitted]. Hereafter, the partial time derivative is indicated by an upper dot.

From Eqs. (1)–(4), one finds

$$\ddot{\Omega} - a^2\frac{\partial^2\Omega}{\partial x^2} = \frac{9G_{11}^2 n}{8\hbar\rho}\frac{\partial^2}{\partial x^2} \times \int_{-\infty}^{+\infty} (\rho_{22} + \rho_{31} + \rho_{31}^*) f(\Delta)d\Delta, \tag{5}$$

where $\Omega = (3G_{11}/4\hbar)\epsilon_{xx}$, $n = \sum_j \sigma(\mathbf{r} - \mathbf{r}_j)$ is the concentration of paramagnetic ions, $\delta(\mathbf{r} - \mathbf{r}_j)$ is the delta function, $\mathbf{r}$ is the coordinate of the jth ion, and $\Delta = \omega_{310}^{(0)} - \omega_{31}$ is the detuning of the hypersound frequency ω_{31} from the central frequency $\omega_{310}^{(0)}$ of the inhomogeneous contour $f(\Delta)$for the $1 \longleftrightarrow 3$ transition.

The dynamics of effective spin will be described quantum-mechanically using Neumann equation for $\hat{\rho}$ with Hamiltonian (1). In so doing, we use the following representation:

$$\Omega = u\exp[i(\omega_{31}t - k_{31}x)] + \text{c.c.}, \quad g\mu_B(B_x + iB_y)/\hbar = \psi\exp(i\omega_{32}t),$$
$$\rho_{31} = R_{31}\exp[-i(\omega_{31}t - k_{31}x)], \quad \rho_{32} = R_{32}\exp[-i(\omega_{32}t)],$$
$$\rho_{21} = R_{21}\exp\{-i[(\omega_{31} - \omega_{32})t - k_{31}x]\}. \tag{6}$$

Here, u and ψ are the real Rabi frequencies of the longitudinal hypersound and the circularly polarized microwave pumping resonant with, respectively, $1 \longleftrightarrow 3$ and $2 \longleftrightarrow 3$ transitions; R_{31}, R_{32}, and R_{21} are the slowly varying amplitudes (in the standard meaning) of the respective density matrix elements, k_{31} is the acoustic wavenumber for the frequency ω_{31} close to the frequency $\omega_{310} = 2\omega_0$; the pump frequency ω_{31}, according to the resonance conditions, is close to $\omega_{320} = \omega_0 + (3G_{11}/2\hbar)\epsilon_{zz}^{(0)}$, and the frequency of the inactive $1 \longleftrightarrow 2$ transition is expressed as $\omega_{210} = \omega_0 - (3G_{11}/2\hbar)\epsilon_{zz}^{(0)}$. From Eqs. (6), one can see that the term ρ_{22} on the right-hand side of Eq. (5) can be ignored.

In Eq. (6), the electromagnetic wavenumber for the frequency ω_{32} is taken to be zero, because the corresponding wavelength $\lambda = 2\pi c/\omega_{32} \sim l_x \gg l_z$, where $l_x(l_z)$ is the size of paramagnetic sample across (along) the magnetic field. Indeed, one ordinarily has in the APR experiments $l_x \sim 1$–2 cm and $l_z \sim 3$–4 mm [3, 7]. At the same time, one has for $\omega_{31} \approx 2\omega_0 \approx 5 \times 10^{10}$ s^{-1} $\lambda \approx 4$ cm $\gg l_z$.

As a result, one can ignore the relatively rapidly varying oscillatory terms and arrive at the set of constitutive equations:

$$\dot{\rho}_{33} = iu(R_{31} - R_{31}^*) + i\psi(R_{32} - R_{32}^*) - \Gamma(\rho_{33} - w_3),$$
$$\dot{\rho}_{11} = iu(R_{31}^* - R_{31}) - \Gamma(\rho_{11} - w_1),$$
$$\dot{R}_{32} = -i(\Delta_{32} - i\gamma_{32})R_{32} - iuR_{21}^* + i\psi(\rho_{33} - \rho_{22}), \tag{7}$$
$$\dot{R}_{31} = -i(\Delta_{31} - i\gamma_{31})R_{31} + iu(\rho_{33} - \rho_{11}) - i\psi R_{21},$$
$$\dot{R}_{21} = -i(\Delta_{21} - i\gamma_{21})R_{21} + iuR_{32}^* - i\psi R_{31},$$

where $\Gamma = 1/T_1$ is the relaxation rate of the diagonal elements of $\hat{\rho}$ (for the sake of simplicity, the approximation of a single longitudinal relaxation rate is used [15]; it is shown below that this approximation is not crucial in our case); γ_{32}, γ_{31}, and γ_{21} are the transverse relaxation rates for the corresponding transitions; $\Delta_{32} = \omega_{320} - \omega_{32}$, $\Delta_{31} = \omega_{310} - \omega_{31}$, and $\Delta_{21} = \omega_{210} - \omega_{31} + \omega_{32}$ are, respectively, the detuning between the field and atomic frequencies; w_α ($\alpha = 1, 2, 3$) are the equilibrium populations of atomic levels; and the diagonal components of $\hat{\rho}$ are related to one another by the expression $\rho_{11} + \rho_{22} + \rho_{33} = 1$.

The induced magnetic dipole transitions $1 \longleftrightarrow 2$ can be ignored if the Rabi frequency of microwave pumping is lower than the detuning between the transitions $2 \longleftrightarrow 3$ and $1 \longleftrightarrow 2$: $\psi \ll |\omega_{320} - \omega_{210}| = (3G_{11}/\hbar)\epsilon_{zz}^{(0)}$. The nonequidistance can be assumed to be appreciable if $|\omega_{320} - \omega_{210}| \sim 0.1\omega_0$. Taking $G_{11} \sim 10^{-14}$ erg for the Ni^{2+} ions in a MgO crystal matrix [1, 3, 6], one obtains that the detuning is $|\omega_{320} - \omega_{210}| \sim 10^{10}$ s^{-1} for the static strain $\epsilon_{zz}^{(0)} \sim 10^{-3}$, which corresponds to its elastic limit; then the microwave pumping at $\psi \ll 10^{10}$ s^{-1} will mainly result in the transitions. Within the framework of this model, the microwave field is a given dynamic parameter; i.e., its decrease due to the resonance absorption at the $2 \longleftrightarrow 3$ transition is ignored. This approach is justified if the pump energy density far exceeds the energy density absorbed by the resonance medium: $\hbar^2\psi^2/(4\pi g^2\mu_B^2) \gg n(w_2 - w_3)\hbar\omega_0$. At $T \sim 1$ K and $2\omega_0 \approx 10^{11}$ s^{-1}, one has, according to the Boltzmann distribution, $w_2 - w_3 \approx 0.2$. Then, one has $\psi \gg 10^7$ s^{-1} for a diluted paramagnet ($n \sim 10^{17}$ cm^{-3} [6]), which corresponds to a microwave intensity $I \gg 10^3$ W/cm^2. On a decrease in temperature to 0.1 K, the populations of the second and third levels become negligible and the microwave pumping is not exhausted for practically any intensity.

In the steady-state regime (for which the time derivatives can be ignored), one obtains from Eqs. (7) in the linear approximation in u

$$R_{31} = -\frac{(\Delta_{21} - i\gamma_{21})u}{(\Delta_{21} - i\gamma_{21})(\Delta_{31} - i\gamma_{31}) - \psi^2} \times \left\{ w_1 - w_3 - \frac{(w_2 - w_3)\psi^2}{\Gamma(\Delta_{32}^2 + \gamma_{32}^2) + 4\gamma_{32}\psi^2} \times \left(2\gamma_{32} + \Gamma\frac{\Delta_{32} - i\gamma_{32}}{\Delta_{21} - i\gamma_{21}} \right) \right\}. \quad (8)$$

We first consider the case where the microwave pumping is absent ($\psi = 0$). Then, from Eq. (8) one has $R_{31} = -u(w_1 - w_3)/(\Delta_{31} - i\gamma_{31})$. Evidently, $\Delta_{31} = \omega_{310} - \omega_{31} + \Delta = \delta\omega + \Delta$, where $\delta\omega$ is the detuning between the hypersound field and the center of inhomogeneously broadened contour of the $1 \longleftrightarrow 3$ transition. Let us further assume that the contour $f(\Delta)$ is Lorentzian: $f(\Delta) = (\gamma/\pi)/(\gamma^2 + \Delta^2)$, where $\gamma^{-1} = T_2^*$ is the dephasing time for the ρ_{31} elements because of the inhomogeneous broadening. As a result and using Eqs. (6) and (5), one arrives for $\gamma \gg \gamma_{31}$ [3, 6] at the dispersion relation

$$k_{31} = \frac{\omega_{31}}{a}\left[1 - 2\eta(w_1 - w_3)\omega_{310}^{(0)}\frac{\delta\omega + i\gamma}{\gamma^2 + \delta\omega^2} \right]^{-1/2},$$

where the dimensionless parameter $\eta = 9G_{11}^2 n/16\hbar\omega_{310}^{(0)}\rho a^2$. For the Ni^{2+} ions in MgO, the above parameters, and [3] $n \sim 10^{17}$ cm^{-3}, $\rho \cong 5$ g/cm^3, $a \approx 10^6$ cm/s, $\omega_{310}^{(0)} \sim 10^{11}$ s^{-1}, and $\gamma \sim 10^8$ s^{-1} [3], one has $\eta \sim 10^{-7}$ and $\omega_{310}^{(0)}/\gamma \sim 10^3$. Hence, the second term in the square brackets of the dispersion relation is much smaller than unity, and one obtains the well-known [16] dependences of the hypersound refractive index $N_0(\delta\omega) = a\mathrm{Re}k_{31}/\omega_{31}$ and absorption coefficient $\kappa_0(\delta\omega) = \mathrm{Im}k_{31}$ on the microwave frequency (Fig. 2)

$$N_0(\delta\omega) = 1 + \eta(w_1 - w_3)\omega_{310}^{(0)}\frac{\delta\omega}{\gamma^2 + \delta\omega^2}, \quad \kappa_0(\delta\omega) = \kappa_0(0)\frac{\gamma^2}{\gamma^2 + \delta\omega^2}, \quad (9)$$

where $\kappa_0(0) = \eta(w_1 - w_3)\omega_{310}^{(0)2}/\gamma a$ is the absorption coefficient at $\delta\omega = 0$. Substituting the above-mentioned parameters for Ni^{2+} in MgO, one finds $\kappa_0(0) \sim 10$ cm^{-1}, which is in good agreement with Shiren's experimental data at $T \approx 1.8$ K [3].

Let now $\psi \neq 0$. As is mentioned above, $\gamma \sim \Delta_{32} \sim \Delta_{21} \gg \gamma_{32}, \gamma_{21}, \gamma_{31}$. In addition, $\gamma_{32} \gg \Gamma$ [3, 6]. We also assume that $\psi \geq \gamma$. Under these conditions, the expression in braces in Eq. (8) is, with a good degree of accu-

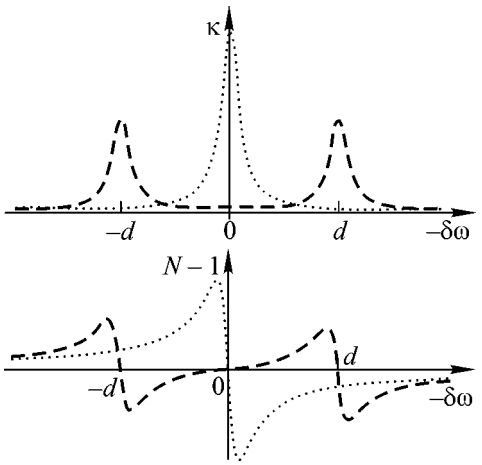

Fig. 2. Resonance profiles of the (top) absorption coefficient and (bottom) refractive index in the (dots) absence and (dashes) presence of resonance electromagnetic pumping.

racy, $w_1 - w_3 - (w_2 - w_3)/2 = (3w_1 - 1)/2$. Let the microwave frequency exactly coincide with the center of the contour of the $2 \longleftrightarrow 3$ transition; i.e., $\omega_{32} = \omega_{320}^{(0)}$. Then $\Delta_{21} = \delta\omega + \Delta$. Taking this and the above estimates into account, one obtains for the hypersound refractive index $N(\delta\omega)$ and absorption coefficient $\kappa(\delta\omega)$ in the presence of pumping

$$\begin{aligned} N(\delta\omega) &= 1 + \eta\frac{3w_1 - 1}{2} \\ &\times \omega_{310}^{(0)}\frac{(\delta\omega^2 + \gamma^2 - \psi^2)\delta\omega}{(\psi^2 + \gamma^2 - \delta\omega^2)^2 + 4\gamma^2\delta\omega^2}, \\ \kappa(\delta\omega) &= \kappa_0(0)\frac{3w_1 - 1}{2(w_1 - w_3)} \\ &\times \gamma^2\frac{\psi^2 + \gamma^2 + \delta\omega^2}{(\psi^2 + \gamma^2 - \delta\omega^2)^2 + 4\gamma^2\delta\omega^2}. \end{aligned} \quad (10)$$

At $T \sim 0.1$ K and $2\omega_0 \sim 10^{11}$ s^{-1}, one has to a good degree of accuracy $w_2 = w_3 = 0$. Then, $(3w_1 - 1)/2 = w_1 - w_3 = 1$. An analysis of Eq. (10) shows that at $\psi < \gamma/\sqrt{3}$ the curves for $N(\delta\omega)$ and $\kappa(\delta\omega)$ are qualitatively the same as in the absence of the microwave field [see Eqs. (9)]. At $\psi > \gamma/\sqrt{3}$, a small dip appears in the center of resonance absorption line, and if $\psi > \gamma$, then both dependences become qualitatively the same as those typical of EIT [8, 11] (Fig. 2). True enough, these curves are smoother because of the inhomogeneous broadening. Two absorption regions appear, which are symmetrically shifted on both sides of the contour center. The shift is $d = \psi$ (Fig. 2). The half-widths of both absorption lines do not differ from the halfwidth of the central line in the absence of pumping and are equal to γ. Their amplitudes are smaller than the amplitude of the central line by a factor of 2. The value of κ in the center of resonance line has a minimum and is equal at $T \sim 0.1$ K to $\kappa(0) = \kappa_0(0)[1 + (\psi/\gamma)^2]^{-1}$, whereas $\kappa(d) \approx \kappa(\psi) = \kappa_0(0)/2$. Taking $\psi \sim 10^9$ s^{-1} (this corresponds to a magnetic component of $\sim 10^2$ Oe and the intensity $I \sim 10^7$ W/cm^2 of the microwave field) and $\gamma \sim 10^8$ s^{-1}, one concludes that a powerful microwave pumping is capable of reducing the hypersound resonance absorption coefficient by two orders of magnitude. For the MgO crystal with impurity Ni^{2+} ions, one finds $\kappa(0) \sim 0.1$ cm^{-1}. Therefore, a paramagnetic sample of size ~1 cm [3] that absorbs the resonance hypersound well at a length on the order of 1 mm becomes practically fully transparent to the hypersound in the presence of a powerful microwave pumping applied to the sample perpendicularly to the hypersound propagation direction. At the same time, whereas the hypersound frequency in the absence of pumping lies outside the absorption contour ($|\delta\omega| \gg \gamma$), in its presence ($\psi = \delta\omega$) the absorption coefficient $\kappa(\delta\omega) = \kappa_0(0)/2 \sim 5$ cm^{-1}, so that the paramagnetic sample is no longer transparent to the hypersound.

From Eq. (10), one finds for the group velocity v_g at $\delta\omega = 0$

$$v_g = a\left[1 + \frac{3w_1 - 1}{2}\eta\left(\frac{\omega_{310}^{(0)}}{\psi}\right)^2\right]^{-1}.$$

Since $\eta \sim 10^{-7}$ and $\omega_{310}^{(0)}/\psi \sim 10^2$, v_g virtually coincides with a. This is probably the strongest qualitative distinction between AIT and EIT, where the ratio v_g/c (c is the speed of light in vacuum) can be as high as 10^{-7}–10^{-8}.

Thus, the microwave field modulates only the hypersound absorption coefficient. The paramagnetic sample acts as a gate (filter) controlled by the electromagnetic pumping.

The role of static strain plays an important role in our case. In the absence of strain, $\omega_{210} = \omega_{320} = \omega_0$ [3]. Then, the electromagnetic field will excite the $1 \longleftrightarrow 2$ transition and will be strongly absorbed.

The physical essence of the effect considered in this work is the same as for the EIT; i.e., it is due to the interference of "dressed" quantum states [10]. Apart from the above-mentioned quantitative distinctions, there is a qualitative distinction caused by the fact that the signal (probe) field and the pump are physically essentially different.

This work was supported by the Russian Foundation for Basic Research, project no. 02-02-17710a.

REFERENCES

1. J. W. Tucker and V. W. Rampton, *Microwave Ultrasonics in Solid State Physics* (North-Holland, Amsterdam, 1972; Mir, Moscow, 1975).
2. V. R. Nagibarov and U. Kh. Kopvillem, Zh. Éksp. Teor. Fiz. **52**, 936 (1967) [Sov. Phys. JETP **25**, 618 (1967)].
3. N. S. Shiren, Phys. Rev. B **2**, 2471 (1970).
4. G. A. Denisenko, Zh. Éksp. Teor. Fiz. **60**, 2269 (1971) [Sov. Phys. JETP **33**, 1220 (1971)].
5. V. V. Samartsev, B. P. Smolyakov, and R. Z. Sharipov, Pis'ma Zh. Éksp. Teor. Fiz. **20**, 644 (1974) [JETP Lett. **20**, 296 (1974)].
6. S. A. Al'tshuler and B. M. Kozyrev, *Electron Paramagnetic Resonance* (Nauka, Moscow, 1972).
7. V. A. Golenishchev-Kutuzov, V. V. Samartsev, N. K. Solovarov, and B. M. Khabibulin, *Magnetic Quantum Acoustics* (Nauka, Moscow, 1977).
8. K. J. Boller, A. Imamoglu, and S. E. Harris, Phys. Rev. Lett. **66**, 2593 (1991).
9. S. E. Harris, Phys. Rev. Lett. **70**, 552 (1993).
10. S. E. Harris, Phys. Today **50** (7), 36 (1997).
11. O. Kocharovskaya, Phys. Rep. **219**, 175 (1992).
12. S. V. Sazonov, Zh. Éksp. Teor. Fiz. **118**, 20 (2000) [JETP **91**, 16 (2000)].
13. S. V. Sazonov, J. Phys.: Condens. Matter **6**, 6295 (1994).
14. S. V. Voronkov and S. V. Sazonov, Zh. Éksp. Teor. Fiz. **120**, 269 (2001).
15. R. H. Pantell and H. E. Puthoff, *Fundamentals of Quantum Electronics* (Wiley, New York, 1969; Mir, Moscow, 1972).
16. A. M. Portis, Phys. Rev. **91**, 1071 (1953).

Translated by V. Sakun

JETP Letters, Vol. 76, No. 3, 2002, pp. 147–150. From Pis'ma v Zhurnal Éksperimental'noĭ i Teoreticheskoĭ Fiziki, Vol. 76, No. 3, 2002, pp. 181–184.

Dynamic Structure Factor in Liquid Cesium on the Basis of Time-Scale Invariance of Relaxation Processes¶

R. M. Yulmetyev*, A. V. Mokshin*, P. Hänggi, and V. Yu. Shurygin*****

** Kazan State Pedagogical University, 420021 Kazan, Russia*
e-mail: rmy@dtp.ksu.ras.ru; mav@dtp.ksu.ras.ru
*** University of Augsburg, D-86135 Augsburg, Germany*
**** Yelabuga State Pedagogical Institute, 423630 Yelabuga, Russia*

Received June 7, 2002

The dynamic structure factor $S(k, \omega)$ in liquid cesium near the melting point at $T = 308$ K is studied by means of Zwanzig–Mori's memory function formalism. The spectra of $S(k, \omega)$ are calculated on the basis of the idea of time-scale invariance of relaxation processes in liquid metals, which appear on the fourth relaxation level. The spectra of $S(k, \omega)$ obtained are compared with the results of an inelastic neutron scattering measurement. For the description of memory effects we use the statistical presentation of the non-Markovity parameter $\varepsilon_1(k, \omega)$. We find that collective excitations at low wave-vector values have a non-Markovian nature. © *2002 MAIK "Nauka/Interperiodica".*

PACS numbers: 61.20.Gy; 61.20.Lc

The study of collective effects in simple liquids has been the subject of intense interest over the last few years in Inelastic Neutron Scattering (INS) experiments [1], Molecular Dynamics (MD) simulations [2, 3], and different theories [4]. According to these methods, liquid alkali metals have distinct collective excitations in a wide range of wave-vector values and also outside the hydrodynamic region. This fact was obtained from a careful analysis of the dynamic structure factor $S(k, \omega)$ spectra. High-frequency peaks are appreciable in $S(k, \omega)$ for low k values (approximately, up to half the position of the first maximum of the static structure factor), and these peaks do not exist in high-k regions. Understanding the microscopic mechanism responsible for the propagation and damping of these excitations is still a challenge in liquid metals, where the dynamics is conditioned by interacting electron gas effects. So, a recent INS experiment on liquid cesium near its melting point was carried out by Bodensteiner *et al.* in Grenoble [5]. The results of their experiment have shown that high-frequency collective excitations exist in this system for wave vector region $k < 1.1$ Å^{-1}. MD simulation performed by Kambayashi and Kahl [2] validated fully the findings of INS in liquid cesium. The analysis of collective excitations that extend beyond the hydrodynamic limit is a great contribution to the development of theoretical models of the liquid state [6].

For a system composed of N particles of mass m, the density fluctuations are given by

$$\rho(k, t) = N^{-1}\sum_{j=1}^{N}\exp[ikr_j(t)],$$

where $r_j(t)$ is the coordinate of the jth particle and k is the wave vector. Then, the main dynamical quantity of interest is the density–density correlation function $F(k, t) = \langle\rho^*(k, 0)\rho(k, t)\rangle/\langle|\rho(k, 0)|^2\rangle$, where $\langle|\rho(k, t)|^2\rangle = S(k)$ is the static structure factor. The angular brackets denote an equilibrium ensemble average at temperature T and density $\rho = N/V$ with V being the volume of the system involved. If $F(k, t)$ is known, the dynamic structure factor follows from

$$S(k, \omega) = [S(k)/\pi]\lim_{\epsilon \to +0}\mathrm{Re}[F(k, i\omega + \epsilon)].$$

According to the memory function (MF) formalism and the projection operator method [7], we can find the time evolution of $F(k, t)$ in the following way:

$$\frac{dF(k, t)}{dt} = -\Omega_1^2\int_0^t d\tau M_1(t-\tau)F(k, \tau). \qquad (1)$$

Here, we introduce the first general relaxation frequency parameter Ω_1^2 and the MF of the first order $M_1(k, t)$. However, by using the same method, we can define the time evolution of the high order *MF* $M_1(k, t)$, $M_2(k, t)$, …. Thus, a set of interconnected relaxation processes corresponds to an arbitrary relaxation pro-

¶ This article was submitted by the authors in English.

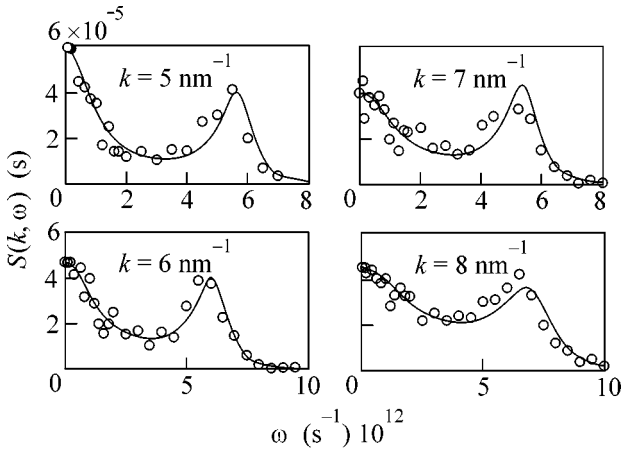

Fig. 1. Theoretical (solid line) and experimental (○) values of the dynamic structure factor for liquid cesium near the melting point.

cess (for example, to a density fluctuations in liquids), which can be easily taken into account by MF formalism.

According to the definition, for ergodic processes the correlation functions $M_0(k, t) = F(k, t)$, $M_1(k, t)$, …, $M_i(k, t)$ have the following properties:

$$\lim_{t \to 0} M_i(k, t) = 1, \quad \lim_{t \to \infty} M_i(k, t) = 0. \tag{2}$$

Thus, the correlation functions $M_i(k, t)$ have characteristic time scales, which can generally be defined at fixed k by the equation

$$\tau_i = \mathrm{Re}[\tilde{M}_i(0)], \quad \tilde{M}_i(s) = \int_0^\infty dt M_i(t) e^{-st}. \tag{3}$$

Here, Re[…] denotes the real part of […].

These time scales T_i characterize the corresponding relaxation processes and can have different numerical values. Nonetheless, on a certain level (for example, on the ith level), the scale invariance of the nearest interconnected relaxation processes can exist. Physically, it implies the existence of the time-scale invariance (TSI) of relaxation processes on the nearest ith and $(i + 1)$-th relaxation levels. Such an approach allows one to receive an approximation of the form $M_{i+1}(k, t) \approx M_i(k, t)$, which is actually the closure of the chain of integro-differential equations similar to 1. As a result, only the first $(i - 1)$ variables are necessary for the full description of the system investigated. In the case of simple liquid metals, by analogy with the hydrodynamics region, we propose that only three variables, namely local density, local momentum density, and local energy density, are sufficient to reproduce its spectral features at the microscopic level. These variables are implicitly present in $F(k, t)$, $M_1(k, t)$, and $M_2(k, t)$. From the above reasoning, one can write the following closure: $M_4(k, t) \approx M_3(k, t)$. By means of the Laplace transformation of the corresponding equations for $M_0(k, t) = F(k, t)$, $M_1(k, t)$, $M_2(k, t)$, we obtain an expression for the dynamic structure factor in which the static structure factor $S(k)$ and general relaxation parameters of the ith orders Ω_i^2 $(i = 1, 2, 3, 4)$ are contained:

$$\begin{aligned} S(k, \omega) = \frac{S(k)}{2\pi} \Omega_1^2 \Omega_2^2 \Omega_3^2 (4\Omega_4^3 - \omega^2)^{1/2} \{ \Omega_1^4 \Omega_3^4 \\ + \omega^2 (\Omega_1^4 \Omega_4^2 - 2\Omega_1^2 \Omega_3^4 - \Omega_1^4 \Omega_3^2 + 2\Omega_1^2 \Omega_2^2 \Omega_4^2 \\ - \Omega_1^2 \Omega_2^2 \Omega_3^2 + \Omega_2^4 \Omega_4^2) + \omega^4 (\Omega_3^4 - 2\Omega_1^2 \Omega_4^2 \\ + 2\Omega_1^2 \Omega_3^2 - 2\Omega_2^2 \Omega_4^2 + \Omega_2^2 \Omega_3^2) + \omega^6 (\Omega_4^2 - \Omega_3^2) \}. \end{aligned} \tag{4}$$

Now, we use the theory proposed above for the evaluation of $S(k, \omega)$ in liquid cesium near its melting point at $T = 308$ K. The quantities needed for the calculation are $S(k)$ and Ω_i^2 $(i = 1, 2, 3, 4)$. The numerical static structure data were obtained by Bodensteiner *et al.* [5], and we use these $S(k)$ data in our calculations. The first two relaxation parameters Ω_1^2 and Ω_2^2 are defined as $\Omega_1^2 = K_B T k^2 / [MS(k)]$, $\Omega_2^2 = \omega_l^2 - \Omega_1^2$, where $\omega_l^2 = 3\Omega_1^2 S(k) + N/MV \int dr g(r) [1 - \cos(kr)] \nabla_z^2 u(r)$. Here, $K_B T$ is the thermal energy, $g(r)$ is the radial distribution function, and $u(r)$ is the pair interparticle interaction potential (the z axis is chosen in the direction of the wave vector k). However, to calculate the second frequency parameter Ω_2^2, we use the known Hubbard–Beeby approximation [8] $\Omega_2^2 = 3\Omega_1^2 S(k) + \omega_E^2 [1 - 3\sin(x)/x - 6\cos(x)/x^2 + 6\sin(x)/x^3] - \Omega_1^2$. Here $x = kR_0$ with $R_0 = 4.8$ Å and the Einstein frequency ω_E^2 is taken to be 4.12 ps^{-1}, which is the value obtained by Bodensteiner [5]. The theoretical formulas for Ω_3^2 and Ω_4^2 cannot be used in calculations for one reason. The final result of these calculations has gross errors. Therefore, these parameters can be defined by comparing theoretical and experimental results. Namely, we found the third and the forth relaxation frequency parameters (Ω_3^2 and Ω_4^2) were found by us from two mutually independent conditions: the behavior of $S(k, \omega)$ in the points of central ($\omega = 0$) and side ($\omega \neq 0$) maximums.

We have calculated $S(k, \omega)$ in the low-k region $k = 0.4 \sim 0.9$ Å^{-1}, where high-frequency peaks were experimentally observed. The results for the representative wave vectors are shown in Fig. 1. It is clear in Fig. 1 that our theory describes adequately the collective density excitations in spectra of $S(k, \omega)$ for liquid cesium. For the investigated wave-vector region, we have achieved a good agreement with the experiment [5]. In Fig. 2, we

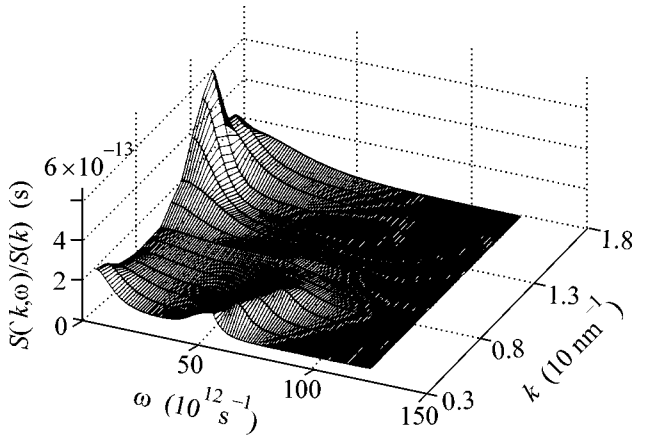

Fig. 2. Dynamic structure factor calculated on the basis theory for liquid cesium at 308 K.

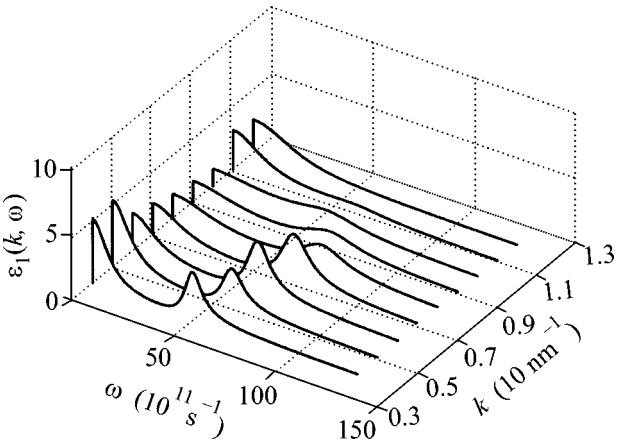

Fig. 3. Frequency dependence of non-Markovity parameter $\varepsilon_1(k, \omega)$ for $4 < k < 12$ nm^{-1}.

report a set of normalized dynamic structure factors, $S(k, \omega)/S(k)$, as calculated from our theory for the wave vector region $0.4 \le k \le 1.8$ Å^{-1}. In this figure, one can see certain changes in the position and altitude of the central and side peaks at different values of the wave vector **k**. As can be seen in Fig. 2, side peaks persist up to $k \sim 1.1$ Å^{-1}, i.e., very close to the position of the first peak in the static structure factor ($k \sim 1.4$ Å^{-1}). This again shows that the liquid supports collective excitations for wavelengths comparable with the mean interparticle spacing, a distinctive characteristic of liquid metals [6].

To understand the nature of the collective excitations below $k = 1$ Å^{-1}, we have studied the behavior of the frequency-dependent non-Markovity parameter $\varepsilon_1(k, \omega)$. This parameter was at first entered [9] on the basis of parameter $\varepsilon_0 = \tau_0/\tau_1$, where the relaxation times τ_0 and τ_1 are calculated by Eq. (3). By this non-Markovity parameter [10], all relaxation processes can be divided into a Markovian scenario, when $\varepsilon_0 \longrightarrow \infty$, a quasi-Markovian scenario at $\varepsilon_0 > 1$, and a non-Markovian scenario at $\varepsilon_0 \sim 1$. The generalized parameter $\varepsilon_1(k, \omega)$ is defined at fixed k by the expression

$$\varepsilon_j(\omega) = \left[\frac{\mu_{j-1}(\omega)}{\mu_j(\omega)}\right]^{1/2}, \qquad \mu_j(\omega) = \{\mathrm{Re}[\int dt M_j e^{i\omega t}]\}^2. \tag{5}$$

Here, $\mu_j(\omega)$ is the power spectra of the ith relaxation level that was introduced. In Fig. 3, we present the results of calculations for the frequency-dependent non-Markovity parameter $\varepsilon_1(k, \omega)$ at several values of wave vectors k. It can be seen in Fig. 3 that the values of $\varepsilon_1(k, \omega)$ show an alternation of maxima and minima. In addition, $\varepsilon_1(k, \omega)$ and $S(k, \omega)$ maxima in the low-k region are located on approximately the same frequencies that are associated with collective excitations in liquid metal. The amplitudes of these peaks quickly fall as k increases. This is due to the amplification of non-Markovity effects. The occurrence of $\varepsilon_1(k, \omega)$ peaks in the region of collective excitations indicates an essential amplification of quasi-Markovity on propagation of ion density fluctuations. High-frequency collective excitations disappear smoothly with increasing k, and simultaneously non-Markovity is further enhanced. Similarly, an increase in $\varepsilon_1(k, \omega = 0)$ means an enhancement of randomness in the thermal motion of particles. Thus, the frequency behavior of the parameter $\varepsilon_1(k, \omega)$ observed consists in a consecutive alternation of quasi-Markovian and non-Markovian relaxation scenarios of behavior. Such an alternation cannot be received within the framework of any other theory.

In this Letter, we have presented the theory, based on Zwanzig–Mori's MF formalism [7], and the idea of TSI, which allows one to describe the dynamic structure spectra in all experimentally investigated regions of the wave vector. The long-range memory and the short time correlations have affected the analysis of non-Markovian properties of the collective dynamics in liquid cesium. In this way, we are going to establish the non-Markovian nature of collective excitations in liquid cesium at low k values.

This work was partially supported by the Russian Foundation for Basic Research (grant no. 02-02-16146). The authors are grateful to Prof. A.G. Novikov and Dr. T. Scopigno for stimulating discussions of scattering data and to Dr. L.O. Svirina for technical assistance.

REFERENCES

1. J. R. D. Copley and M. Rowe, Phys. Rev. A **9**, 1656 (1974); O. Söderstrem, Phys. Rev. A **23**, 785 (1981); O. Söderstrem, J. R. D. Copley, J. B. Suck, *et al.*, J. Phys. F **10**, L151 (1980); U. Dahlborg and K. E. Larsson, Ark.

Fys. **33**, 271 (1966); C. Morkel and W. Gläser, Phys. Rev. A **33**, 3383 (1986); A. Stangl, C. Morkel, U. Balucani, *et al.*, J. Non-Cryst. Solids **205–207**, 402 (1996); A. G. Novikov, V. V. Savostin, A. L. Shimkevich, *et al.*, Physica B (Amsterdam) **228**, 312 (1996).

2. S. Kambayashi and G. Kahl, Phys. Rev. A **46**, 3255 (1992).
3. M. Canales, L. E. González, and Á. Padro, Phys. Rev. E **50**, 3656 (1994); U. Balucani, A. Torcini, and R. Vallauri, Phys. Rev. B **47**, 3011 (1993).
4. F. Yoshida, J. Phys. F **8**, 411 (1978); F. Yoshida and S. Takeno, J. Phys. C **11**, 2895 (1978); R. K. Sharma and K. Tankeshwar, Phys. Rev. E **55**, 564 (1997).
5. T. Bodensteiner, Chr. Morkel, and B. Dorner, Phys. Rev. A **45**, 5709 (1992).
6. U. Balucani and M. Zoppi, *Dynamics of the Liquid State* (Clarendon, Oxford, 1994).
7. R. Zwanzig, Phys. Rev. **124**, 1338 (1961); H. Mori, Prog. Theor. Phys. **33**, 423 (1965).
8. J. Hubbard and J. L. Beeby, J. Phys. C **2**, 556 (1969).
9. R. M. Yulmetyev, P. Hänggi, and F. Gafarov, Phys. Rev. E **62**, 6178 (2000).
10. V. Yu. Shurygin, R. M. Yulmetyev, and V. V. Vorobjev, Phys. Lett. A **148**, 199 (1990).

JETP Letters, Vol. 76, No. 3, 2002, pp. 151–154. From Pis'ma v Zhurnal Éksperimental'noĭ i Teoreticheskoĭ Fiziki, Vol. 76, No. 3, 2002, pp. 185–188.

Cherenkov Radiation and Pair Production by Particles Traversing Laser Beams¶

I. M. Dremin

Lebedev Physical Institute, Russian Academy of Sciences, Moscow, 119991 Russia

Received June 17, 2002

It is shown that Cherenkov radiation can be observed at TESLA in electron collisions with optical laser pulses. The prospects for it to be observed at SLC, LEP, LHC, and RHIC are discussed. The conclusions are compared with results for pair production. © *2002 MAIK "Nauka/Interperiodica".*

PACS numbers: 41.60.Bq; 41.75.Ht

The problem of collisions of very-high-energy charged particles with laser beams is widely discussed now, mostly in connection with e^+e^--pair production (see latest references [1–4]) at SLC and TESLA X-ray laser facilities [5–7] and with some other issues of fundamental physics.

Spontaneous particle creation from vacuum induced by a strong external field was theoretically considered in many papers beginning with [8–10]. However, very powerful high-frequency lasers are needed for this process to be observed. The first observations of this effect were done at SLC [11, 12].

Here, I would like to note that optical lasers can be used for studies of Cherenkov radiation. It is crucial for its observation that the main background process of Compton scattering does not contribute to the kinematical region of Cherenkov radiation. The principal possibility of such a process was first mentioned by V. Ritus in [13]. The results can be, in general, applied to verify our ideas about the properties of the "photon medium" in the region where new physics concepts can become essential and to measure beam energy and laser bunch parameters.

X-ray lasers have been proposed for use in e^+e^--pair production studies because the quantum energies are high enough to reach the threshold energy, which in c.m.s. is equal to $m + 2m_e$, where m_e is the electron mass and m is the mass of the accelerated particle (equal to m_e at SLC, LEP, TESLA, to the proton mass at LHC, and to the nucleus mass at RHIC). At the same time, for studies of Cherenkov radiation, other characteristics of a laser, namely, the ratio F/F_0 of the electric field F to its "critical" value $F_0 = m_e^2/e$ or, equivalently, its peak power density S, are important. They determine the index of refraction n of the "photon medium" in laser bunches. The difference of n from 1 is proportional to the density of photons in a laser pulse, i.e., to S. It is this difference that defines the threshold of Cherenkov radiation and its emission angle and intensity.[1] The parameters F/F_0 and S are higher for optical lasers than for the presently available X-ray lasers. That is why they would be preferred for Cherenkov radiation studies nowadays. Besides, the energy limitations also favor optical lasers for this purpose.

The necessary conditions for Cherenkov radiation to be observed are an excess of the index of refraction n over 1, i.e.,

$$\Delta n = n - 1 > 0, \tag{1}$$

and the real emission angle, given by the formula

$$\cos\theta = 1/\beta n, \tag{2}$$

where $\beta = v/c = \sqrt{1 - m^2/E^2}$ and m and E are the particle mass and energy. For small values of m/E and n, one gets

$$\theta \approx \sqrt{2\Delta n - m^2/E^2} = \sqrt{2\Delta n - \gamma^{-2}}. \tag{3}$$

Hence, the condition for the energy to exceed the threshold for Cherenkov radiation E_{Ct} is written as

$$\gamma m = E \geq E_{Ct} = \frac{m}{\sqrt{2\Delta n}} = \gamma_{Ct} m. \tag{4}$$

It is easily seen that the threshold can become very high for small Δn.

Equation (3) can be rewritten as

$$0 \leq \theta = \sqrt{\gamma^2 - \gamma_{Ct}^2}/\gamma\gamma_{Ct} \leq \frac{1}{\gamma_{Ct}} = \theta_{\max} \quad (\gamma \longrightarrow \infty). \tag{5}$$

¶This article was submitted by the author in English.

[1] An analogous problem was considered in [14] for particles traversing the cosmic microwave background radiation. The density of relic photons is, however, extremely low and, therefore, the index of refraction is so close to 1 that the threshold energy is too high for this effect to be observable.

It is seen that the emission angles of Cherenkov radiation increase from 0 at the threshold to $\theta_{max} = \gamma_{Ct}^{-1}$ for $\gamma \longrightarrow \infty$. However, already at $E = 2E_{Ct}$, this angle is very close to ($\theta(2E_{Ct}) \approx 0.866\theta_{max}$).

The number of Cherenkov photons emitted by a single particle with the electric charge e in the interval of frequencies $d\omega$ from the path length dl is given by the common expression [15]

$$dN_1/d\omega dl = 2\alpha\Delta n, \quad (6)$$

where the fine structure constant $\alpha \approx 1/137$. Thus, all the physical characteristics of the process are determined by the value Δn. The intensity of radiation (6) decreases as the threshold energy (4) increases:

$$\frac{dN_1}{d\omega dl} = \frac{\alpha m^2}{E_{Ct}^2} = \frac{\alpha}{\gamma_{Ct}^2}. \quad (7)$$

The value of Δn is uniquely related to the polarization operator of γ–γ-scattering. For high energy electrons (protons), the laser field can be considered as the constant crossed (or null) field. The refractivity index can be expressed in terms of the photon mass acquired in such a field. It has been calculated in [13, 16], and its graphical representation can be found in [17] (for other approaches see also [18–20]). According to the results of [13, 16], the value of Δn depends on the photon mass μ and its energy ω in the following way:

$$\Delta n = -\mathrm{Re}\mu^2/2\omega^2. \quad (8)$$

The photon mass depends only on the invariant variable

$$\kappa = \frac{2\omega}{m_e}\frac{F}{F_0}. \quad (9)$$

The value of $\mathrm{Re}\mu^2$ is negative[2] in the region about

$$0 \le \kappa \le 15 \quad (10)$$

and has a minimum at $\kappa \approx 5$ with $\mathrm{Re}\mu^2 \approx -0.2\alpha m_e^2$. According to Eq. (8), the refractivity index exceeds 1 in this region, and, consequently, Cherenkov radiation is possible at these values of κ. The perturbation theory is still applicable [13] because $\alpha\kappa^{2/3} \ll 1$.

At a fixed laser intensity, i.e., a fixed ratio F/F_0, the index of refraction does not depend on ω at low energies

$$\Delta n \approx 14\alpha F^2/45\pi F_0^2, \quad (11)$$

because $\mathrm{Re}\mu^2$ is proportional to κ^2 at small κ^2. Thus, the ratio F/F_0 defines there the main features of Cherenkov radiation.

The Cherenkov threshold γ_{Ct} is also completely determined by this ratio as seen from Eqs. (4) and (11). It is the same for electrons and protons. Therefore, the threshold energies E_{Ct} are approximately 2000 times higher for protons than for electrons. Equations (3) and (11) show that, in principle, by measuring the angle θ, one can get the energy of the particle beam and the strength of the laser field or its peak power density.

The magnitude of Δn decreases at higher values of κ and becomes negative at $\kappa > 15$, so that Cherenkov radiation is impossible there.

Even though it can again become positive at extreme energies where the hadronic channels are important, this region is completely inaccessible in collisions with laser beams.

Here, we recall that the energy threshold for the e^+e^--pair production processes in high energy head-on collisions of a particle of mass m with laser quanta is given by

$$E_{th} \approx m_e(m + m_e)/\omega_L. \quad (12)$$

It depends on the energy of laser quanta ω_L and is much lower for X-ray lasers than for optical lasers. It is approximately 1000 times higher for protons than for electrons. In particular, the threshold for $\gamma\gamma$-collisions follows from (12) at $m = 0$.

The condition for Cherenkov radiation threshold to be below the pair production threshold imposes the restriction on the laser quanta energies

$$\omega_L < \sqrt{2\Delta n}\, m_e\left(1 + \frac{m_e}{m}\right) = \gamma_{Ct}^{-1} m_e\left(1 + \frac{m_e}{m}\right). \quad (13)$$

The condition (13) differs for electron and proton beams only by a factor of about 2 in the right-hand side.

For optical and X-ray lasers, according to [2], we assume, respectively, $\omega_L = 1.2$ eV (actually, it varies from 0.12 eV for CO_2-laser to 2.35 eV for Nd:glass laser) and 3.1 keV, the ratios $F/F_0 = 3 \times 10^{-4}$ and 10^{-5} or, equivalently, the peak power densities $S = 3 \times 10^{22}$ W/cm^3 $= 5 \times 10^{16}$ eV^4 and 8×10^{19} W/cm^2 (with a possible goal of 7×10^{29} W/cm^2).

At these parameters, the laser field can be treated as a constant crossed (or null) field because its invariants (see [13])

$$x = \frac{m_e}{\omega_L}\frac{F}{F_0}; \quad \chi = 2\gamma\frac{F}{F_0} \quad (14)$$

are large. For optical lasers with $F/F_0 = 3 \times 10^{-4}$, one gets $x = 125$, and at TESLA energies $\gamma = 10^6$, $\chi = 600$. Thus, the wavelength $1/\omega_L$ is much larger than the formation length m_e/eF.

Electromagnetic processes under these conditions are extremely interesting. New physics concepts may be necessary here because the effective expansion parameter [17, 21, 22] $\alpha\chi^{2/3}$ exceeds 0.5. In particular, this would indicate that the constant field allows the

[2] We consider the value for transverse polarized photons. For other polarizations it differs by a factor less than 2, and this does not change the general conclusions.

interaction with field quanta of arbitrarily low energies. Radiation effects should be reconsidered.

At $F/F_0 = 3 \times 10^{-4}$, Eqs. (9) and (10) impose the upper limit $\omega < 12$ GeV. Only this region of comparatively low energies is accessible for Cherenkov quanta in such strong fields.

Using these characteristics, one also concludes that condition (13) is satisfied for optical lasers with $F/F_0 > 3 \times 10^{-5}$ ($S > 3 \times 10^{21}$ W/cm^2) and is not valid for the presently available X-ray lasers. To satisfy it for X-ray lasers, one must achieve a peak power density as high as 10^{27} W/cm^2, which is, nevertheless, within the proclaimed goals [2].

It follows from Eqs. (6) and (11) that one should deal with the most intense laser fields to get a higher intensity of Cherenkov radiation. Thus, in what follows, we discuss only optical lasers, briefly referring to X-ray lasers for some estimates.

The numerical value of Δn for γ-quanta in the optical laser field with $F/F_0 = 3 \times 10^{-4}$ is given by

$$\Delta n = 0.65 \times 10^{-10}. \quad (15)$$

Therefore, the typical angles and threshold γ-factors for Cherenkov radiation are

$$\theta_{\max} = 1.14 \times 10^{-5}, \quad \gamma_{Ct} = 8.8 \times 10^4. \quad (16)$$

This implies that the energy threshold for Cherenkov radiation is exceeded at LEP2 and TESLA, since it is $E_{Ct}^{(e)} = 45$ GeV and is close to the upper energy of SLC. Only with a further increase in the laser power would it be possible to study this process at SLC.

The pair production threshold for optical lasers is about 430 GeV. Thus, SLC and LEP energies are well below it, while TESLA is just close[3] to the threshold value.

For proton beams, the Cherenkov radiation threshold $E_{Ct}^{(p)} = 83$ TeV is too high even for LHC. If optical lasers with $F/F_0 > 4 \times 10^{-3}$ (the peak power density $S > 5 \times 10^{24}$ W/cm^2) become accessible, one can hope to observe this effect there as well. This energy is much lower than the threshold for pair production at proton accelerators, which is about 400 TeV.

As to the X-ray laser facilities, the threshold for pair production (12) is well below the energies accessible at all the high-energy accelerators.

Now, let us calculate the intensity of Cherenkov radiation for electron beams and compare it with the main background process of Compton scattering.[4] The total number of Cherenkov quanta emitted in the energy interval $d\omega$ by a particle that collides with the laser bunch of the coherent spike length L is

$$\frac{dN_{Ch}}{d\omega} = 2\alpha\Delta n L = 1.1 \times 10^{-5} L \frac{F^2}{F_0^2}. \quad (17)$$

This is the energy distribution at low energies as given by Eqs. (6) and (8). It is almost constant at low energies as demonstrated by Eq. (17) but should decrease towards the cut-off at $\kappa \approx 15$. For a fixed value of the ratio F/F_0, the energies of emitted Cherenkov quanta are proportional to κ and limited according to Eqs. (9) and (10). However, already at $\kappa \approx 4$ the magnitude of Δn and, consequently, the intensity (6) are about twice as low as they are at $\kappa = 0$. Therefore, the effective values of ω, which are important in the distribution, can be approximately estimated according to Eq. (9) as

$$\omega_{\text{eff}} < 2m_e(F_0/F). \quad (18)$$

For the values of the ratio F/F_0 adopted above, one gets $\omega_{\text{eff}}^{(o)} < 3.5$ GeV for optical lasers and $\omega_{\text{eff}}^{(X)} < 100$ GeV for X-ray lasers. One can use Eq. (9) for an estimate of Δn in these energy regions. The threshold and effective energy of Cherenkov quanta decrease, while the emission angle and the intensity of radiation increase with an increase in laser fields F.

The absolute intensity can be evaluated according to Eqs. (6) and (17). For the coherent spike length $L \sim 1$ mm, the number of quanta per 1 GeV is estimated as

$$dN_{Ch}/d\omega \approx 5 \text{ GeV}^{-1}. \quad (19)$$

Thus, the emitted energy within the effective interval should be of the order of 30 GeV per 1 mm.

To proceed with similar estimates for Compton scattering, we consider first its kinematics. This leads to the following relation between the emission angle θ and energy ω of the scattered quantum in the laboratory system:

$$\cos\theta = \left(1 + \frac{\omega_L}{E} - \frac{2\omega_L}{\omega}\right)\left(1 - \frac{\omega_L}{E}\right)^{-1} \approx 1 - \frac{2\omega_L}{\omega}. \quad (20)$$

The precise limits imposed by this relation on the energy of emitted quanta are given by $\omega_L \le \omega \le E$. In the right-hand side of (20), we have taken into account that the particle beam energy is much higher than the photon energies $E \gg \omega > \omega_L$. At angles that are typical for Cherenkov radiation (16), the energy of the backscattered quantum obtained from Eq. (20) is equal to $\omega \approx 37$ GeV, while Cherenkov radiation is much softer ($\omega_{Ch} < 3.5$ GeV) due to the cut-off imposed by the behavior of Δn. Such "soft" photons are emitted at larger angles at Compton scattering. Therefore, there is no overlap of the kinematic regions available for Compton and Cherenkov processes. By separating the relatively soft quanta at the angle (16), one would be able to get rid of the background due to Compton processes. These processes contribute to completely different

[3] However, notice the rather wide spread of available wavelengths for optical lasers mentioned above.

[4] The final results are valid for any charged particles.

energy ranges and, therefore, can be easily disentangled.

The multiphoton processes would lead to even harder quanta in Compton scattering. In other words, they are effective at larger angles $\theta > 2\sqrt{\omega_L/\omega}$. Thus, even at high values of x, the usual Compton effect formulas are needed to estimate its intensity at small angles. Let us also note that these energies are much lower than the threshold for pair production (12) equal to 220 GeV for $L = 1.2$ eV.

The total energy loss due to Compton scattering is much larger than for Cherenkov radiation (19). It can be as large as 16/63 of the initial electron energy [13]. This is determined by the extremely hard backscattered quanta. The use of different lasers inevitably leads to a change in the corresponding values of F/F_0 and S, and, consequently, in the threshold energy E_{Ct}. Therefore, one should treat estimates with caution. The practical feasibility of observing such an effect at high energies should be considered in close relation to the definite conditions of a particular experiment. For example, one cannot use the Nd:glass laser of SLC experiments [11, 12, 23] with $F/F_0 = 2.3 \times 10^{-6}$ at TESLA, because the Cherenkov threshold energy becomes too high. The optimum choice would be a laser with the highest power density (see (17)).

Finally, let us note that, in principle, the heavy ion accelerator RHIC can also be used for pair production studies with X-ray lasers because the threshold energy according to (12) is equal to 165 GeV per nucleon that is available there. The Cherenkov radiation threshold is the same as for proton accelerators if estimated per nucleon. It has been discussed above in connection with LHC and is not reachable at RHIC.

I am grateful to E.L. Feinberg, V.A. Maisheev, A.I. Nikishov, and V.I. Ritus for discussions and comments.

This work was supported by the Russian Foundation for Basic Research, grants no. 00-02-16101 and 02-02-16779.

REFERENCES

1. T. Tajima and G. Mourou, physics/0111091.
2. A. Ringwald, Phys. Lett. B **510**, 107 (2001); hep-ph/0112254.
3. R. Alkofer, M. B. Hecht, C. D. Roberts, *et al.*, Phys. Rev. Lett. **87**, 193902 (2001).
4. V. S. Popov, Pis'ma Zh. Éksp. Teor. Fiz. **74**, 151 (2001) [JETP Lett. **74**, 133 (2001)].
5. J. Arthur *et al.* (LCLS Group), SLAC-R-0521 (1998).
6. R. Brinkman, G. Materlik, J. Rossbach, and A. Wagner, DESY-97-048 (1997).
7. G. Materlik and T. Tschentscher, DESY-TESLA-2001-23; DESY-TESLA-FEL-2001-05 (2001).
8. F. Sauter, Z. Phys. **69**, 742 (1931).
9. W. Heisenberg and H. Euler, Z. Phys. **98**, 714 (1936).
10. J. Schwinger, Phys. Rev. **82**, 664 (1951).
11. C. Bula, K. T. McDonald, E. I. Prebys, *et al.*, Phys. Rev. Lett. **76**, 3116 (1996).
12. D. L. Burke, R. C. Field, G. Horton-Smith, *et al.*, Phys. Rev. Lett. **79**, 1626 (1997).
13. V. I. Ritus, Zh. Éksp. Teor. Fiz. **57**, 2176 (1969) [Sov. Phys. JETP **30**, 1181 (1970)]; Tr. Fiz. Inst. Akad. Nauk SSSR **111**, 113 (1979).
14. I. M. Dremin, Pis'ma Zh. Éksp. Teor. Fiz. **75**, 199 (2002) [JETP Lett. **75**, 167 (2002)].
15. I. E. Tamm and I. M. Frank, Dokl. Akad. Nauk SSSR **14**, 107 (1937); I. E. Tamm, J. Phys. USSR **1**, 439 (1939).
16. N. B. Narozhny, Zh. Éksp. Teor. Fiz. **55**, 714 (1968) [Sov. Phys. JETP **28**, 371 (1969)].
17. V. I. Ritus, Tr. Fiz. Inst. Akad. Nauk SSSR **168**, 144 (1986); **168**, 153 (1986).
18. A. M. Frolov, V. A. Maisheev, and V. L. Mikhailov, Nucl. Instrum. Methods Phys. Res. A **254**, 549 (1987).
19. V. A. Maisheev, Zh. Éksp. Teor. Fiz. **112**, 2016 (1997) [JETP **85**, 1102 (1997)].
20. M. H. Thoma, Europhys. Lett. **52**, 498 (2000).
21. D. A. Morozov and N. B. Narozhny, Zh. Éksp. Teor. Fiz. **72**, 44 (1977) [Sov. Phys. JETP **45**, 23 (1977)].
22. N. B. Narozhny, Phys. Rev. D **20**, 1313 (1979); **21**, 1176 (1980).
23. A. C. Melissinos, in *Proceedings of International Conference "Frontier Tests of QED and Physics of the Vacuum,"* Ed. by E. Zavattini, D. Bakalov, and C. Rizzo (Heron Press, Sofia, 1998), p. 236.

JETP Letters, Vol. 76, No. 3, 2002, pp. 155–159. Translated from Pis'ma v Zhurnal Éksperimental'noĭ i Teoreticheskoĭ Fiziki, Vol. 76, No. 3, 2002, pp. 189–193.

Spin-Injection Mechanism of Magnetization Reversal and Hysteresis of Current in Magnetic Junctions

Yu. V. Gulyaev*, P. E. Zil'berman*, É. M. Épshteĭn*, and R. J. Elliott**

** Institute of Radio-Engineering and Electronics, Russian Academy of Sciences, Fryazino, Moscow region, 141190 Russia*

e-mail: zil@ms.ire.rssi.ru

*** University of Oxford, Department of Physics, Oxford OX1, United Kingdom*

Received June 19, 2002

A novel mechanism is proposed for magnetization reversal by the current of magnetic junctions with two metallic ferromagnetic layers and thin separating nonmagnetic layer. The spin-polarized current flows perpendicularly to the interfaces between the ferromagnetic layers, in one of which the spins are pinned and in the other they are free. No domain structure is formed in the ferromagnetic layers. The current breaks spin equilibrium in the free layer, which manifests itself in the injection or extraction of spins. The nonequilibrium spins interact with the magnetization of the lattice due to the effective field of *s–d* exchange, which is current dependent. At currents exceeding a certain threshold value, this interaction leads to magnetization reversal. Two threshold currents for magnetization reversal have been obtained theoretically, which are reached as the current increases or decreases, respectively. Thus, the phenomenon of current hysteresis is found. The calculated results are in good agreement with experiments on magnetization reversal by current in three-layer junctions of composition Co(I)/Cu/Co(II) prepared in a pillar form. © *2002 MAIK "Nauka/Interperiodica".*

PACS numbers: 75.70.Cn; 75.60.Ej; 75.60.Jk

The possibility of affecting the orientation of magnetization in a thin ferromagnetic film using a spin-polarized current was first suggested and discussed in 1996 [1–3]. In recent years, this problem has attracted increasing interest not only from the theoretical but also from the applied viewpoint. At present, magnetic junctions are applied for reading information with the use of the effect of giant magnetoresistance [3]. The experimental detection of a significant influence of a polarized current on the magnetic state would permit us not only to read but also to write information.

The above effect of current was recently revealed and experimentally studied [4–8] in three-layer magnetic junctions. The polarized current flowed perpendicularly to the layer interfaces. In the literature, various possible mechanisms of current effect have been discussed. It is supposed in [1, 2, 9] that the magnetizations of layers 1 and 2 are noncollinear; in this case, charge carriers, when intersecting the boundary of layer 2, should adjust to the new quantization axis. This adjustment occurs at distances of the order of the quantum wavelength. This results in a torque that acts on the magnetization and depends on the current. At current densities exceeding a certain threshold, this torque leads to magnetization reversal. It is important that the magnetization reversal threshold in this case is determined by dissipative processes in layer 2.

Another mechanism, which is called NEXI (nonequilibrium exchange interaction) by the authors of [10], consists in the establishment of a strong indirect exchange interaction of two ferromagnetic layers upon the passage of a polarized current through these layers. A specific feature of this mechanism is that the charge carriers in layers 1 and 2 should have a common spin wave function. Both mechanisms yield a value of an order of 10^8–10^9 A/cm^2 for the threshold current density.

For "point" junctions with a diameter of the contact of ~4–50 nm [4, 5], a threshold current density close to that predicted theoretically was observed in experiments (10^8–10^9 A/cm^2). However, for metallic pillars of larger diameters (~60–600 nm), the threshold turned out to be much smaller, ~10^7–10^8 A/cm^2 [6, 7]. In addition, the relation of the measured threshold current with the spin-dependent scattering of charge carriers from the boundary of layer 2 and with dissipative processes in layer 2 still remains doubtful [7]. Thus, the question of the possibility of other mechanisms of influence of current on the magnetic state retains its importance.

In this report, we suggest a new, spin-injection mechanism of current effect on the orientation of magnetization in a magnetic junction. We consider a conventional model of a magnetic junction with two ferromagnetic layers, 1 and 2, of which one (layer 1) is pinned and the other (layer 2) is free. The flux of polarized charged carriers from layer 1 into layer 2 injects spins into layer 2, i.e., breaks spin equilibrium and increases the degree of spin polarization in this layer.

The nonequilibrium spins interact with the magnetization of the lattice due to the effective field of *s–d* exchange, which depends on the current. At a sufficiently large current exceeding a certain threshold, the effective field causes the magnetization reversal of layer 2.

The current density through the junction depends on the angle χ between the quantization axes z_1 and z_2 of layers 1 and 2. This dependence is universal, is determined by the rules of transformation of spin wave functions upon rotation of the quantization axis, and has the form [11]

$$j = \frac{j_p + j_a}{2} + \frac{j_p - j_a}{2}\cos\chi, \quad (1)$$

where $j_{p,a}$ are the current densities for the parallel ($\chi = 0$) and antiparallel ($\chi = \pi$) orientations of the magnetizations. An external field can change the angle χ, which leads to the effect of giant magnetoresistance; its measure is the ratio $\rho \equiv (j_p - j_a)/j_p > 0$.

The spin injection in layer 2 can conveniently be characterized by the function

$$P_2(y) = \frac{n_\uparrow(y) - n_\downarrow(y)}{n}, \quad (2)$$

where y is the coordinate along the current, $n_{\uparrow,\downarrow}(y)$ are the densities of charge carriers with opposite spins, and $n = n_\uparrow(y) + n_\downarrow(y)$ is the total carrier density independent of the coordinate y in the case of metal because of the condition of quasi-neutrality. By its meaning, $P_2(y)$ is the degree of spin polarization in layer 2.

We assume that in layer 1 the spins are completely pinned. Therefore, the degree of spin polarization in this layer is equal to the equilibrium degree P_1 and is independent of coordinates. The flux of spins in layer 1 is uniform in space and is directed along the current, i.e., along the y axis. Upon the passage into layer 2, only the projection of the spin onto the quantization axis z_2 remains unchanged [1, 2]. The flux of this projection at the interface $y = 0$ is $J_1 = (\hbar/2e)jP_1\cos\chi$ and continuously passes into the flux of spins in layer 2

$$J_2(y) = \frac{\hbar}{2e}[j_\uparrow(y) - j_\downarrow(y)], \quad (3)$$

where the partial densities of currents of charge carriers with opposite spins are

$$j_{\uparrow,\downarrow}(y) = -eD\frac{\partial n_{\uparrow,\downarrow}(y)}{\partial y} + en_{\uparrow,\downarrow}(y)v. \quad (4)$$

For simplicity, the drift velocity v and the diffusion coefficient D in (4) are assumed to be independent of spin. In essence, it is the existence of a spin flux at the interface between the layers that is the cause of the violation of spin equilibrium in layer 2, i.e., the cause of spin injection or extraction.

The partial current densities satisfy the continuity equations

$$\frac{1}{e}\frac{\partial j_{\uparrow,\downarrow}(y)}{\partial y} = -\frac{n_{\uparrow,\downarrow}(y) - n^e_{\uparrow,\downarrow}}{\tau_s}, \quad (5)$$

in which $n^e_{\uparrow,\downarrow}$ are the equilibrium carrier densities and τ_s is the spin equilibration time. Equations (2), (4), and (5) permit us to obtain the equation for the sought function $P_2(y)$, which has the form

$$\frac{\partial^2 P_2(y)}{\partial y^2} - \frac{v}{D}\frac{\partial P_2(y)}{\partial y} - \frac{[P_2(y) - P_2]}{D\tau_s} = 0, \quad (6)$$

where P_2 denotes the equilibrium value of $P_2(y)$. We seek the solution to Eq. (6) that satisfies the following boundary conditions: (1) the condition for the continuity of the flux of spins at $y = 0$, namely, $J_1 = J_2(y \longrightarrow +0)$, and (2) the condition for the restoration of spin equilibrium through the thickness of layer 2 equal to L_y, i.e., the condition $L_y > l_s$, where l_s is the spin relaxation length. The condition $L_y > l_s$ is in principle unimportant and is imposed here for simplicity. With decreasing L_y, all further formulas stop being dependent on the thickness of layer 2, and for estimation we can merely assume $L_y = l_s$ in them.

The explicit expression for the relaxation length l_s is determined by the relationship between the contribution of diffusion and drift to the current (4). The most important contribution comes from currents that are not too high, when

$$|j| \ll j_D \equiv 2en\sqrt{D/\tau_s}, \quad (7)$$

at which diffusion is dominating. Indeed, $D \sim v_F^2\tau_p$, where the Fermi velocity is $v_F \sim 10^8$ cm/s, the time of relaxation of the momentum is $\tau_p \sim 3 \times 10^{-15}$ s, $\tau_s \sim 10^{-13}$ s, and $n \sim 10^{22}$–10^{23} cm^{-3}. Then, we obtain $j_D \sim 5.4 \times 10^{10}$ to 5.4×10^{11} A/cm^2. Later in this paper, we will consider much smaller currents, so that condition (7) is always well fulfilled. In this case, the length l_s is determined only by diffusion and can be estimated as $l_s = \sqrt{D\tau_s} \sim 17$ nm.

Finding a solution to Eq. (6) and averaging it over the thickness of layer 2, we obtain

$$\bar{P}_2 \equiv \frac{1}{L_y}\int_0^{L_y} P_2(y)dy = P_2 + (P_1\cos\chi - P_2)(j/j_c), \quad (8)$$

where $j_c = enL_y/\tau_s$.

The injection term proportional to current in (8) is small, since $j_c = (L_y/2l_s)j_D \gg |j|$. Therefore, the contribution that is proportional to current to the average magnetization of layer 2, which is equal to $\bar{M}_2 \equiv M_2 +$

$\mu_B n \bar{P}_2$ where μ_B is the Bohr magneton, should also be small. The energy of magnetic anisotropy and the Zeeman energy in an applied magnetic field H are determined by the magnetization $\bar{M}_2$. Therefore, the contribution of the current and spin injection to these energies should also be negligible. The situation with the energy of the *s–d* exchange interaction is different. The average density of this energy (integral of the energy density over the volume of the layer referred to volume) can be represented in the form

$$E_{s-d} = -\alpha M_2 \mu_B n \bar{P}_2. \quad (9)$$

Energy (9) is proportional to the product of the magnetizations of the lattice and free carriers; the dimensionless coefficient α that characterizes the efficiency of exchange is estimated as $\alpha \sim Aa^3/\mu_B^2$. A typical value of the parameter A is 0.1–10 eV [12]. The parameter a is of the order of the lattice parameter. We take a value $a^3 \sim 10^{-23}$ cm^{-3} for the estimation. Then, we obtain $\alpha \sim 1.8 \times (10^4–10^6) \gg 1$. It is precisely due to the large value of the coefficient α that the spin injection caused by the polarized current substantially affects the exchange energy and, through it, the magnetic state of layer 2.

The substitution of Eqs. (1) and (8) into Eq. (9) yields the angular dependence of the energy density of the *s–d* exchange in the form

$$E_{s-d} = -A_{s-d} - B_{s-d}\cos\chi - C_{s-d}\cos\chi, \quad (10)$$

where

$$A_{s-d} = \alpha\mu_B n M_2 P_2\left[1 - \frac{\tau_s}{2enL_y}(j_p + j_a)\right], \quad (11)$$

$$B_{s-d} = \frac{\alpha\mu_B M_2 \tau_s}{2eL_y}[P_1(j_p + j_a) - P_2(j_p - j_a)], \quad (12)$$

$$C_{s-d} = \frac{\alpha\mu_B M_2 \tau_s P_1}{2eL_y}(j_p - j_a). \quad (13)$$

Let the easy axis lie in the plane of layer 2 and make an angle β with the quantization axis z_1 of layer 1. Then, the anisotropy-energy density in layer 2 is

$$E_A = -K\cos^2(\chi - \beta), \quad (14)$$

where K is the anisotropy constant.

If the external magnetic field is applied in the same plane at an angle α to the axis z_1, then the Zeeman-energy density in layer 2 is

$$E_H = -\tilde{M}_2 H\cos(\chi - \alpha), \quad (15)$$

where $\tilde{M}_2 = M_2 + \mu_B n P_2$ is the equilibrium magnetization of layer 2 produced by localized spins and free charge carriers. The total magnetic energy of the layer is equal in this case to the sum

$$E_{tot} = E_{s-d} + E_A + E_H \quad (16)$$

and can be considered as a function of the angle χ at given a α and β.

It can be seen from a comparison of (10) with (14) and (15) that the *s–d* exchange energy is equivalent to the appearance of an additional magnetic field $H' = B_{s-d}/\tilde{M}_2$, which is parallel to the z_2 axis, and that of an additional anisotropy with an anisotropy constant $K' = C_{s-d}$ and an anisotropy axis parallel to the z_2 axis. It is known that changes in the field or in the anisotropy constants can lead to reorientation phase transitions in the film. We show below that the polarized current, changing the field H' and the constant K', also leads under certain conditions to the magnetization reversal of layer 2.

Consider the simplest (and, apparently, the most important [6, 7]) case where $\alpha = \pi$ and $\beta = 0$. We completely neglect the dissipative processes in the magnetic subsystem of layer 2. Then, this subsystem under stationary conditions can be in a state of partial equilibrium in spite of the presence of a dc constant current. The equilibrium angle χ is determined from the conditions of the minimum of energy (16)

$$\frac{\partial E_{tot}(\chi)}{\partial\chi} = 0, \quad \frac{\partial^2 E_{tot}(\chi)}{\partial\chi^2} > 0. \quad (17)$$

After calculating the derivatives in (17) with Eqs. (10) and (14)–(16) taking into account, we find that the magnetic state is determined by the current-dependent parameter

$$\xi \equiv -\frac{B_{s-d} - \tilde{M}_2 H}{2(C_{s-d} + K)}. \quad (18)$$

At $|\chi| < 1$, two equilibrium angles exist, $\chi = 0$ and $\chi = \pi$; at $\chi > 1$, there is only one equilibrium angle, $\chi = \pi$; and at $\xi < -1$, there also is only one angle, $\chi = 0$.

The establishment in the junction of this or that value of the angle χ depends on the history of the magnetization process. Let first the current be $j = 0$ and a sufficiently large (in absolute magnitude) field be present ($|H| > 2K/\tilde{M}_2$). According to (18), such a situation corresponds to $\xi > 1$, and the angle $\chi = \pi$. Let now the current increase in the positive direction, i.e., $j/j_c > 0$. Then, the charge carriers are injected into layer 2 and increase, in accordance with (8), the degree of spin polarization in this layer. According to (12), the coefficient B_{s-d} increases, whereas the coefficient $C_{s-d} \sim (j_p - j_a)$ is relatively small. In this case, the parameter ξ decreases and falls into the interval $|\xi| < 1$. In this range, the value of the angle $\chi = \pi$ is equilibrium and, therefore, remains unaltered. This situation is retained until we, with a further increase in the current, fall into another interval, $\xi < -1$. At the boundary of this interval, the equilibrium angle should change abruptly to the value $\chi = 0$. Thereby, at this boundary, a discontinuous reorientation of the magnetization occurs (magnetization reversal). The threshold current density for such a process, $j_{a \to p}$, can be found from the condition $\xi = -1$

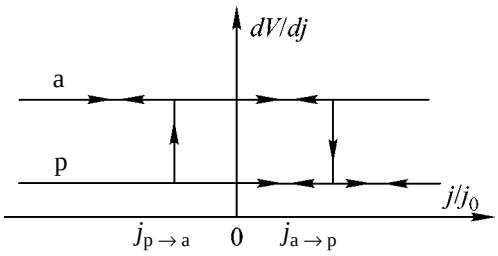

Current dependence of the differential resistance dV/dj: (a) upon the antiparallel and (p) parallel orientations of the magnetizations in layers 1 and 2. Arrows show the possible directions of current changes.

and, with Eqs. (12) and (13) taking into account, is equal to

$$j_{a\to p} = j_0(1-\rho)\frac{h+h_k}{2P_1-\rho(3P_1+P_2)}, \qquad (19)$$

where

$$h = \frac{H}{4\pi\tilde{M}_2}, \quad h_k = \frac{K}{2\pi\tilde{M}_2^2}, \quad j_0 = j_c\frac{8\pi\tilde{M}_2^2}{\alpha\mu_B nM_2}.$$

As the current changes to the opposite direction, we again fall into the interval $|\xi| < 1$, but now we have $\chi = 0$. Since this angle is the equilibrium angle in this interval, it will be conserved. As the current decreases further, the value $j = 0$ is reached and then the current changes its sign. According to (8), this means that now the extraction of spins occurs and a decrease in the degree of spin polarization in layer 2. This continues until we pass into the region $\xi > 1$. At the boundary, the equilibrium angle returns abruptly to the initial value $\chi = \pi$. In other words, a second magnetization reversal to the initial orientation occurs at this boundary. The threshold current density $j_{p\to a}$ for this process is found from the condition $|\xi| = 1$, which yields

$$j_{p\to a} = j_0\frac{h-h_k}{2P_1+\rho(P_1-P_2)}. \qquad (20)$$

Comparing formulas (19) and (20) with one another, we see that the threshold currents do not coincide. This or that threshold current can be obtained depending on in which direction a change in the current occurs. In other words, we obtained a current hysteresis. Note that such a situation was observed experimentally in [6–8] upon the investigation of pillar magnetic junctions of composition Co(I)/Cu/Co(II). In this connection, we perform a more detailed comparison of our calculations with the results of the above works.

It is convenient to represent the calculated dependence of the differential resistance dV/dj on the current density j, where by V we mean the voltage of the current source. The result, naturally, will depend on the mechanism of conductivity in the junction (ohmic conductivity, ballistic transport, effects of heating, etc.). For simplicity, we will assume that the conductivity is ohmic. Then, $dV/dj = R + r(\chi)$, where R is the internal resistance of the source, and $r(\chi)$ is the resistance of the junction depending on the angle χ. These dependences for two values of the angle χ ($\chi = \pi$ and $\chi = 0$) are shown in the figure. Arrows indicate the character and the direction of the change in the resistance depending on the current. Jumps of resistance related to magnetization reversal are seen. Qualitatively, this dependence completely corresponds to experimental data [6–8].

For quantitative estimation, we will use the abovecited numerical values of some parameters and additionally take the following parameters for Co films [13]: $M_2 \sim 0.1$ T, $K \sim 0.4$ J/cm^3, $n \sim 10^{22}$ cm^{-3}, $\alpha \sim 1.8\times 10^5$, $P_1 = P_2 = 0.38$, and $L_y = l_s = 17$ nm. The earlier-introduced parameter of the magnetoresistance ρ can be written as $\rho = (r(\pi) - r(0))/(R + r(\pi))$. Since in [5–7] the relation $R \gg r(\chi) \geq r(0)$ was fulfilled, the parameter ρ was very small. Therefore, upon the estimation of threshold currents by formulas (19) and (20), we assume $\rho = 0$. Then, we obtain (at $h = 0$) $j_{a\to p} = -j_{a\to p} \sim 3.4\times 10^7$ A/cm^2, which approximately corresponds to the experimental estimate of the threshold currents. We emphasize that, as in experiments, the threshold currents have different signs at $h = 0$ and coincide in absolute magnitude. It is seen from our calculations that the magnitude of these currents is mainly determined by the magnetic anisotropy rather than by the dissipative processes in layer 2. In complete accordance with experiments, the threshold currents are shifted in the positive direction upon the application of the magnetic field h, and the symmetry in the location of the two thresholds with respect to the point $j = 0$ is violated (see figure). It is interesting that the theory predicts the disappearance of one of the thresholds, namely, $j_{a\to p} = 0$, at $h = h_k$. At given values of the parameters and anisotropy constant K, this should correspond to a field $H \approx 0.8$ T.

In conclusion, we consider our supposition on the absence of a domain structure in layer 2. The character of the domain structure in such cases and the effect of the polarized current on this structure have been discussed in our previous papers [14, 15]. According to [14], no domains should arise in very thin films, when $L_y \leq \delta$, where δ is the width of a domain wall (typically, $\delta \sim 5$ nm [16]). It is precisely this relation that was fulfilled in experiments [6–8], where $L_y \approx 1.5$–10 nm. Note that, according to [15], no current hysteresis arises in the presence of a domain structure, and the switching from the current j_a to the current j_p and vice versa occurs gradually rather than abruptly.

ACKNOWLEDGMENTS

This work was supported in part by the ISTC (grant no. 1522) and by the Russian Foundation for Basic Research (project no. 00-02-16384).

REFERENCES

1. J. C. Slonczewski, J. Magn. Magn. Mater. **159**, L1 (1996).
2. L. Berger, Phys. Rev. B **54**, 9353 (1996).
3. N. F. Schwabe, R. J. Elliott, and S. Wingreen, Phys. Rev. B **54**, 12953 (1996).
4. M. Tsoi, A. G. M. Jansen, J. Bass, *et al.*, Phys. Rev. Lett **80**, 4281 (1998).
5. E. B. Myers, D. C. Ralf, J. A. Katine, *et al.*, Science **285**, 867 (1999).
6. J. A. Katine, F. J. Albert, R. A. Buhrman, *et al.*, Phys. Rev. Lett. **84**, 3149 (2000).
7. J. Grollier, V. Cros, A. Hamzic, *et al.*, Appl. Phys. Lett. **78**, 3663 (2001).
8. J.-E. Wegrowe, A. Fabian, Ph. Guittienne, *et al.*, Appl. Phys. Lett. **80**, 3775 (2002).
9. L. Berger, J. Appl. Phys. **89**, 5521 (2001).
10. C. Heide and R. J. Elliott, Europhys. Lett. **50**, 271 (2000).
11. M. Julliere, Phys. Lett. A **54**, 225 (1975).
12. É. L. Nagaev, *Physics of Magnetic Semiconductors* (Nauka, Moscow, 1979).
13. S. Chikasumi, *Physics of Ferromagnetism. Magnetic Characteristics and Engineering Applications* (Syokabo, Tokyo, 1984; Mir, Moscow, 1987), in Japanese.
14. Yu. V. Gulyaev, P. E. Zil'berman, R. J. Elliott, and É. M. Épshteĭn, Fiz. Tverd. Tela (St. Petersburg) **44**, 1064 (2002) [Phys. Solid State **44**, 1111 (2002)].
15. Yu. V. Gulyaev, P. E. Zil'berman, R. J. Elliott, and É. M. Épshteĭn, Zh. Tekh. Fiz. **72** (7), 79 (2002) [Tech. Phys. **47**, 873 (2002)].
16. L. D. Landau and E. M. Lifshits, *Collection of Works of L. D. Landau* (Nauka, Moscow, 1969), Vol. 1, p. 128.

Translated by S. Gorin

JETP Letters, Vol. 76, No. 3, 2002, pp. 160–164. Translated from Pis'ma v Zhurnal Éksperimental'noĭ i Teoreticheskoĭ Fiziki, Vol. 76, No. 3, 2002, pp. 194–198.

Magnetic Properties of Two-Dimensional SNS-Type Josephson Junction Arrays

S. M. Ishikaev*, É. V. Matizen*, V. V. Ryazanov, and V. A. Oboznov****

** Institute of Inorganic Chemistry, Siberian Division, Russian Academy of Sciences, Novosibirsk, 630090 Russia*
e-mail: salavat@casper.che.nsk.su
*** Institute of Solid State Physics, Chernogolovka, Moscow region, 142432 Russia*
Received June 25, 2002

The field dependence of the magnetic moment of square (100×100) SNS-type Josephson junction arrays was studied by a SQUID magnetometer. A considerable difference in the behavior of this dependence was revealed for the cases of the entry of magnetic flux into the array and its exit from it. The branches of the curve obtained with increasing field strength had the form of regular periodic dependences with peaks corresponding to integer and half-integer numbers of flux quanta per cell. The curves obtained with decreasing field strength had no noticeable features and, in particular, no periodic structure. Magnetic flux avalanches were not observed in the SNS-type arrays, although the critical parameter of the system was sufficiently great ($LI_C/\Phi_0 \gg 1$) to satisfy the necessary condition of the self-organized criticality. The quasi-hydrodynamic flux motion in the array was explained by the considerable viscosity characterizing the vortex motion through the Josephson junctions.

PACS numbers: 75.70.Cn; 74.80.Fp; 74.50.+r; 74.25.Ha

The dynamics of magnetic vortices in regular arrays of Josephson junctions attracted the attention of researchers years ago [1, 2] and has been intensively studied in recent years with a view to obtaining a narrow-band coherent submillimeter radiation from a Josephson junction array (JJA) with a large number of junctions [3]. Despite the fact that the vortex dynamics in JJAs is the subject of numerous theoretical publications, e.g., [4, 5], direct experimental studies of the magnetic properties of JJAs are only represented by our publication [6], which reports on the observation of avalanches of tens or hundreds of flux quanta in Nb–NbO_x–Pb JJAs and the realization of a self-organized criticality [7]. The presence of the latter in chaotic JJAs was predicted in 1994 [8]. It should be noted that the possibility of the appearance of such avalanches demonstrating the realization of the self-organized criticality in the magnetization of a regular JJA was predicted by none of the theoretical publications (see, e.g., [4, 5]). After the aforementioned publication of our results, Ginzburg and Savitskaya showed that, in ideal JJAs, the self-organized critically is impossible, and the avalanches observed in our experiment could be caused by a slight violation of the array periodicity. The scatter in the array cell dimensions that is sufficient to cause such an effect is about 5% [9], which is within the technological scatter of the parameters of our JJAs.

The purpose of the study described below was the observation of the magnetic flux motion in the JJAs with SNS junctions and, specifically, the detection of the manifestations of the self-organized criticality, such as the formation of avalanches, as in the SIS-type JJAs [6]. Taking into account that, in SNS junctions, one can obtain large critical currents (and large values of the critical parameter), we expected to obtain large avalanche amplitudes with these devices. However, the behavior of the magnetic flux in SNS-type arrays proved to be noticeably different from that in arrays with SIS junctions.

In our experiment, we studied square JJAs fabricated using the same masks as in the previous study, but in this case the arrays consisted of Nb–$Cu_{0.95}Al_{0.05}$–Nb junctions of the SNS type. Each junction had an area of 7 μm^2, a normal layer thickness of 200 nm, a normal resistance $R_n \sim 10^{-3}\ \Omega$, an inductance per cell $L \sim 2 \times 10^{-12}$ H, and a critical current $I_C \sim 1.5$ mA at $T = 4.2$ K (the corresponding critical parameter was $LI_C/\Phi_0 \sim 9.3 \gg 1$, where Φ_0 is a magnetic flux quantum). The array consisted of 100×100 cells whose size was $a^2 = 20 \times 20\ \mu m^2$ (a piece of the array is schematically represented in Fig. 1).

The measurements were performed by a SQUID magnetometer with a sensitivity of 10^{-13} A m^2. The magnetometer was designed in our laboratory, and its characteristics are briefly described in our previous publication [6] and also in [10].

The results of measurements are presented in Figs. 2 and 3 displaying the hysteresis loops of the dependence $M(H)$ for a number of temperatures. Owing to the adjustment of the astaticism of the receiving coils–solenoid system, the curves were recorded with almost

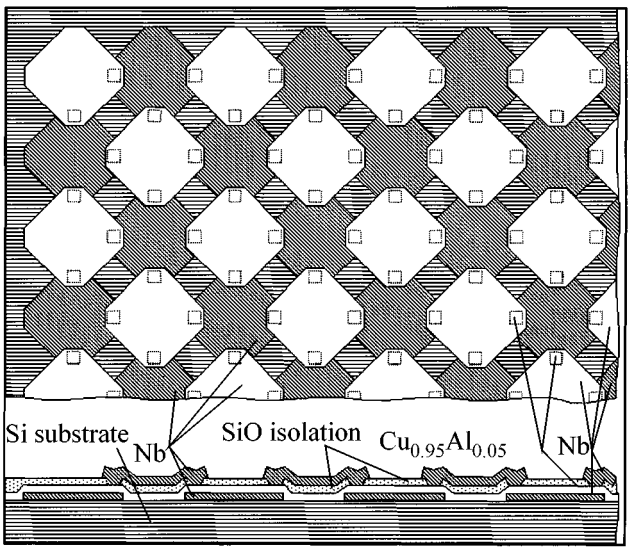

Fig. 1. Geometry of a Nb–$Cu_{0.95}Al_{0.05}$–Nb Josephson Junction array.

complete compensation of the considerable contribution made by the superconducting films (banks) of the Josephson structure under study in the SQUID magnetometer. This contribution was proportional to the external field, and, at a temperature of 7 K in a field of 300 mOe, it exceeded the signal from the JJA by more than an order of magnitude.

The curves $M(H)$ reflect the specific critical state arising in a regular Josephson structure. At temperatures below 8 K, one can see pronounced regular peaks with a temperature-independent period of approximately 60 mOe in magnetic field. In view of the fact that the real field in the array region is reduced because of the partial displacement of the field of the solenoid by the superconducting film structure, this value corresponds to the flux quantum per array cell $\Delta H = \Phi_0/a^2 \sim$ 52 mOe. The periodic peaks of the magnetic moment mean a sharp increase in the critical current of the fluxon pinning (the depinning current) at integer frustrations f, when all cells contain equal integer numbers of flux quanta and their distribution throughout the array is most regular and stable. Exactly in the middle between any two large peaks, one can notice small peaks that correspond to changes of the magnetic flux by a half-quantum per cell. Presumably, this situation also corresponds to the relatively stable distribution of the added flux quanta over the JJA in a checkered order [11, 12]. At temperatures from 6 to 7.1 K in the field interval ±60 mOe, one also can see features corresponding to flux changes by one third of the flux quantum per cell. In the region where periodic peaks are observed, their shape at $\lambda \gg a$ agrees well with the calculations [4].

The most intriguing fact seems to be as follows: the sharp regular peaks in the hysteresis loops are observed

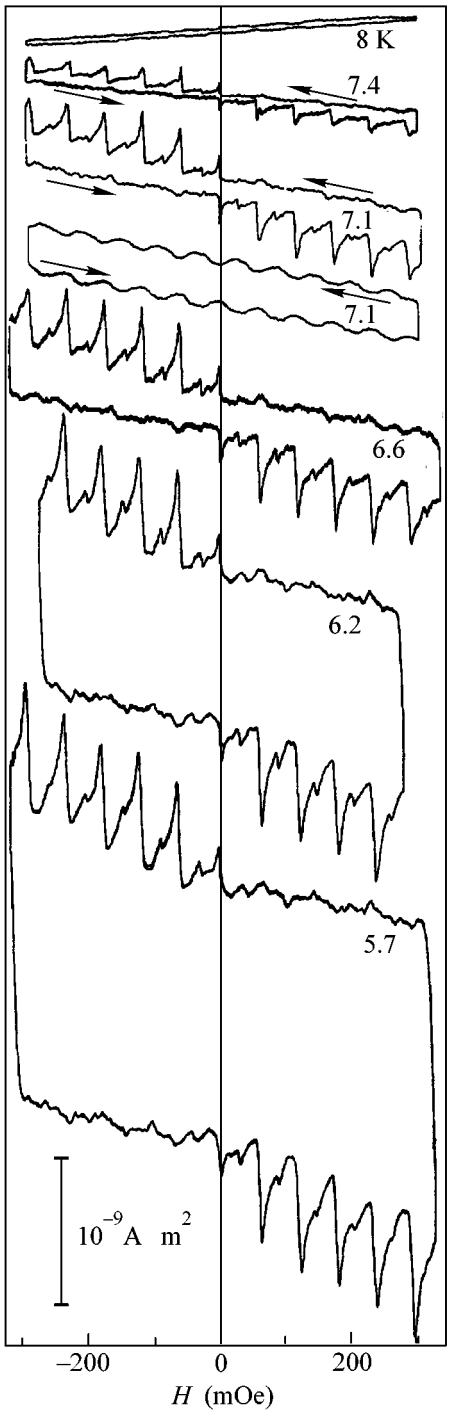

Fig. 2. Magnetization curves of a Josephson junction array for temperatures between 5.7 and 8 K.

only when the field strength increases while, when the field strength decreases, they are practically undetectable and reappear when the field crosses the zero level. Since the peaks in the magnetization curve reflect the ordered filling of the JJA by magnetic flux, their absence in the descending branch presumably indicates the absence of ordering in the flux distribution over the

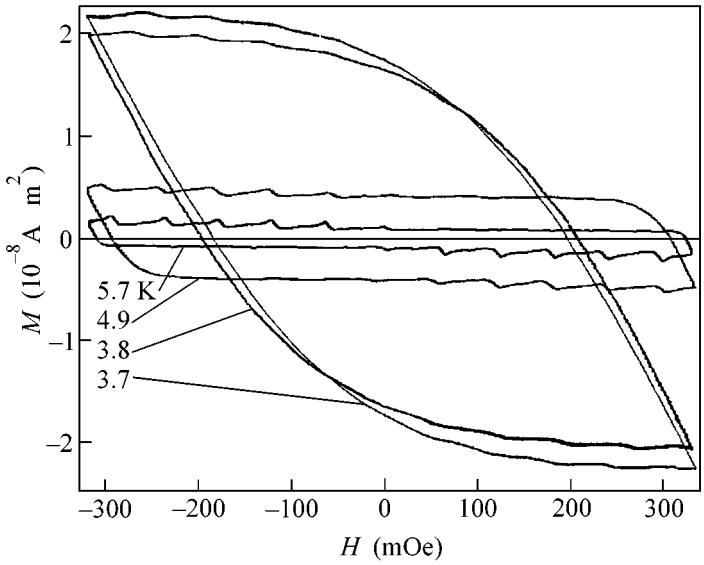

Fig. 3. Magnetization curves of a Josephson junction array for temperatures between 3.7 and 5.7 K.

Josephson structure in the course of the field decrease. Thus, the entry of fluxons into the array is accompanied by the formation of ordered structures in their distribution, whereas the exit from the array occurs in a random irregular way. It should be noted that asymmetry of magnetization was also observed in SIS-type JJAs [6], but in that case, it was weakly pronounced and therefore was ignored in the cited paper. Hence, the asymmetry can be accepted as a general property of the collective motion of Josephson vortices in JJAs, and this property is somehow related to the geometry of the system but independent of the type of junctions.

Possibly, the asymmetry of the hysteresis loops is to some extent caused by the boundary potential barrier, which hinders the penetration of fluxons into the array and, thus, leads to a difference in the type of their distribution in the JJA at their entry and exit. The characteristic features of magnetic dynamics may also be determined by the fact that the profile of the potential energy of pinning in the cells near the boundary of the Josephson array is asymmetric due to the edge effects. In [13], it was shown that the asymmetry of the pinning potential can lead to an anisotropy of the pinning force, i.e., a kind of "diode effect," when the force required for setting the vortices in motion in one direction is smaller than the force required for their motion in the opposite direction. It is natural to expect that the asymmetric profile of the pinning potential varies along the boundary and that, near the corners of the array, it is noticeably different from the profile at the boundary away from the corners. This may lead to a situation where the entry and exit of the flux occur through different regions of the boundary, and hence these are accompanied by different types of flux distribution in the array. We assume that another important factor was that the dimensions of the Josephson junctions in our structure (~3 μm) were fundamentally comparable with the dimensions of the JJA cells (20 μm). In the theoretical publications available to us, the modeling of the vortex dynamics in JJAs was performed by assuming the junction dimensions to be negligibly small, and this seems to be the main reason why the asymmetric behavior was not predicted by the theory.

In Fig. 2, one can notice two fundamentally different magnetization curves obtained for a JJA at a temperature of 7.1 K. The lower of these two curves exhibits no sharp peaks and no asymmetry observed in all the other hysteresis loops. The curve was obtained by heating the JJA above the superconducting transition temperature and then cooling it in a magnetic field of ≈180 mOe. Such a procedure results in the freezing of Abrikosov vortices in the niobium films forming the banks of the Josephson junctions. Since the pinning occurs in this case at randomly distributed defects, a certain disorder is introduced in the magnetic system. In the magnetic field range studied in the experiment, the Abrikosov vortices do not move from their positions because of the large pinning force in the superconducting films, but they noticeably affect the flux motion through the Josephson array. This effect proves to be greater than the effects of other factors, and therefore the curve under consideration exhibits no asymmetry and no sharp peaks at integer frustrations. All other curves were obtained with the Josephson arrays cooled in magnetic fields below 1 mOe, which guaranteed the absence of Abrikosov vortices.

One can distinguish two temperature regions within which the curves $M(H)$ behave in different ways. In the first region corresponding to higher temperatures (Fig. 2), the depth of the field penetration into the array, $\lambda = \Phi_0/2\pi\mu_0 I_C$, considerably exceeds the array period a. Every flux quantum (fluxon) with the diameter ~λ is

distributed over several cells, and their intrinsic fields of currents are small (the weak pinning region). In this limit, the magnetic flux is uniformly distributed over the array. Within this temperature region, sharp peaks of $M(H)$ are observed in the ascending branches of the hysteresis loops, every peak corresponding to a state with an integer number of flux quanta per cell. At lower temperatures, when λ is much smaller than a (the strong pinning region), each cell always contains an integer number of flux quanta, and their behavior can be described by the discrete dynamics. In this case, the intrinsic fields of the screening currents flowing in the JJA are large, which results in a nonuniform distribution of fluxons over the array and manifests itself as an increase in the width of the peaks in the magnetization curves and a decrease in their relative height, as one can see from Fig. 3. This result agrees well with the conclusions made in [14, 15], where it was shown that the ratio of the peak amplitudes observed in the magnetization curves at integer f (and, hence, the depinning current) to the values obtained at intermediate f (at the "pedestal" level) decreases with decreasing temperature because of the growing self-field effect with decreasing λ. For the structure studied in our experiment, the calculated value of the fluxon size 2λ becomes equal to the structure period $a = 20$ μm at temperatures of about 6.5 K.

From the half-width of the magnetization hysteresis loops, one can estimate the fluxon depinning current at noninteger frustrations on the basis of the assumption that the currents flow over the array along concentric square circuits, in which case the half-width of a hysteresis loop is directly proportional to the current. For square lines of current, a simple calculation yields the following expression for the magnetic moment of the array: $M = I_{dep}N^3a^2/6$, where I_{dep} is the depinning current, which is assumed to be constant over the entire array. One can expect that real lines of current deviate from square ones by "cutting" the angles, and therefore the simplest model provides a somewhat underestimated value.

Figure 4 shows the temperature dependence of the depinning current I_{dep} estimated by the aforementioned method (on the logarithmic scale). The solid line shows the theoretical dependence for a square array, which, according to [12, 14] with allowance for the self-field effect of currents, yields $I_{dep} = 0.1I_c(1 + 1.5a/\lambda)$, where I_c is the critical current of a single junction. The temperature dependence of I_c for an SNS-type junction in the "dirty" limit is expressed as $I_c = 0.1I_c(0)(1 - T/T_C)^2 e^{-\alpha\sqrt{T}}$, where $T_c = 9.2$ K is the superconducting transition temperature of the Josephson junction banks (see, e.g., [16]). The coefficient $\alpha = 3.6$ was determined from the direct measurements of the critical current through a single SNS Josephson junction with a normal interlayer of the same composition. The value of the factor $I_c(0) = 3.6$ A was determined by fitting to the experiment in the temperature region near T_c, and it is close to the value $I_c(0) = 3.9$ A obtained from the direct measurements of the critical current of a single junction. One can see that above 3.7 K the experimental data agree well with the theoretical dependence, but at low temperatures, a noticeable discrepancy is observed. Presumably, this occurs because of the considerable curvature of the field lines and their concentration near the edge of the array. As a result, the magnetic field in this region considerably exceeds the external field and can noticeably suppress the critical currents of the junctions. The suppression is strongest for the currents circulating along the edges, i.e., the currents that have the maximal circuit areas and make the maximal contributions to the total magnetic moment. When the temperature is sufficiently high, the critical currents are small, and the suppression does not manifest itself, because the magnetic field rather easily penetrates into the structure, and, hence, no field concentration at the array edge takes place.

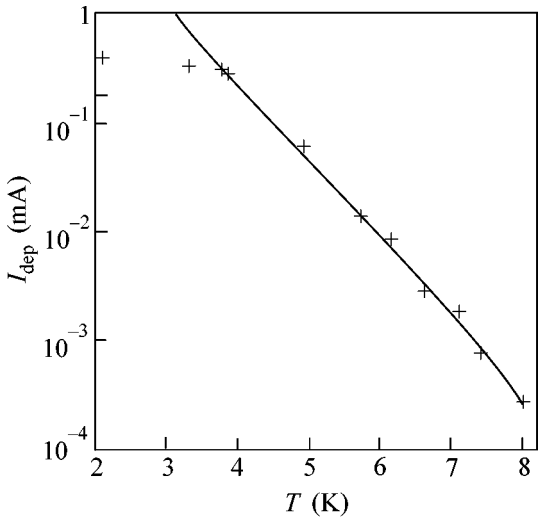

Fig. 4. Temperature dependence of the depinning current of a Josephson junction array.

In closing, it should be noted that the study of the mechanisms underlying the interesting phenomenon of asymmetry in the magnetic flux dynamics requires additional experiments with regular Josephson junction arrays of different types (SIS and SNS) and with different junction characteristics, such as critical current densities, junction dimensions, and distances between the superconducting banks.

This work was supported by the Russian Foundation for Basic Research (project no. 02-02-16564) and the State program "High-Temperature Superconductivity" (project no. 023-02).

REFERENCES

1. J. M. Kosterlitz and D. J. Thouless, J. Phys. C **6**, 1181 (1973); V. L. Berezinskii, Zh. Éksp. Teor. Fiz. **61**, 1144

(1971) [Sov. Phys. JETP **34**, 610 (1971)]; Zh. Éksp. Teor. Fiz. **59**, 907 (1970) [Sov. Phys. JETP **32**, 493 (1970)].

2. S. R. Stenoy, J. Phys. C **18**, 1543 (1985); **18**, 5163 (1985); R. Mehrotra and S. R. Stenoy, Europhys. Lett. **9**, 11 (1989); J. S. Chung, K. H. Lee, and D. Stroud, Phys. Rev. B **40**, 6570 (1989); K. K. Mon and S. Teitel, Phys. Rev. Lett. **62**, 673 (1989); W. Xia and P. L. Leath, Phys. Rev. Lett. **63**, 1428 (1989); P. L. Leath and W. Xia, Phys. Rev. B **44**, 9619 (1991); D. Domínguez, Phys. Rev. Lett. **72**, 3096 (1994); F. Falo, A. P. Bishop, and P. S. Lomdahl, Phys. Rev. B **41**, 10983 (1990); N. Gronbech-Jensen, A. R. Bishop, F. Falo, and P. S. Lomdahl, Phys. Rev. B **46**, 11149 (1992).
3. P. Barbara, A. B. Cawthorne, S. V. Shitov, and C. J. Lobb, Phys. Rev. Lett. **82**, 1963 (1999).
4. D. Domínguez and J. V. Jose, Phys. Rev. B **53**, 11692 (1996).
5. D.-X. Chen, J. J. Morreno, and A. Hernando, Phys. Rev. B **53**, 6579 (1996); D.-X. Chen, A. Sánchez, and A. Hernando, Phys. Rev. B **50**, 10342 (1994).
6. S. M. Ishikaev, É. V. Matizen, V. V. Ryazanov, *et al.*, Pis'ma Zh. Éksp. Teor. Fiz. **72**, 39 (2000) [JETP Lett. **72**, 26 (2000)].
7. P. Bak, C. Tang, and K. Wisenfeld, Phys. Rev. Lett. **59**, 381 (1987).
8. S. L. Ginzburg, Zh. Éksp. Teor. Fiz. **106**, 607 (1994) [JETP **79**, 334 (1994)].
9. S. L. Ginzburg and N. E. Savitskaya, Pis'ma Zh. Éksp. Teor. Fiz. **73**, 163 (2001) [JETP Lett. **73**, 145 (2001)].
10. S. M. Ishikaev and E. V. Matizen, in *High Temperature Superconductivity: New Materials and Properties, Joint Symposium of the SB RAS and the CNEAS TU, Tohoku University, Japan, 1999*, p. 65; S. M. Ishikaev, Prib. Tekh. Éksp., No. 3, 145 (2002).
11. L. N. Vu, M. S. Wistrom, and D. J. Van Harlingen, Appl. Phys. Lett. **63**, 1693 (1993).
12. M. S. Rzchowski, S. P. Benz, M. Tinkham, and C. J. Lobb, Phys. Rev. B **42**, 2041 (1990).
13. B. Y. Zhu, L. V. Look, V. V. Moshchalkov, *et al.*, Phys. Rev. B **64**, 12504 (2001).
14. T. E. Trias, J. R. Philips, H. S. J. van der Zant, and T. P. Orlando, IEEE Trans. Appl. Supercond. **5**, 2707 (1995).
15. J. R. Philips, H. S. J. van der Zant, J. White, and T. P. Orlando, Phys. Rev. B **47**, 5219 (1993).
16. A. Barone and G. Paterno, *Physics and Applications of the Josephson Effect* (Wiley, New York, 1982; Mir, Moscow, 1984).

Translated by E. Golyamina

JETP Letters, Vol. 76, No. 3, 2002, pp. 165–169. Translated from Pis'ma v Zhurnal Éksperimental'noĭ i Teoreticheskoĭ Fiziki, Vol. 76, No. 3, 2002, pp. 199–203.

Photoinduced Transition of $[Fe(CN)_5NO]$ Nitroprusside Anions to Metastable States and Electron Localization in the $(BEDT\text{-}TTF)_4K[Fe(CN)_5NO]_2$ Molecular Metal

S. V. Kapelnitsky[1, 2], E. B. Yagubskiĭ[2], L. A. Kushch[2], and I. Yu. Shevyakova[2]

[1] *Russian Research Centre Kurchatov Institute, Moscow, 123182 Russia*

[2] *Institute of Problems of Chemical Physics, Russian Academy of Sciences, p/o Chernogolovka, Moscow region, 142432 Russia*

e-mail: kapelnitsky@imp.kiae.ru

Received June 25, 2002

The crystals of $(BEDT\text{-}TTF)_4K[Fe(CN)_5NO]_2$, representing a quasi-two-dimensional organic metal with conducting layers of bis(ethylenedithio)tetrathiofulvalene (BEDT-TTF) and nonconducting layers containing photochromic nitroprusside anions $[Fe(CN)_5NO]^{2-}$, were studied by the method of electron spin resonance. Illuminated by light with a wavelength of 514.5 nm, the organic metal crystals feature the formation of localized paramagnetic centers in the conducting cation layers of BEDT-TTF. The phenomenon of electron localization in the BEDT-TTF layers is related to the light-induced formation of long-lived metastable states of nitroprusside anions. © *2002 MAIK "Nauka/Interperiodica".*

PACS numbers: 73.21.Ac; 71.30.+h

The crystal structure of the quasi-two-dimensional organic metal ($(BEDT\text{-}TTF)_4K[Fe(CN)_5NO]_2$ [1, 2]), which is similar to the other conductors and superconductors based on bis(ethylenedithio)tetrathiofulvalene (BEDT-TTF) [3], features the alternation of the conducting layers of BEDT-TTF radical cations and the nonconducting anion layers. The characteristic features of the given organic metal are related to the fact that the nonconducting layers contain nitroprusside (NP) anions $[Fe(CN)_5NO]^{2-}$ exhibiting photochromic properties in a number of salts.

As is known, the NP anions $[Fe(CN)_5NO]^{2-}$, exposed to the light with a wavelength of 350–540 nm at a sufficiently low temperature, exhibit a transition to two long-lived metastable states, MS1 and MS2. It should be noted that the fraction of NP anions involved in this transition does not exceed 30–50%. The reverse transition from MS1 and MS2 to the ground state (GS) takes place under the action of light with a wavelength of 620–760 nm or on heating [4–10]. The transition to the metastable states is accompanied by a reversible variation of interatomic distances in the NP anion and by a change in the anion geometry. An X-ray diffraction study [8] showed that a transition to the MS1 state alters coordination of the NO group with respect to the central Fe atom. In both GS and MS1, the atoms of Fe, N, and O forming a Fe–(N–O) group lie on the same axis, but Fe atom is bound to nitrogen in the GS and to oxygen in the MS1 configuration. Based on the X-ray diffraction data for $Na_2[Fe(CN)_5NO]_2 \cdot 2H_2O$ crystals, it was concluded [8] that the Fe–(N–O) group in the MS2 configuration exhibits bond bending, whereby the Fe–N–O angle amounts to 82° and both atoms of the NO group are coordinated to iron. However, the nature of MS2 remains unclear and is still a subject for discussion [7, 8, 11–15]. The light-induced transition of NP anions to metastable states modifies the optical properties of nitroprusside crystals [16–18]. For example, $Na_2[Fe(CN)_5NO]_2 \cdot 2H_2O$ crystals exhibit a reversible change of color. The photochromic properties of nitroprusside salts are of interest from the standpoint of possible applications in light-controlled data storage devices with high-density recording [17, 18].

The structure of $(BEDT\text{-}TTF)_4K[Fe(CN)_5NO]_2$ is characterized by short contacts C⋯O, S⋯N, and C⋯N between BEDT-TTF cations and NP anions, whereby the interatomic distances are smaller than the sums of the corresponding van der Waals radii [2]. Therefore, one may expect that the transition of NP anions to metastable states in this quasi-two-dimensional organic metal will modify the electronic properties of conducting cation layers. Unfortunately, until recently, investigations were restricted to the properties of nonconducting salts of NP and related anions [9, 19–21]. However, preliminary DSC data [22] showed evidence of the formation of metastable states of NP anions in the $(BEDT\text{-}TTF)_4K[Fe(CN)_5NO]_2$ crystals upon illumination. The aim of our work was to study the influence of the light-induced metastable states of NP anions on the BEDT-TTF conducting system in the $(BEDT\text{-}TTF)_4K[Fe(CN)_5NO]_2$ molecular metal by the method of electron spin resonance (ESR).

0021-3640/02/7603-0165$22.00

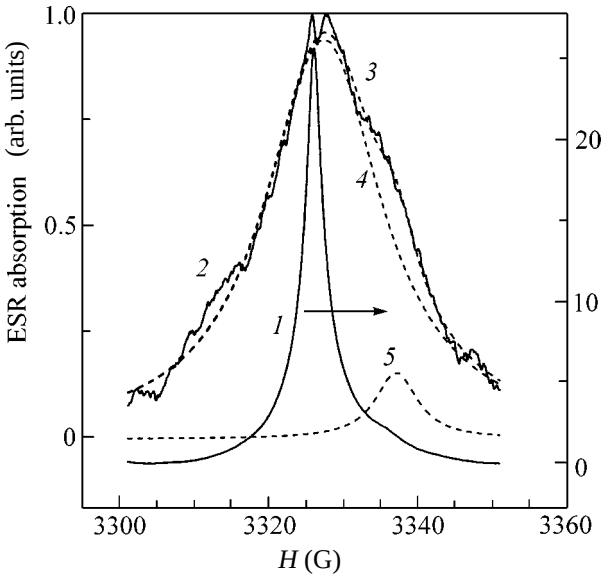

Fig. 1. ESR spectra (absorption at f = 9.4 GHz) of a $(BEDT\text{-}TTF)_4K[Fe(CN)_5NO]_2$ crystal measured at T = 6 K: (*1*) signal before laser irradiation; (*2*) additional (difference) signal D appearing after 300-min irradiation at 50 K; (*3*) approximation of the signal D by a sum of Lorentzian components D_1 and D_2 (curves *4* and *5*, respectively). The difference spectrum was calculated by formula (1) using the Lorentzian parameters and the k values determined from experimental data processed in terms of expressions (1) and (2). The right-hand ordinate scale refers to curve *1* and the left-hand scale, to curves *2*–*5*.

Measurement procedure. The ESR spectra of single crystal samples were recorded at 9.4 GHz on a Bruker ESP 300 spectrometer equipped with an ESR 900 continuous flow cryostat (Oxford Instruments). The measurements were performed using a cylindrical microwave cavity of the ER 4115 OD type intended for optical experiments. The sample crystal in the cavity was oriented so that the long axis (corresponding to the crystallographic axis *a*) coincided with the constant magnetic field direction.

The experiments involving irradiation of the $(BEDT\text{-}TTF)_4K[Fe(CN)_5NO]_2$ crystals were conducted as follows. A single crystal sample was illuminated *in situ* (in the cavity) with the light of an Ar laser at a wavelength of 514.5 nm and an intensity of 210 mW/cm^2. The incident light was polarized so that the electric field vector was perpendicular to the Fe–N–O linear bonds of NP anions. As is known, this polarization favors maximum population of metastable states in $Na_2[Fe(CN)_5NO]_2 \cdot 2H_2O$ [10]. The samples were irradiated at 50 K for 150 or 300 min, after which the ESR spectra were taken at a temperature of T = 3.3, 6, and 10 K and compared to the spectra measured before irradiation. Another series of experiments with irradiated crystals involved cyclic measurements upon annealing the sample at a gradually increased temperature T_a. Each cycle consisted in a low-temperature annealing for 2 min at a preset T_a value, followed by the ESR measurements at T = 6 K.

Results and discussion. The ESR spectrum of an unirradiated crystal contains a single symmetric line the position of which corresponds to g = 2.009. At room temperature, the line width (determined as the distance between peaks of the absorption derivative signal) is ΔH_{pp} = 34 G. As the temperature decreases, the line width monotonically decreases (to ΔH_{pp} = 1.0 G at 3.5 K). The room-temperature magnetic spin susceptibility calculated using the integral intensity of the ESR line is 6.5×10^{-4} emu/mol, which falls within the limits typical of BEDT-TTF based conductors. The susceptibility remains virtually unchanged when the temperature decreases down to 100 K (Pauli type of susceptibility). This behavior agrees with the metal-type character of the temperature dependence of the conductivity of $(BEDT\text{-}TTF)_4K[Fe(CN)_5NO]_2$ crystals [1] and indicates that the ESR signal observed is due to the spin resonance of conduction electrons in the BEDT-TTF cation layers. As the temperature decreases from 60 to 3.5 K, the magnetic susceptibility monotonically decreases approximately by a factor of 3.

The laser irradiation of a sample led to very small changes in the ESR spectra. It must be noted that the penetration depth of the light with a wavelength of 514.5 nm in a $(BEDT\text{-}TTF)_4K[Fe(CN)_5NO]_2$ crystal is as small as 0.3 μm [23], which is significantly smaller than the sample thickness (13 μm). For this reason, the ESR spectrum of a sample upon irradiation can be presented as

$$S_{irr} = kS_{bi} + D, \tag{1}$$

where $k \approx 1$, S_{bi} is the spectrum before irradiation and D is the difference spectrum. The difference spectrum was approximated by a superposition of two Lorentzian lines,

$$D \approx D_1 + D_2 = (2A_1/\pi)(\Delta H_1/(4(H - H_1)^2 + \Delta H_1^2)) + (2A_2/\pi)(\Delta H_2/(4(H - H_2)^2 + \Delta H_2^2)), \tag{2}$$

where H is the constant magnetic field; A_1, H_1, and ΔH_1 are the integral intensity, the resonance field, and the full width at half maximum (FWHM) of the first Lorentzian, respectively; and A_2, H_2, and ΔH_2 are the analogous values for the second Lorentzian. The coefficient k and the parameters of approximating Lorentzians were determined by least squares.

Figure 1 shows the spectrum of an unirradiated sample and the difference spectrum $D = S_{irr} - kS_{bi}$ obtained for the ESR measurements at T = 6 K after laser irradiation for 300 min at T = 50 K. The difference spectrum can be interpreted as containing additional signal components arising due to the irradiation. Dashed lines *4*, *5* in Fig. 1 present the two Lorentzian lines, the superposition of which is used to approximate the difference signal D. The half-width (FWHM) of the spectrum of

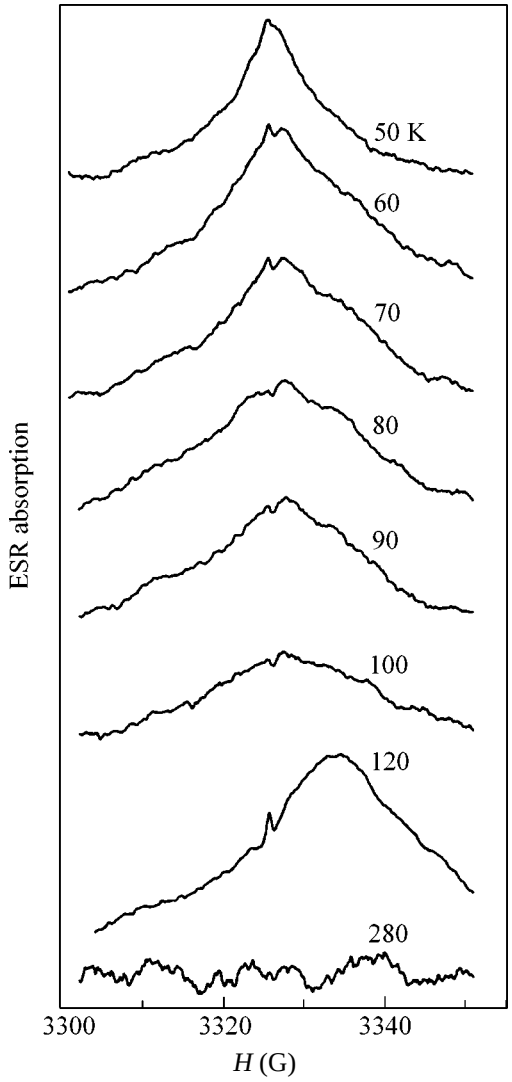

Fig. 2. Evolution of the additional (difference) signal D in the ESR spectrum of a sample irradiated for 300 min at 50 K and sequentially annealed at various temperatures T_a (indicated next to the curves). The spectra were measured at T = 6 K and the signal D was calculated by formula (1).

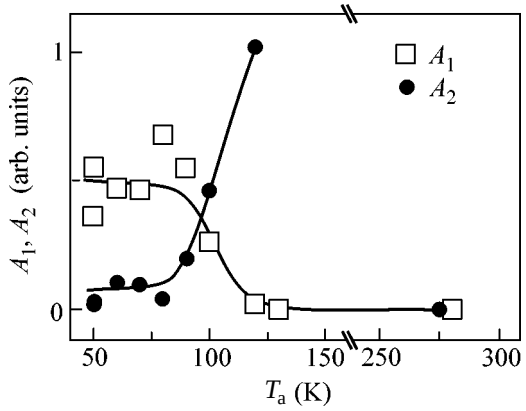

Fig. 3. Variation of the A_1 and A_2 values (integral intensities of the additional signal components D_1 and D_2, respectively) for a sample irradiated for 300 min at 50 K and then subjected to stepwise annealing at a gradually increasing temperature T_a. The ESR spectra were measured at T = 6 K and the A_1 and A_2 values were determined from the experimental data processed in terms of expressions (1) and (2). The curves are drawn for illustration.

the unirradiated sample measured at T = 6 K is ΔH = 3.3 G, while half-widths of the additional signal components D_1 and D_2 arising after a 300-min laser irradiation amount to 7 and 10 G, respectively. The intensities of the D_1 and D_2 signals increase with the irradiation time.

One of the Lorentzians (e.g., that denoted by D_1) is characterized by the same resonance field as that of the conduction electron spin resonance (CESR) (see Fig. 1). When the constant magnetic moment is oriented along the *a* axis, the *g* value corresponding to the D_1 signal component is 2.009, while the value corresponding to D_2 is g = 2.004. Coincidence of the resonance field of the additional signal D_1 and CESR was also observed when the constant magnetic moment was oriented along the *b* axis, which is evidence that the D_1 signal is due to electrons of the cation layers of BEDT-TTF. Elucidation of the nature of the second signal component (D_2) requires additional investigation. However, we can point out that the results of ESR [12] and magnetic susceptibility [21] measurements for various nitroprussides show that the $[Fe(CN)_5NO]^{2-}$ anions are diamagnetic in both ground and metastable states.

Figure 2 shows the evolution of the additional (difference) signal D for the sample irradiated for 300 min, observed in the course of a sequential increase in the annealing temperature T_a. The ESR spectra were measured at 6 K and the difference signal intensity was calculated by formula (1). As can be seen, the additional signal varies rather slightly for the sample annealed at T_a < 90 K; after annealing at T_a = 280 K, signal D disappears. Figure 3 shows plots of the A_1 and A_2 values, representing the intensities of the additional signal components D_1 and D_2, respectively, versus the annealing temperature T_a. In the interval of 90 K < T_a < 130 K, a decrease in A_1 is accompanied by an increase in A_2; the latter component disappears in the interval of 130 K < T_a < 280 K. The presence of two signals from paramagnetic centers characterized by significantly different thermal stability is probably explained by the existence of two metastable states of NP anions in $(BEDT\text{-}TTF)_4K[Fe(CN)_5NO]_2$ crystals, which are populated in the course of illumination.

Here and below, we imply by MS1 and MS2 the metastable states of NP anions possessing lower and higher thermal stability, respectively. A decrease in the D_1 signal intensity upon annealing at $T_a \geq 90$ K can be explained by the decrease in the MS1 concentration. An

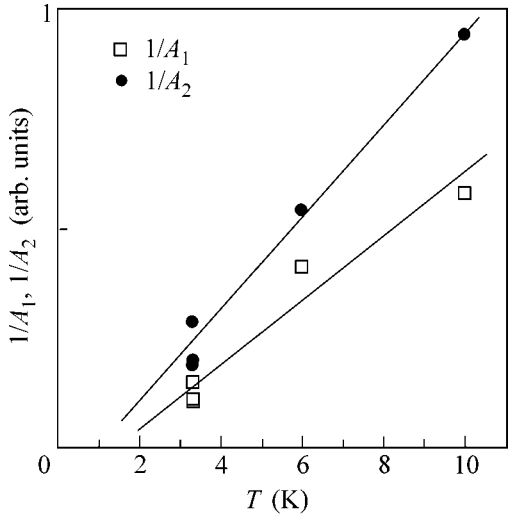

Fig. 4. The temperature variation of the A_1 and A_2 values (integral intensities of the additional signal components D_1 and D_2, respectively) for a sample irradiated for 150 min at 50 K; symbols represent the experimental data, straight lines correspond to the Curie–Weiss law for magnetic susceptibility. The A_1 and A_2 values were determined from experimental data processed in terms of expressions (1) and (2).

increase in intensity of the D_2 signal at the expense of decreasing the D_1 signal indicates that (i) at least a part of MS1 converts into MS2 and (ii) a metastable state of lower energy (MS2) possesses a higher thermal stability than the state of higher energy (MS1). In most nitroprussides, a two-stage character of the thermoactivated transition MS1⟶MS2⟶GS is usually not detected because the rate of the second stage (MS2⟶GS) is much greater than that of the first stage (MS1⟶MS2). Previously, the thermoactivated MS1⟶MS2 transition was revealed by IR spectroscopy in a photochromic osmium mononitrosyl complex $Na_2[Os(CN)_5NO] \cdot H_2O$ [20].

The results of our ESR measurements indicate that MS1 possesses a lower thermal stability in (BEDT-TTF)$_4$K[Fe(CN)$_5$NO]$_2$ than in $Na_2[Fe(CN)_5NO]_2 \cdot 2H_2O$ (the MS1 lifetime of the latter complex at T = 140 K exceeds 10^4 s [5]). The lower thermal stability in the former case is apparently related to the interaction between NP anions and BEDT-TTF cations, which results in the distance between Fe and N atoms in the nitroprusside anion of (BEDT-TTF)$_4$K[Fe(CN)$_5$NO]$_2$ [2] being significantly different from that in $Na_2[Fe(CN)_5NO]_2 \cdot 2H_2O$ [8].

Figure 4 shows the temperature dependence of the integral intensities A_1 and A_2 of the additional ESR signal components D_1 and D_2, respectively, in a sample irradiated for 150 min. As can be seen, the character of this dependence differs from that of the CESR signal measured before irradiation. The observed behavior of A_1 and A_2 (proportional to the corresponding magnetic susceptibilities) agrees with the Curie–Weiss law. This temperature dependence of the magnetic susceptibility is evidence that the D_1 and D_2 signals are due to localized spins rather than the spins of conduction electrons. The concentration of these spins can be estimated from the additional signal intensity. Assuming that the D_1 and D_2 signals are produced by spins S = 1/2 occurring within the light penetration depth, we obtain 3% per formula unit for a crystal irradiated for 300 min at T = 50 K and 10% for the same exposure followed by a single low-temperature annealing (30 min at 100 K). Coincidence of the g value, corresponding to the D_1 signal assigned to the localized magnetic moments, with the g value for the CESR signal from BEDT-TTF cation layers shows evidence for the localization of electrons taking place in the conducting layers of the (BEDT-TTF)$_4$K[Fe(CN)$_5$NO]$_2$ organic metal.

A possible reason for the transition of conduction electrons to the localized state may be the appearance of a fluctuating potential (Anderson's localization) in the BEDT-TTF layers that is related to the transition of a part of NP anions to the metastable state as a result of the laser irradiation. At present, it is still unclear whether a metal–insulator transition actually takes place in the (BEDT-TTF)$_4$K[Fe(CN)$_5$NO]$_2$ crystals within the light penetration depth. However, it is highly probable that the illumination at low temperatures may lead to reversible changes in the optical properties and conductivity of this organic metal due to electron localization in the BEDT-TTF layers.

The authors are grateful to R.P. Shibaeva and S.S. Khasanov for fruitful discussions of the results and to I.S. Grigor'ev and G.G. Grigoryan for their help in creating an optical attachment to the ESR spectrometer. This study was supported by the Russian Foundation for Basic Research (project no. 00-03-2200 NTsNI) and by INTAS (grant no. 00-0651).

REFERENCES

1. L. Kushch, L. Buravov, V. Tkacheva, *et al.*, Synth. Met. **102**, 1646 (1999).
2. S. Khasanov, L. Zorina, and R. Shibaeva, Koord. Khim. **27**, 283 (2001).
3. E. B. Yagubskii, Mol. Cryst. Liq. Cryst. **230**, 139 (1993).
4. Th. Woike, W. Krasser, and P. S. Bechthold, Phys. Rev. Lett. **53**, 1767 (1984).
5. H. Zollner, Th. Woike, W. Krasser, and S. Haussühl, Z. Kristall. **188**, 139 (1989).
6. Th. Woike, W. Kirchner, H. Kim, *et al.*, Hyperfine Interact. **7**, 265 (1993).
7. J. A. Guida, P. J. Aymonino, O. E. Piro, and E. E. Castellano, Spectrochim. Acta A **49**, 535 (1993).
8. M. D. Carducci, M. R. Pressprich, and P. Coppens, J. Am. Chem. Soc. **119**, 2669 (1997).
9. H. Zollner, W. Krasser, Th. Woike, and S. Haussühl, Chem. Phys. Lett. **161**, 497 (1989).

10. Th. Woike, W. Krasser, H. Zöllner, *et al.*, Z. Phys. D **25**, 51 (1993).
11. J. Tritt-Goc, Mol. Phys. Rep. **14**, 119 (1996).
12. C. Terrile, O. R. Nascimento, I. J. Moraes, *et al.*, Solid State Commun. **73**, 481 (1990).
13. V. Rusanov, V. Angelov, J. Angelova, *et al.*, J. Solid State Chem. **123**, 39 (1996).
14. J. Tritt-Goc, N. Pislewski, and S. K. Hoffmann, Chem. Phys. Lett. **102**, 471 (1997).
15. J. Schefer, Th. Woike, M. Imlau, and B. Delley, Eur. Phys. J. B **3**, 349 (1998).
16. Th. Woike, Th. Barthel, G. Schetter, *et al.*, Laser Optoelektron. **25**, 18 (1993).
17. Th. Woike, W. Kirchner, G. Schetter, *et al.*, Opt. Commun. **106**, 6 (1994).
18. Th. Woike, M. Imlau, S. Haussühl, *et al.*, Phys. Rev. B **58**, 8411 (1998).
19. P. Coppens, D. Fomitchev, M. D. Carducci, and K. J. Culp, J. Chem. Soc., Dalton Trans. 865 (1998).
20. J. A. Guida, O. E. Piro, and P. J. Aymonino, Inorg. Chem. **34**, 4113 (1995).
21. M. Clemente-León, E. Coronado, J. R. Galán-Mascarós, *et al.*, Inorg. Chem. **40**, 87 (2001).
22. S. Schmickler, M. Imlau, Th. Woike, *et al.*, Z. Kristallogr., Suppl. Issue, No. 16, 96 (1999).
23. M. Maksimuk, private communication.

Translated by P. Pozdeev

JETP Letters, Vol. 76, No. 3, 2002, pp. 170–174. From Pis'ma v Zhurnal Éksperimental'noĭ i Teoreticheskoĭ Fiziki, Vol. 76, No. 3, 2002, pp. 204–208.

Electric Field Dependence of the Thermal Conductivity of a Granular Superconductor: Giant Field-Induced Effects Predicted¶

S. A. Sergeenkov

Bogoliubov Laboratory of Theoretical Physics, Joint Institute for Nuclear Research, 141980 Dubna, Moscow region, Russia

Received June 3, 2002; in final form, July 1, 2002

The temperature and electric-field dependence of the electronic contribution to the thermal conductivity (TO) of a granular superconductor is considered within a 3D model of inductive Josephson junction arrays. In addition to a low-temperature maximum of zero-field TC $\kappa(T, 0)$ (controlled by mutual inductance L_0 and normal state resistivity R_n), the model predicts the two major effects in the applied electric field: (i) the decrease in the linear TC and (ii) the giant enhancement of the nonlinear (i.e. ∇T-dependent) TC with $\Delta\kappa(T, E)/\kappa(T, 0)$, reaching 500% for parallel electric fields $E \simeq E_T$ ($E_T = S_0|\nabla T|$ is an "intrinsic" thermoelectric field). The possibility of experimentally observing the predicted effects in granular superconductors is discussed. © *2002 MAIK "Nauka/Interperiodica".*

PACS numbers: 74.25.Fy; 74.50.+r; 74.80.Bj

1. INTRODUCTION

Inspired by new possibilities offered by cutting-edge nanotechnologies, the experimental and theoretical physics of increasingly sophisticated mesoscopic quantum devices (heavily based on Josephson junctions and their arrays) is becoming one of the most exciting and rapidly growing areas of modern science [1–3]. In addition to the traditional fields of expertise (such as granular superconductors [2]), Josephson junction arrays (JJAs) are actively used for testing principally novel ideas (e.g., topologically protected quantum bits [3]) in a bid to solve probably one of the most challenging problems in quantum computing. Though traditionally the main emphasis in studying JJAs has been on their behavior in applied magnetic fields, recently special attention has been given to the so-called electric field effects (FEs) in JJs and granular superconductors [4–9]. The unusually strong FEs observed in bulk high-T_c superconducting (HTS) ceramics [4] (including the substantial enhancement of the critical current, reaching $\Delta I_c(E)/I_c(0) = 100\%$ for $E = 10^7$ V/m) have been attributed to a crucial modification of the original weak-link structure under the influence of very strong electric fields. This hypothesis has been corroborated by further investigations, both experimental (through observation of the correlation between the critical current behavior and type of weak links [5]) and theoretical (by studying the FEs in *SNS*-type structures [6] and *d*-wave granular superconductors [7]). Among other interesting field-induced effects, one can mention the FE-based Josephson transistor [8] and the Josephson analogue of the *magnetoelectric effect* [9] (electric field generation of Josephson magnetic moment in zero magnetic field). At the same time, very little is known about the influence of electric fields on thermal transport properties of granular superconductors. In an attempt to shed some light on this interesting and important (for potential applications) problem, in this letter we present a theoretical study of the electric-field and temperature dependence of the electronic contribution to the thermal conductivity (TC) κ of a granular superconductor (described by a 3D model of inductive JJAs). As we shall see below, in addition to a low-temperature maximum of zero-field TC $\kappa(T, 0)$ (controlled by the mutual inductance L_0 and normal state resistivity R_n), the model predicts unusually strong (giant) field-induced effects in the behavior of nonlinear (i.e. ∇T-dependent) TC. In particular, it is estimated that the absolute values of the TC enhancement $\Delta\kappa(T, E)/\kappa(T, 0)$ can reach up to 500% for relatively low (in comparison with the fields needed to observe a critical current enhancement [4, 5]) applied electric fields E that match an intrinsic thermoelectric field $E_T = S_0|\nabla T|$. The estimates of the model parameters suggest quite an optimistic possibility of observing the predicted effects in granular superconductors and JJAs.

2. THE MODEL

To adequately describe the thermodynamic behavior of a real granular superconductor for all temperatures and under the simultaneous influence of arbitrary electric field E and thermal gradient ∇T, we consider one of

¶ This article was submitted by the author in English.

the numerous versions of the 3D JJAs models based on the following Hamiltonian

$$\mathcal{H}(t) = \mathcal{H}_T(t) + \mathcal{H}_L(t) + \mathcal{H}_E(t), \quad (1)$$

where

$$\mathcal{H}_T(t) = \sum_{ij}^{N} J_{ij}[1 - \cos\phi_{ij}(t)] \quad (2)$$

is the well-known tunneling Hamiltonian,

$$\mathcal{H}_L(t) = \sum_{ij}^{N} \frac{\Phi_{ij}^2(t)}{2L_{ij}} \quad (3)$$

accounts for the mutual inductance L_{ij} between grains (and controls the normal state value of the thermal conductivity, see below) with $\Phi_{ij}(t) = (\hbar/2e)\phi_{ij}(t)$ being the total magnetic flux through an array, and finally

$$\mathcal{H}_E(t) = -\mathbf{p}(t)\mathbf{E} \quad (4)$$

describes the electric field induced polarization contribution, where the polarization operator

$$\mathbf{p}(t) = -2e\sum_{i=1}^{N} n_i(t)\mathbf{r}_i. \quad (5)$$

Here, n_i is the pair number operator and $\mathbf{r}_i$ is the coordinate of the center of the grain.

As usual, the tunneling Hamiltonian $\mathcal{H}_T(t)$ describes the short-range interaction between N superconducting grains arranged in a 3D lattice with coordinates $\mathbf{r}_i = (x_i, y_i, z_i)$. The grains are separated by insulating boundaries producing the temperature-dependent Josephson coupling $J_{ij}(T) = J_{ij}(0)F(T)$ with

$$F(T) = \frac{\Delta(T)}{\Delta(0)}\tanh\left[\frac{\Delta T}{2k_BT}\right] \quad (6)$$

and $J_{ij}(0) = [\Delta(0)/2](R_0/R_{ij})$, where $\Delta(T)$ is the temperature-dependent gap parameter, $R_0 = h/4e^2$ is the quantum resistance, and R_{ij} is the resistance between grains in their normal state that is assumed [10] to vary exponentially with the distance $\mathbf{r}_{ij}$ between neighboring grains; i.e., $R_{ij}^{-1} = R_n^{-1}\exp(-r_{ij}/d)$ (where d is of the order of an average grain size).

As is well-known [2, 10], a constant electric field E and a thermal gradient ∇T applied to a *JJA* cause the time evolution of the initial phase difference $\phi_{ij}^0 = \phi_i - \phi_j$ as follows:

$$\phi_{ij}(t) = \phi_{ij}^0 + \omega_{ij}(\mathbf{E}, \nabla T)t. \quad (7)$$

Here, $\omega_{ij} = 2e(\mathbf{E} - \mathbf{E}_T)\mathbf{r}_{ij}/\hbar$, where $\mathbf{E}_T = S_0\nabla T$ is an "intrinsic" thermoelectric field with S_0 being a zero-field value of the Seebeck coefficient.

3. LINEAR THERMAL CONDUCTIVITY (FOURIER LAW)

We start our consideration by discussing the temperature behavior of the conventional (that is, *linear*) thermal conductivity of a granular superconductor in an arbitrary applied electric field E, paying special attention to its evolution with a mutual inductance L_{ij}. For simplicity, in what follows we will limit our consideration to the longitudinal component of the total thermal flux $\mathbf{Q}(t)$ which is defined (in a q-space representation) via the total energy conservation law as follows:

$$\mathbf{Q}(t) \equiv \lim_{\mathbf{q}\to 0}\left[i\frac{\mathbf{q}}{\mathbf{q}^2}\dot{\mathcal{H}}_{\mathbf{q}}(t)\right], \quad (8)$$

where $\dot{\mathcal{H}}_{\mathbf{q}} = \partial\mathcal{H}_{\mathbf{q}}/\partial t$ with

$$\mathcal{H}_{\mathbf{q}}(t) = \frac{1}{v}\int d^3x e^{i\mathbf{q}\mathbf{r}}\mathcal{H}(\mathbf{r}, t). \quad (9)$$

Here, $v = 8\pi d^3$ is the properly defined normalization volume, and we made a usual substitution $\frac{1}{N}\sum_{ij}A(r_{ij}, t) \longrightarrow \frac{1}{v}\int d^3xA(\mathbf{r}, t)$ valid in the long-wavelength approximation ($\mathbf{q} \longrightarrow 0$).

In turn, the heat flux $\mathbf{Q}(t)$ introduced above is related to the appropriate components of the linear thermal conductivity (LTC) tensor $\kappa_{\alpha\beta}$ as follows (hereafter, $\{\alpha, \beta\} = x, y, z$):

$$\kappa_{\alpha\beta}(T, \mathbf{E}) \equiv -\frac{1}{V}\left[\frac{\partial\overline{\langle Q_\alpha\rangle}}{\partial(\nabla_\beta T)}\right]_{\nabla T = 0}, \quad (10)$$

where

$$\overline{\langle Q_\alpha\rangle} = \frac{1}{\tau}\int_0^\tau dt\langle Q_\alpha(t)\rangle. \quad (11)$$

Here, V is a sample's volume, τ is the characteristic Josephson time for the network, and $\langle\ldots\rangle$ denotes thermodynamic averaging over the initial phase differences ϕ_{ij}^0

$$\langle A(\phi_{ij}^0)\rangle = \frac{1}{Z}\int_0^\pi\prod_{ij}d\phi_{ij}^0 A(\phi_{ij}^0)e^{-\beta H_0} \quad (12)$$

with an effective Hamiltonian

$$H_0[\phi_{ij}^0] = \int_0^\tau\frac{dt}{\tau}\int\frac{d^3x}{V}\mathcal{H}(\mathbf{r}, t). \quad (13)$$

Here, $\beta = 1/k_BT$, and $Z = \int_0^\pi\prod_{ij}d\phi_{ij}^0 e^{-\beta H_0}$ is the partition function. The averaging procedure defined above allows us to study the temperature evolution of the system.

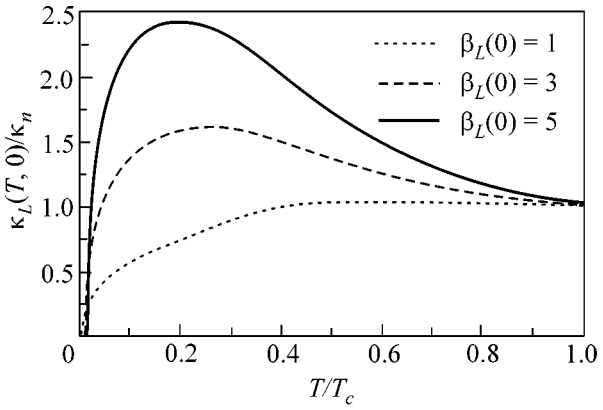

Fig. 1. Temperature dependence of the zero-field linear thermal conductivity $\kappa_L(T, 0)/\kappa_n$ for different values of the dimensionless parameter $\beta_L(0)$.

Taking into account that in JJAs [11] $L_{ij} \propto R_{ij}$, we obtain $L_{ij} = L_0 \exp(r_{ij}/d)$ for the explicit r-dependence of the weak-link inductance in our model. Finally, in view of Eqs. (1)–(13) and making use of the usual "phase-number" commutation relation $[\phi_i, n_j] = i\delta_{ij}$, we find the following analytical expression for the temperature and electric field dependence of the electronic contribution to the linear thermal conductivity of a granular superconductor:

$$\kappa_{\alpha\beta}(T, \mathbf{E}) = \kappa_0[\delta_{\alpha\beta}\eta(T, \epsilon) + \beta_L(T)\nu(T, \epsilon) f_{\alpha\beta}(\epsilon)], \tag{14}$$

where

$$f_{\alpha\beta}(\epsilon) = \frac{1}{4}[\delta_{\alpha\beta}A(\epsilon) - \epsilon_\alpha\epsilon_\beta B(\epsilon)] \tag{15}$$

with

$$A(\epsilon) = \frac{5 + 3\epsilon^2}{(1 + \epsilon^2)^2} + \frac{3}{\epsilon}\tan^{-1}\epsilon \tag{16}$$

and

$$B(\epsilon) = \frac{3\epsilon^4 + 8\epsilon^4 - 3}{\epsilon^2(1 + \epsilon^2)^3} + \frac{3}{\epsilon^3}\tan^{-1}\epsilon. \tag{17}$$

Here, $\kappa_0 = Nd^2S_0\Phi_0/VL_0$, $\beta_L(T) = 2\pi I_c(T)L_0/\Phi_0$ with $I_c(T) = (2e/\hbar)J(T)$ being the critical current (we neglect the possible field dependence of I_c because, as we shall see below, the characteristic fields where the thermal conductivity exhibits the most interesting behavior are much lower than those needed to produce a tangible change of the critical current [4]), $\epsilon \equiv \sqrt{\epsilon_x^2 + \epsilon_y^2 + \epsilon_z^2}$ with $\epsilon_\alpha = E_\alpha/E_0$, and $E_0 = \hbar/2ed\tau$ is a characteristic electric field. In turn, the "order parameters" of the system introduced above, $\eta(T, \epsilon) \equiv \langle\phi_{ij}^0\rangle$ and $\nu(T, \epsilon) \equiv \langle\sin\phi_{ij}^0\rangle$, are defined as follows:

$$\eta(T, \epsilon) = \frac{\pi}{2} - \frac{4}{\pi}\sum_{n=0}^{\infty}\frac{1}{(2n+1)^2}\left[\frac{I_{2n+1}(\beta_E)}{I_0(\beta_E)}\right] \tag{18}$$

and

$$\nu(T, \epsilon) = \frac{\sinh\beta_E}{\beta_E I_0(\beta_E)}, \tag{19}$$

where

$$\beta_E(T, \epsilon) = \frac{\beta J(T)}{2}\left(\frac{1}{1 + \epsilon^2} + \frac{1}{\epsilon}\tan^{-1}\epsilon\right). \tag{20}$$

Here, $J(T) = J(0)F(T)$ with $J(0) = (\Delta_0/2)(R_0/R_n)$ and $F(T)$ given by Eq. (6); $I_n(x)$ stand for the appropriate modified Bessel functions.

3.1. Zero-field effects. Turning to the discussion of the results obtained, we start with a more simple zero-field case. The relevant parameters affecting the behavior of the LTC in this particular case include the mutual inductance L_0 and the normal state resistance between grains R_n. For the temperature dependence of the Josephson energy (see Eq. (6)), we used the well-known [12] approximation for the BCS gap parameter, which is valid for all temperatures, $\Delta(T) = \Delta(0)\tanh(\gamma\sqrt{(T_c - T)/T})$ with $\gamma = 2.2$.

Despite the rather simplified nature of our model, it seems to describe quite reasonably the behavior of the LTC for all temperatures. Indeed, in the absence of an applied electric field ($E = 0$), the LTC is isotropic (as expected), $\kappa_{\alpha\beta}(T, 0) = \delta_{\alpha\beta}\kappa_L(T, 0)$, where $\kappa_L(T, 0) = \kappa_0[\eta(T, 0) + 2\beta_L(T)\nu(T, 0)]$ vanishes at zero temperature and reaches a normal state value $\kappa_n \equiv \kappa_L(T_c, 0) = (\pi/2)\kappa_0$ at $T = T_c$. Figure 1 shows the temperature dependence of the normalized LTC $\kappa_L(T, 0)/\kappa_n$ for different values of the dimensionless parameter $\beta_L(0) = 2\pi I_c(0)L_0/\Phi_0$. As is clearly seen, with an increase in this parameter, the LTC evolves from a flatlike pattern (for relatively small values of L_0) to a low-temperature maximum (for higher values of $\beta_L(0)$). Notice that the peak temperature T_p is virtually insensitive to the variation of the inductance parameter L_0, while being at the same time strongly influenced by resistivity R_n. Indeed, the curves presented here correspond to the resistance ratio $r_n = R_0/R_n = 1$ (a highly resistive state). It can be shown that a different choice of r_n leads to quite a tangible shift of the maximum; namely, the smaller the normal resistance between grains R_n (or the better the quality of the sample), the higher the temperature at which the peak is developed. As a matter of fact, the peak temperature T_p is related to the so-called phase-locking temperature T_J (which marks the attainment of phase coherence between the adjacent grains in the array and always lies

below the superconducting temperature T_c of a single grain), which is usually defined via an average (per grain) Josephson coupling energy as [13] $J(T_J, r_n) = k_B T_J$. In particular, for $T \simeq T_c$, it can be shown analytically that $T_J(r_n)$ indeed increases with r_n as $T_J(r_n)/T_c \simeq r_n/(1 + r_n)$.

3.2. Electric field effects. Turning to the discussion of the LTC behavior in an applied electric field, let us demonstrate first its anisotropic nature. For simplicity (but without losing generality), we assume that $\mathbf{E} = (E, 0, 0)$ and $\nabla T = (\nabla_x T, \nabla_y T, 0)$. Such a choice of the external fields allows us to consider both parallel $\kappa_{xx}(T, E)$ and perpendicular $\kappa_{yy}(T, E)$ components of the LTC corresponding to the two most interesting configurations, $\mathbf{E} \parallel \nabla T$ and $\mathbf{E} \perp \nabla T$, respectively. The inset in Fig. 2 demonstrates the predicted electric field dependence of the normalized LTC $\kappa_L(T, E)/\kappa_L(T, 0)$ for both configurations taken at $T = 0.2T_c$ (with $r_n = 1$ and $\beta_L(0) = 1$). First of all, we note that both components of the LTC decrease as the field E/E_0 increases. Secondly, the normal component κ_{yy} decreases more slowly than the parallel one κ_{xx}, thus suggesting some kind of anisotropy in the system. In view of the structure of Eq. (14), the same behavior is also expected for the temperature dependence of the field-induced LTC; that is, $\Delta\kappa_L(T, E)/\kappa_L(T, 0) < 0$ for all fields and temperatures. In terms of the absolute values, for $T = 0.2T_c$ and $E = E_0$, we obtain $[\Delta\kappa_L(T, E)/\kappa_L(T, 0)]_{xx} = 90\%$ and $[\Delta\kappa_L(T, E)/\kappa_L(T, 0)]_{yy} = 60\%$ for the attenuation of LTC in an applied electric field.

4. NONLINEAR THERMAL CONDUCTIVITY: GIANT FIELD-INDUCED EFFECTS

Let us turn now to the most intriguing part of this paper and consider the nonlinear generalization of the Fourier law and the very unusual behavior of the resulting nonlinear thermal conductivity (NLTC) under the influence of an applied electric field. In what follows, by the NLTC we understand a ∇T-dependent thermal conductivity $\kappa^{NL}_{\alpha\beta}(T, \mathbf{E}) \equiv \kappa_{\alpha\beta}(T, \mathbf{E}; \nabla T)$, which is defined as follows

$$\kappa^{NL}_{\alpha\beta}(T, \mathbf{E}) \equiv -\frac{1}{V}\left[\frac{\partial \overline{\langle Q_\alpha \rangle}}{\partial(\nabla_\beta T)}\right]_{\nabla T \neq 0} \tag{21}$$

with $\overline{\langle Q_\alpha \rangle}$ given by Eq. (11).

Repeating the same procedure as before, we obtain finally for the relevant components of the NLTC tensor

$$\kappa^{NL}_{\alpha\beta}(T, \mathbf{E}) = \kappa_0[\delta_{\alpha\beta}\eta(T, \epsilon_{\text{eff}}) + \beta_L(T)\nu(T, \epsilon_{\text{eff}})D_{\alpha\beta}(\epsilon_{\text{eff}})], \tag{22}$$

where

$$D_{\alpha\beta}(\epsilon_{\text{eff}}) = f_{\alpha\beta}(\epsilon_{\text{eff}}) + \epsilon^\gamma_T g_{\alpha\beta\gamma}(\epsilon_{\text{eff}}) \tag{23}$$

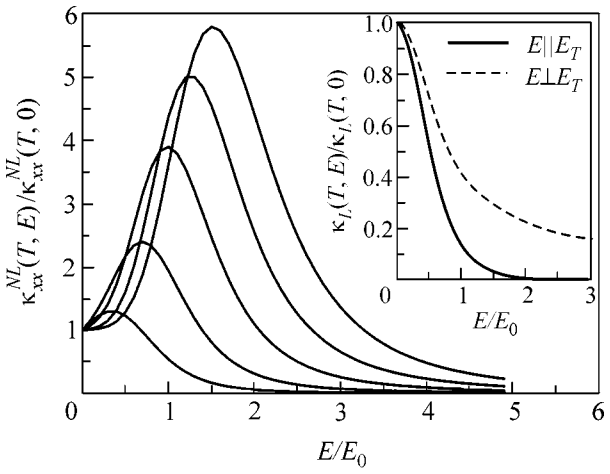

Fig. 2. Electric field dependence of the nonlinear thermal conductivity $\kappa^{NL}_{xx}(T, E)/\kappa^{NL}_{xx}(T, 0)$ for different values of the applied thermal gradient $\epsilon_T = S_0|\nabla T|/E_0$ ($\epsilon_T = 0.2$; 0.4; 0.6; 0.8; 1.0, increasing from bottom to top). Inset: Electric field dependence of the linear thermal conductivity $\kappa_L(T, E)/\kappa_L(T, 0)$ for parallel ($\mathbf{E} \parallel \nabla T$) and perpendicular ($\mathbf{E} \perp \nabla T$) configurations.

with

$$g_{\alpha\beta\gamma}(\epsilon) = \frac{1}{8}[(\delta_{\alpha\beta}\epsilon_\gamma + \delta_{\alpha\gamma}\epsilon_\beta + \delta_{\gamma\beta}\epsilon_\alpha)B(\epsilon) + 3\epsilon_\alpha\epsilon_\beta\epsilon_\gamma C(\epsilon)] \tag{24}$$

and

$$C(\epsilon) = \frac{3 + 11\epsilon^2 - 11\epsilon^4 - 3\epsilon^6}{\epsilon^4(1 + \epsilon^2)^4} - \frac{3}{\epsilon^5}\tan^{-1}\epsilon. \tag{25}$$

Here, $\epsilon^\alpha_{\text{eff}} = \epsilon^\alpha - \epsilon^\alpha_T$, where $\epsilon_\alpha = E_\alpha/E_0$ and $\epsilon^\alpha_T = E^\alpha_T/E_0$ with $E^\alpha_T = S_0\nabla_\alpha T$; the other field-dependent parameters (η, ν, B, and $f_{\alpha\beta}$) are the same as before but with $\epsilon \longrightarrow \epsilon_{\text{eff}}$.

As expected, in the limit $E_T \longrightarrow 0$ (or when $E \gg E_T$), from Eq. (22) we recover all the results obtained in the previous section for the LTC. Let us see now what happens when the "intrinsic" thermoelectric field $\mathbf{E_T} = S_0\nabla T$ becomes comparable with the applied electric field E. Figure 2 (main frame) depicts the resulting electric field dependence of the parallel component of the NLTC tensor $\kappa^{NL}_{xx}(T, E)$ for different values of the dimensionless parameter $\epsilon_T = E_T/E_0$ (the other parameters are the same as before). As is clearly seen in this picture, in sharp contrast to the field behavior of the previously considered linear TC, its nonlinear analogue evolves with the field quite differently. Namely, NLTC strongly increases for small electric fields ($E < E_m$), reaches a pronounced maximum at $E = E_m = \frac{3}{2}E_T$, and eventually declines at higher fields ($E > E_m$). Furthermore, as directly follows from the very structure of Eq. (22), a similar "reentrant-like" behavior of the nonlinear ther-

mal conductivity will occur in its temperature dependence as well. Even more remarkable is the absolute value of the field-induced enhancement. According to Fig. 2 (main frame), it is easy to estimate that near the maximum (with $E = E_m$ and $E_T = E_0$) and for $T = 0.2T_c$ one gets $\Delta\kappa_{xx}^{NL}(T, E)/\kappa_{xx}^{NL}(T, 0) \simeq 500\%$.

5. DISCUSSION

To understand the rather unusual results obtained above, let us take a closer look at the field-induced behavior of the Josephson voltage in our system (see Eq. (7)). Clearly, strong heat conduction requires the attainment of a quasi-stationary (that is nearly zero-voltage) regime within the array. In other words, the maximum of the thermal conductivity in an applied electric field should correlate with a minimum of the total voltage in the system, $V(E) \equiv (\hbar/2e)\langle\partial\phi_{ij}(t)/\partial t\rangle = V_0(\epsilon - \epsilon_T)$, where $\epsilon \equiv E/E_0$ and $V_0 = E_0 d = \hbar/2e\tau$ is the characteristic voltage. For linear TC (which is valid only for small thermal gradients with $\epsilon_T \equiv E_T/E_0 \ll 1$), the average voltage across an array $V_L(E) \simeq V_0(E/E_0)$ has a minimum at a zero applied field (where LTC indeed has its maximum value, see the inset in Fig. 2), while for nonlinear TC (with $\epsilon_T \simeq 1$) we have to consider the total voltage $V(E)$, which reaches a minimum at $E = E_T$ (in good agreement with the predictions for the NLTC maximum, which appears at $E = \frac{3}{2}E_T$, see the main frame in Fig. 2).

To complete our study, let us estimate the order of magnitude of the main model parameters. Starting with applied electric fields E needed to observe the nonlinear field effects in granular superconductors predicted above, we notice that, according to Fig. 2, the most interesting behavior of NLTC takes place for $E \simeq E_0$. Taking $d \simeq 10$ μm and $\tau \simeq 10^{-9}$ s for typical values of the average grain size and the characteristic Josephson tunneling time (valid for conventional JJs [14] and HTS ceramics [10]), we get $E_0 = \hbar/(2ed\tau) \simeq 2 \times 10^{-2}$ V/m for the characteristic electric field (which is surprisingly lower than the typical fields needed to observe a critical current enhancement in HTS ceramics [4, 5]). On the other hand, the maximum of NLTC occurs when this field nearly perfectly matches the "intrinsic" thermoelectric field $E_T = S_0|\nabla T|$ induced by an applied thermal gradient, that is, when $E \simeq E_0 \simeq E_T$. Using $S_0 \simeq 0.5$ μV/K for the zero-field value of the linear Seebeck coefficient [10, 14], we obtain $|\nabla T|_E \simeq E_0/S_0 \simeq 4 \times 10^4$ K/m for the characteristic value of an applied thermal gradient.

Finally, taking as an example [15] granular aluminum films with phonon-dominated heat transport (with $\kappa_{ph}(T) \simeq 2 \times 10^{-7}$ W/mK at $T = T_J \simeq 0.2T_c$), let us estimate the absolute value of the zero-field electronic contribution predicted here $\kappa_e(T) \equiv \kappa_L(T, 0)$ at $T = 0.2T_c$. Recalling that within our model the scattering of normal electrons is due to the presence of the mutual inductance between the adjacent grains L_0, and using $L_0 \simeq \mu_0 d \simeq 4\pi \times 10^{-12}$ H and $V \simeq Nd^2 l$ (l is the thickness of a film), we obtain $\kappa_e(T = 0.2T_c) \simeq \beta_L(0) \times 10^{-7}$ W/mK as a rough estimate of the electronic contribution to the inductance-driven effect discussed here. Correspondingly, we get $\kappa_e(0.2T_c)/\kappa_{ph}(0.2T_c) \simeq \beta_L(0)/2$ for the ratio, where $\beta_L(0) = 2\pi I_c(0)L_0/\Phi_0$. Thus, depending mainly on the value of the critical current $I_c(0)$ and the mutual inductance between adjacent grains L_0, the thermal conductivity of specially prepared granular alumina films will be dominated by either the phonon (for small $\beta_L(0)$) or electronic (for large $\beta_L(0)$) contribution. Undoubtedly, the above estimates suggest quite a realistic possibility of observing the predicted nontrivial behavior of the thermal conductivity in granular superconductors and artificially prepared Josephson junction arrays. We hope that the results presented here will motivate further theoretical and experimental studies of this interesting problem.

REFERENCES

1. *Proceedings of the Conference "Mesoscopic and Strongly Correlated Electron Systems," Chernogolovka, 1997*, Ed. by V. F. Gantmakher and M. V. Feigel'man; Phys. Usp. **41**, 2 (1998); *Mesoscopic and Strongly Correlated Electron Systems-II*, Ed. by M. V. Feigel'man, V. V. Ryazanov, and V. B. Timofeev; Phys. Usp., Suppl. **44**, 10 (2001).
2. *Studies of High Temperature Superconductors*, Ed. by A. Narlikar and F. Araujo-Moreira (Nova Science, New York, 2001), Vol. 39.
3. L. B. Ioffe, M. V. Feigel'man, A. Ioselevich, *et al.*, Nature **415**, 503 (2002).
4. T. S. Orlova, B. I. Smirnov, and J. Y. Laval, Fiz. Tverd. Tela (St. Petersburg) **43**, 974 (2001) [Phys. Solid State **43**, 1007 (2001)].
5. T. S. Orlova, B. I. Smirnov, J. Y. Laval, *et al.*, Supercond. Sci. Technol. **12**, 356 (1999).
6. A. L. Rakhmanov and A. V. Rozhkov, Physica C (Amsterdam) **267**, 233 (1996).
7. D. Domínguez, C. Wiecko, and J. V. José, Phys. Rev. Lett. **83**, 4164 (1999).
8. J. Mannhart, Supercond. Sci. Technol. **9**, 49 (1996).
9. S. A. Sergeenkov and J. V. José, Europhys. Lett. **43**, 469 (1998).
10. S. A. Sergeenkov, Pis'ma Zh. Éksp. Teor. Fiz. **67**, 650 (1998) [JETP Lett. **67**, 680 (1998)].
11. A.-L. Eichenberger, J. Affolter, M. Willemin, *et al.*, Phys. Rev. Lett. **77**, 3905 (1996).
12. R. Meservey and B. B. Schwartz, in *Superconductivity*, Ed. by R. D. Parks (Marcel Dekker, New York, 1969), Vol. 1, p. 117.
13. L. Leylekian, M. Ocio, L. A. Gurevich, *et al.*, Zh. Éksp. Teor. Fiz. **112**, 2079 (1997) [JETP **85**, 1138 (1997)].
14. G. I. Panaitov, V. V. Ryazanov, A. V. Ustinov, *et al.*, Phys. Lett. A **100**, 301 (1984).
15. Y. Shapira and G. Deutscher, Phys. Rev. B **30**, 166 (1984); J. Deppe and J. L. Feldman, Phys. Rev. B **50**, 6479 (1994).

JETP Letters, Vol. 76, No. 3, 2002, pp. 175–179. Translated from Pis'ma v Zhurnal Éksperimental'noĭ i Teoreticheskoĭ Fiziki, Vol. 76, No. 3, 2002, pp. 209–213.

Ferromagnetic Resonance Features in Anisotropic Magnetic Films with a Metastable State of Magnetic Moment

B. A. Belyaev and A. V. Izotov

Kirenskiĭ Institute of Physics, Siberian Division, Russian Academy of Sciences, Krasnoyarsk, 660036 Russia

e-mail: belyaev@iph.krasn.ru

Received July 2, 2002

In experiments on single-domain magnetic films with uniaxial in-plane anisotropy, a new homogeneous ferromagnetic resonance peak was observed in a planar magnetic field oriented at an angle to the easy magnetization axis and directed opposite to the magnetization projection onto the field direction. The peak was observed in fields smaller than the magnetization reversal field of the film, and the origin of the peak was found to be related to the metastable state of the magnetic moment. A good agreement was obtained between phenomenological calculations and experimental data. © *2002 MAIK "Nauka/Interperiodica".*

PACS numbers: 75.70.Ak; 76.50.+g

Previous studies [1] of thin magnetic films possessing induced uniaxial in-plane anisotropy by a scanning ferromagnetic-resonance spectrometer [2] revealed a narrow peak of microwave absorption that was accompanied by an abrupt increase in the magnetic susceptibility. The peak was observed in a constant magnetic field H oriented normally to the easy magnetization axis (EMA). Its position corresponding to the uniaxial magnetic anisotropy field H_k was independent of the pumping frequency f. The peak was shown to be caused by the nonlinear static magnetic susceptibility; however, it was clearly distinguished at high and microwave frequencies. This paper describes experiments performed on permalloy films with a uniaxial magnetic anisotropy, in which an additional absorption peak was revealed in the ferromagnetic resonance spectrum. Unlike the peak of the static susceptibility, the new peak was observed in a wide range of angles between the direction of the scanning constant magnetic field and the EMA. The new peak exists in the fields $H < H_k$, and its position strongly depends on both the pumping frequency and the angle between the scanning field and the EMA.

The film samples of thickness 500 Å were fabricated by the thermal vacuum deposition of permalloy with the composition Ni_{75}–Fe_{25} characterized by a relatively small positive magnetostriction constant. The films were deposited on glass substrates 0.5 mm thick with dimensions 25×10 mm. The substrates were heated to 200°C, and the rate of deposition was 10 Å/s. The uniaxial magnetic anisotropy in the plane of a magnetic film was induced along the short side of the substrate by a constant magnetic field of 30 Oe applied during the deposition in the corresponding direction. To increase the anisotropy field, a uniaxial compression was applied to the films through a slight bending deformation of the substrate during the deposition [3]. Owing to the elastic stress, the anisotropy field in the middle of the film increased by a factor of more than 3, as compared to a stress-free sample, and reached the values $H_k > 15$ Oe. Simultaneously, the coercive force, which was measured by the magnetization reversal along the EMA, increased by almost an order of magnitude and reached the values $H_c > 4$ Oe [4]. The presence of a large anisotropy field in the samples was necessary to reduce the angular dispersion of the magnetic moment, while the increase in the coercive force (as will be shown below) was necessary to "hold" the magnetic moment of the film in the metastable state.

The experiment was performed with an automated scanning ferromagnetic resonance spectrometer [2] whose locality of measurement $S \approx 1$ mm^2 was determined by the diameter of the measuring aperture in the microwave head. The vectors of the external magnetic field H and the orthogonally oriented microwave pumping field h of frequency $f = 1.034$ GHz lay in the film plane (Fig. 1). The ferromagnetic resonance spectra were recorded within a local area of a thin magnetic film under investigation for different angles of the EMA orientation θ_n. Before each measurement run, the sample was magnetized along the EMA by the field $H =$ 300 Oe. Then, the field was reduced to zero, the required angle θ_n was set, the magnetic field direction was switched to the opposite, and, finally, two ferromagnetic resonance spectra were recorded in a given range of the scanning field. The first spectrum was recorded during the direct run of the scanning field H (the dashed lines in Fig. 2), and the second spectrum (the solid lines) was recorded after the sample magne-

0021-3640/02/7603-0175$22.00

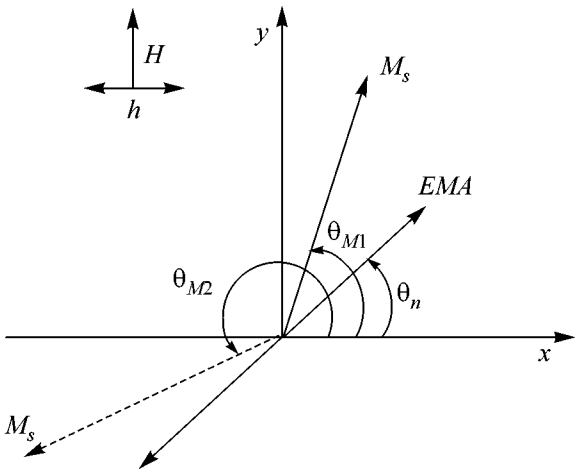

Fig. 1. Model of a magnetic film with a uniaxial anisotropy.

tization by the field H = 300 Oe without changing the angle θ_n during the reverse run.

Evidently, at the beginning of the direct run of the scanning field H, the projection of the saturation magnetization vector M_s onto the field axis (see Fig. 1) is directed opposite to the field, and, hence, the magnetic moment of the film area under investigation is in some metastable state until the magnetization reversal field of the film area under study is reached. Note that, owing to the presence of a low-frequency modulating magnetic field in the ferromagnetic resonance spectrometer [2] and the relatively small size of the film area under study, the magnetization reversal of this area occurs in a single Barkhausen jump. Therefore, the magnetization reversal field is the coercive force H_c of the given area of a thin magnetic film [4]. From Fig. 2, one can see that, at "small" angles θ_n, the amplitude of the ferromagnetic resonance signal in the stable state (i.e., ground state) is higher than in the metastable state, while at "large" angles, the situation is reversed. Note that the signal amplification factor achieved in recording the spectra for the angle θ_n = 25° was an order of magnitude greater than in the case of θ_n = 10°.

Figure 3 shows the angular dependences of the measured fields of the homogeneous ferromagnetic resonance $H_R(\theta_n)$ in the ground state of the magnetic moment (the full circles) and in the metastable state (the empty circles) for the central part of a film sample with the anisotropy field H_k = 16.6 Oe and the effective saturation magnetization M_s = 980 G. In the same figure, the empty triangles show the angular dependence of the magnetization reversal field $H_c(\theta_n)$ of the film area under study. In the case of film magnetization normal to the EMA, the magnetization reversal field almost coincides with the anisotropy field, but it rapidly decreases with an increase in θ_n. The full triangles in Fig. 3 show the measured resonance fields for the inter-

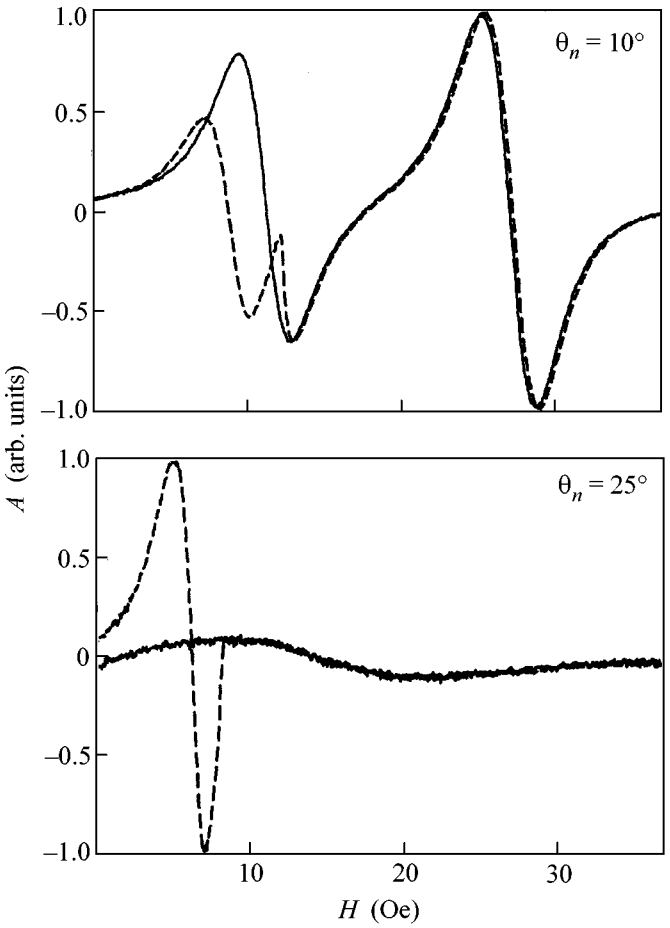

Fig. 2. Derivatives of the absorption lines for the ground state (the solid lines) and the metastable state (the dashed lines) of the magnetic moment of a thin magnetic film.

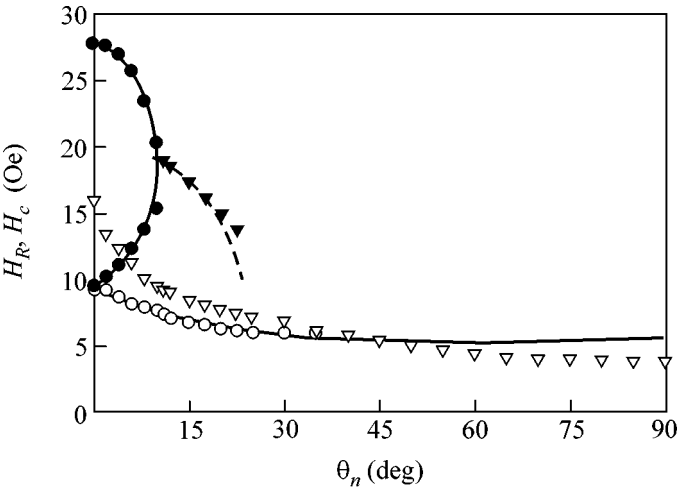

Fig. 3. Angular dependences of the resonance fields and the magnetization reversal field of a magnetic film. The dots represent the experimental data and the lines show the results of calculations (details are in the main body of the paper).

val of angles θ_n where the amplitude of the ferromagnetic resonance signal observed in the ground state of the magnetic moment is smaller than the amplitude observed in the metastable state. In this interval, an increase in θ_n is accompanied by a decrease in the resonance field and a monotone decrease in the amplitude of the ferromagnetic resonance signal, which gradually vanishes in noise. Figure 3 shows that the resonance field observed for the magnetic moment in the metastable state also monotonically decreases with increasing θ_n, but this field can be measured only when $H_c > H_R$.

To reveal the origin of the resonances observed in the experiment, we consider the model of a boundless single-domain magnetic film possessing a uniaxial in-plane magnetic anisotropy with the EMA directed at an angle θ_n to the x axis (Fig. 1). As is known, in a planar magnetic field H applied at an arbitrary angle to the EMA, when the strength of this field is lower than that of the anisotropy field H_k, two thermodynamically stable positions of the magnetic moment vector exist in the film [5]. These two states are separated by a barrier whose height is determined by the value of H_k, and the region of existence of the two states is bounded by the curve described by the cycloid equation

$$H_x^{2/3} + H_y^{2/3} = H_k^{2/3}. \quad (1)$$

Thus, in addition to the ground state of magnetization with the equilibrium angle θ_{M1} (see Fig. 1) corresponding to the absolute energy minimum, the second, metastable, position is present with the equilibrium angle θ_{M2} corresponding to the local energy minimum. This fact, in particular, gives rise to a hysteresis and makes it possible to observe a ferromagnetic resonance for the two aforementioned states.

For the thin magnetic film model shown in Fig. 1, by solving the Landau–Lifshits equation in the absence of damping, it is easy to obtain (e.g., following [6]) the expression for the eigenfrequency of the magnetization precession ω_0;

$$\omega_0^2 = \Omega_1\Omega_2, \quad (2)$$

where

$$\Omega_1 = \gamma[H\sin(\theta_M) + H_k\cos^2(\theta_n - \theta_M) + 4\pi M_S];$$

$$\Omega_2 = \gamma[H\sin(\theta_M) + H_k\cos 2(\theta_n - \theta_M)];$$

γ is the gyromagnetic ratio; and the equilibrium angle θ_M for the magnetization vector M_s is determined from the equation

$$H\cos(\theta_M) + \frac{1}{2}H_k\sin 2(\theta_n - \theta_M) = 0, \quad (3)$$

which is obtained from the condition of the minimal free energy density of the film, including the Zeeman energy, the anisotropy energy, and the energy of demagnetizing fields. Equation (3), depending on the magnetic field strength and the orientation of the EMA, yields either one value of the equilibrium angle θ_M or two different values corresponding to the ground and metastable states of the magnetization vector.

In Fig. 3, the solid lines show the angular dependences of the resonance field that were obtained from Eqs. (2) and (3) for both states of the magnetic moment of the film under study. One can see a good agreement between theory and experiment for both ground state and metastable states. However, the formulas obtained above do not describe the angular dependence of the peak position observed in the experiment for $\theta_n > 10°$ (the full triangles in Fig. 3). The origin of this peak can be explained by the field dependence of the component χ_{xx} of the dynamic magnetic susceptibility tensor. For the film model under consideration (see Fig. 1), this component is easily calculated by solving the Landau–Lifshits equation with the damping parameter α involved in the dissipative term in the Hilbert form:

$$\chi_{xx} = \frac{\gamma M_s(\Omega_1 + i\alpha\omega)\sin^2\theta_M}{\omega_0^2 - (1+\alpha^2)\omega^2 + i\alpha\omega(\Omega_1 + \Omega_2)}. \quad (4)$$

Separating this component into the real and imaginary parts and setting $\alpha^2 \ll 1$, we obtain

$$\chi_{xx} = \chi'_{xx} + i\chi''_{xx}, \quad (5)$$

$$\chi'_{xx} = \frac{\gamma M_s[\Omega_1(\omega_0^2 - \omega^2) + \alpha^2\omega^2(\Omega_1 + \Omega_2)]\sin^2\theta_M}{[(\omega_0^2 - \omega^2)^2 + \alpha^2\omega^2(\Omega_1 + \Omega_2)^2]}, \quad (6)$$

$$\chi''_{xx} = \frac{\gamma M_s\alpha\omega(\Omega_1^2 + \omega^2)\sin^2\theta_M}{[(\omega_0^2 - \omega^2)^2 + \alpha^2\omega^2(\Omega_1 + \Omega_2)^2]}. \quad (7)$$

Evidently, the change in the electromagnetic energy absorption in the magnetic film during the magnetic field scan is determined by the field dependence of the quantity χ''_{xx} with the absorption maxima corresponding to the conditions $d\chi''_{xx}/dH = 0$ and $d^2\chi''_{xx}/dH^2 < 0$. It can be easily shown that, in addition to the main absorption maxima observed at the ferromagnetic resonance in the fields H_R when the pumping frequency is $\omega = \omega_0$, one more maximum is observed in the field where the condition

$$\frac{d}{dH}(\Omega_1\Omega_2) = 0 \quad (8)$$

is satisfied. The angular dependence of the position of this maximum was calculated from Eq. (7) for the pumping frequency used in the measurements (f = 1.034 GHz). This dependence is shown in Fig. 3 by the dashed line and, as one can see, it also agrees well with the experiment.

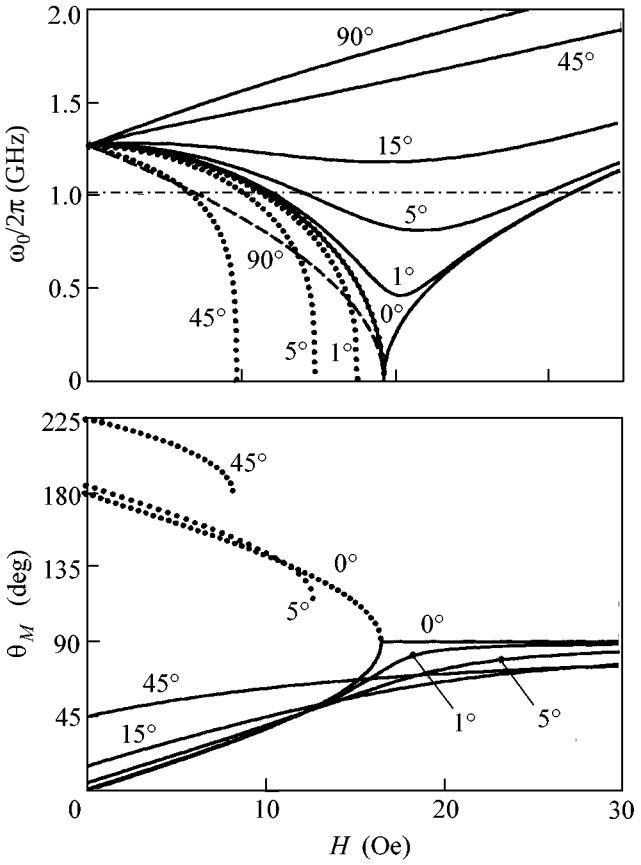

Fig. 4. Field dependences of the ferromagnetic resonance frequency and the equilibrium angle of magnetization for several directions of the easy magnetization axis. The solid lines correspond to the ground state of the magnetic moment and the dotted and dashed lines correspond to the metastable state.

The additional susceptibility maximum can be observed only in a limited range of variation of the angle θ_n, and calculations show that the lower bound of this range is determined by the pumping frequency and tends to zero when $\omega \longrightarrow 0$. It should be noted that the susceptibility peak revealed in our experiment exists only when the pumping frequency satisfies the condition $\omega < \omega_0$. Therefore, this peak cannot be considered as a ferromagnetic resonance. In fact, this peak characterizes the microwave absorption that occurs in the magnetic film when the ferromagnetic resonance frequency approaches the pumping frequency in the course of the field scan and then moves away from it.

These conclusions are supported by the computational results shown in Fig. 4. The upper part of this figure presents the eigenfrequencies of homogeneous oscillations of magnetization in the magnetic film model under study as functions of the constant magnetic field. These dependences were calculated by Eq. (2) for different directions of the EMA. The solid lines show the ferromagnetic resonance frequencies for the ground state, and the dotted and dashed lines, for the metastable state. In the calculations, we used the parameters presented above for the magnetic film area under investigation. The horizontal dot-and-dash line indicates the pumping frequency used in the measurements. One can see that, owing to the nonmonotonic dependence $\omega_0(H)$ observed at certain angles, e.g., at $\theta_n = 15°$, the resonance frequency first approaches the pumping frequency and then moves away from it during the field scan. Therefore, the position of the maximum in the field dependence of the microwave absorption by the film coincides with the position of the minimum in the dependence $\omega_0(H)$ [see Eqs. (2) and (8)].

It was found that, for the frequency $\theta_n = 0$, as the angle θ_n increases, the ferromagnetic resonance field H_R for the metastable state of the magnetic moment of the film first decreases reaching its minimal value $H_R = H_k/2$ at $\theta_n = 45°$ (see Fig. 4) and then increases to the maximal value $H_R = H_k$. Note that, when $\theta_n = 0$, the ferromagnetic resonance frequencies for the metastable and ground states observed in the fields $H < H_k$ fully coincide. The lower part of Fig. 4 shows the field dependences of the equilibrium orientation angles of the saturation magnetization. The curves were obtained by Eq. (3) for several values of θ_n. As one would expect, these dependences prove to be noticeably different for the ground state (the solid lines) and for the metastable state (the dotted lines).

Thus, on specially prepared samples of thin magnetic films, we observed a ferromagnetic resonance in a specific metastable state of the magnetic moment. We studied the dispersion dependences of the ferromagnetic resonance field in the phenomenological approximation and obtained a good agreement between theory and experiment. We showed that, in the metastable state, the ferromagnetic resonance field can be measured only in conditions when this field is smaller than the field of magnetization reversal of the magnetic film sample under study. In other words, the effect revealed in our experiments can be observed in films with a sufficiently high coercive force.

In addition, we have found that the microwave absorption peaks observed in the experiment for the ground state of the film in a certain interval of angles of the EMA orientation result from the nonmonotonic dispersion dependence of the ferromagnetic resonance field. Despite the fact that, in the spectrum records, these peaks manifest themselves as ferromagnetic resonances, they are observed at frequencies below the ferromagnetic resonance frequencies and, hence, are of different origin. Namely, in this case, the change in the microwave absorption observed during the magnetic field scan is caused by the approach of the resonance frequency to the pumping frequency and its subsequent change in the opposite direction. The width of these absorption peaks is much greater than the width of the ferromagnetic resonance line. In principle, such peaks

can be observed in any materials, including massive ones, in which a nonmonotonic behavior of the frequency dispersion of the resonance field takes place.

REFERENCES

1. B. A. Belyaev, A. V. Izotov, and S. Ya. Kiparisov, Pis'ma Zh. Éksp. Teor. Fiz. **74**, 248 (2001) [JETP Lett. **74**, 226 (2001)].
2. B. A. Belyaev, A. A. Leksikov, I. Ya. Makievskiĭ, and V. V. Tyurnev, Prib. Tekh. Éksp., No. 3, 106 (1997).
3. B. A. Belyaev, A. G. Vladimirov, and V. V. Polyakov, in *Proceedings of the XVI International School-Workshop "Novel Magnetic Materials for Microelectronics," Moscow, 1998*, Part 1, p. 329.
4. B. A. Belyaev, A. V. Izotov, and A. A. Leksikov, Zavod. Lab. **67** (9), 23 (2001).
5. L. D. Landau and E. M. Lifshitz, *Course of Theoretical Physics*, Vol. 8: *Electrodynamics of Continuous Media* (Nauka, Moscow, 1982; Pergamon, New York, 1984).
6. A. G. Gurevich, *Magnetic Resonance in Ferrites and Antiferromagnets* (Nauka, Moscow, 1973), pp. 79–89.

Translated by E. Golyamina

JETP Letters, Vol. 76, No. 3, 2002, pp. 180–184. Translated from Pis'ma v Zhurnal Éksperimental'noĭ i Teoreticheskoĭ Fiziki, Vol. 76, No. 3, 2002, pp. 214–218.

Phase Transition in a Vortice Lattice in a Bi2212:Pb Single Crystal

L. S. Uspenskaya*, A. B. Kulakov*, and A. L. Rakhmanov**

* *Institute of Solid State Physics, Russian Academy of Sciences, Chernogolovka, Moscow region, 142432 Russia*
e-mail: uspenska@issp.ac.ru

** *Institute of Theoretical and Applied Electrodynamics, Russian Academy of Sciences, Moscow, 125412 Russia*

Received July 10, 2002

The magnetooptical method was used to investigate the penetration of a magnetic flux into a single crystal of a high-temperature superconductor $(Bi_{0.84}Pb_{0.16})_{2.2}Sr_2CaCu_2O_8$ in crossed magnetic fields. It is shown that at low temperatures the penetration of the magnetic flux is anisotropic: the flux moves preferentially along the magnetic field applied in the plane of the sample, and the anisotropy grows as the temperature increases. At a temperature $T_m = 54 \pm 2$ K, there occurs a sharp change in the character of penetration of the magnetic field into the superconductor; the direction of the flux ceases be dependent on the direction and magnitude of the magnetic field applied in the plane of the sample. In this case, the transition temperature T_m is independent of the applied magnetic field. The effect is interpreted in terms of the concepts of a phase transition in the system of vortices, which is related to a sharp decrease in the correlations in the position of vortices in various CuO planes, i.e., with the transition from three-dimensional to two-dimensional behavior of the vortex structure. © *2002 MAIK "Nauka/Interperiodica".*

PACS numbers: 74.25.Dw; 74.60.-w; 74.72.Hs

The dynamics of a magnetic flux in high-temperature superconductors (HTSCs) with a high anisotropy and in isotropic or weakly anisotropic superconductors can differ markedly [1, 2]. The differences are clearly seen in magnetooptical observations of the penetration of a magnetic flux into a superconductor in crossed magnetic fields [3]. Thus, magnetooptical images demonstrate a strong effect of the longitudinal (applied in the plane *ab*) magnetic field $\mathbf{H_{ab}}$ on the penetration and distribution of the transverse (oriented along the *c* axis) magnetic flux in HTSCs such as YBCO. At the same time, in layered systems with a strong anisotropy (e.g., Bi2212), the penetration of the magnetic flux oriented along the *c* axis is independent of the intensity and direction of $\mathbf{H_{ab}}$. Such a difference in the penetration of the magnetic flux is due to the fact that the magnetic flux penetrates into superconductors with a weak anisotropy in the form of three-dimensional Abrikosov vortices, whereas into the layered HTSCs it penetrates in the form of two-dimensional vortices with a weak coupling between the vortices located in different CuO planes [3].

The problem of the existence of a transition between the two above-described types of magnetic structures and the nature of this transition has been discussed in the literature for more than a decade [1]. To observe this transition by the magnetooptical method, it is natural to use single crystals with an anisotropy that is greater than that in the 1-2-3-type systems but lower than that in Bi2212. As is known [4], doping Bi2212 with lead decreases the anisotropy of the superconducting properties, and the single crystals of the HTSC Bi222:Pb are suitable candidates for such an investigation.

In this work, we used the magnetooptical method to study the penetration of a perpendicular magnetic field B_z into single-crystal plates of the HTSC Bi222:Pb placed in a longitudinal magnetic field. It is shown that at temperatures below $T_m = 54 \pm 2$ K the transverse field penetrates into the plate chiefly in the direction of the applied longitudinal field $\mathbf{H_{ab}}$. At a temperature $T = T_m$, there occurs a sharp change in the character of penetration of the magnetic flux: the direction of its motion ceases be dependent on $\mathbf{H_{ab}}$. It is also shown that at temperatures $T < T_m$ the anisotropy of penetration of the transverse flux increases with increasing temperature and field $\mathbf{H_{ab}}$.

The single crystals of $(Bi_{0.84}Pb_{0.16})_{2.2}Sr_2CaCu_2O_{8+\delta}$ were grown from a solution in the melt using a seed grown from the same melt. The critical temperature of the transition ($T_c \approx 91$ K) and the width of the superconducting transition ($\Delta T_c \approx 1$ K) were determined by the inductive technique. The preparation of the samples was described in detail in [5]. Prior to measurements, the samples were polished chemically in ethylenediaminetetraacetic acid. A flat single crystal was obtained with a shape close to a triangle with a long side (3.4 mm) oriented along the diagonal between the planes *ac* and *ab* and a side equal to 2.4 mm coinciding with the *ac* plane. The thickness of the sample was approximately 70 μm. The microstructure of the single

crystal was studied by X-ray topography (angular scanning method). Defects that are typical of the Bi2212:Pb crystals were detected: a twin structure (twins located in the *ab* plane almost perpendicular to the long side of the single crystal) and a lamellar structure (lamellae parallel to the *ac* plane and one of the sides of the single crystal).

Magnetooptical measurements were performed in a temperature range from 12 K to T_c. The magnetic field H_z parallel to the *c* axis was generated by a solenoidal coil and could be varied from 0 to ±1200 Oe. The dc field $\mathbf{H_{ab}}$ was produced by Helmholtz coils with a special core that ensured a field uniformity of about 1% in the site where the sample was placed. The field $\mathbf{H_{ab}}$ was varied from 0 to 1800 Oe and could be rotated in any direction. Both regimes, the cooling of the sample in the field $\mathbf{H_{ab}}$ from a temperature above T_c (FC) and the magnetization of the sample in the field $\mathbf{H_{ab}}$ at the temperature of observation (ZFC) were used in the experiments.

The distributions of the transverse component of the magnetic field B_z were studied using a standard magnetooptical method described in [6]. As the indicator of the magnetic field, we used a garnet film with an in-plane anisotropy of 2000 Oe, which permitted us to perform observations in sufficiently high magnetic fields. Using the magnetooptical patterns obtained with the help of a digital camera with a fixed sensitivity, we constructed profiles of the distribution of the magnetic flux along various directions. The calibration of the image brightness corresponding to given magnitudes of a magnetic field was performed at the same camera sensitivity at $T > T_c$ (in the temperature range 12–150 K, the sensitivity of the indicator film remained unaltered).

Figure 1a displays a typical picture of the penetration of the transverse magnetic flux at $\mathbf{H_{ab}} = 0$. Such behavior of the magnetic flux was observed over the whole temperature range from 12 to 54 K. Note that the magnetic field begins penetrating into the sample in those sites where twins enter onto the edge of the crystal. This effect is observed at all temperatures $T < 54$ K and is reproduced upon repeated measurements. The distribution of the magnetic flux at $T < 54$ K was settled in in times of 1 to 3 min, after which it remained almost unaltered. At temperatures above 54 ± 2 K, the picture of the penetration of the field sharply changes. The flux begins to penetrate through a weak site and occupies the whole sample in a time less than 1 s, as is usually observed in Bi2212 single crystals that have not been doped with lead [3]. At $T < 54$ K, we recorded the profiles of magnetic induction $B_z(r)$ near the weak site in various directions to the edge of the crystal. The profile consists of two regions of characteristics. Near the center of the volume occupied by the magnetic flux, the distribution of the field only weakly changes in space. At the periphery of the spot, there exists a region in which there occurs a sharp and almost linear decrease

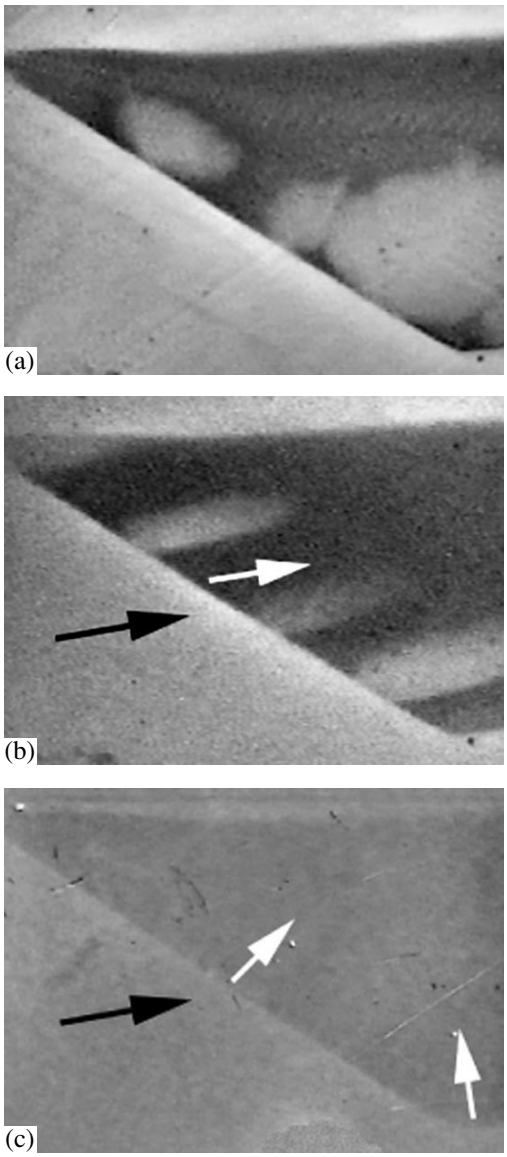

Fig. 1. Penetration of perpendicular magnetic flux into the sample: (a) $H_{ab} = 0$, $H_z = 60$ Oe, and $T = 30$ K; (b) $H_{ab} = 1800$ Oe, $H_z = 60$ Oe, and $T = 30$ K; and (c) $H_{ab} = 1800$ Oe, $H_z = 60$ Oe, and $T = 56$ K. Arrows show the directions of the applied field and motion of the magnetic flux.

in $B_z(r)$. The profiles of the magnetic flux depend on the angle, and the spot of the ingoing flux has a maximum size approximately along the laminar structure. The ratio k_J of the maximum magnitude of $\partial B_z/\partial r$ to the minimum one does not exceed 2.

Figure 1b shows a typical picture of the penetration of the magnetic flux into the sample after cooling in a magnetic field H_{ab} (FC mode) at $T < 54$ K. It can be seen from Fig. 1b that the magnetic flux chiefly propagates along the direction $\mathbf{H_{ab}}$, which is shown by an arrow. Such a picture of the penetration of the magnetic field

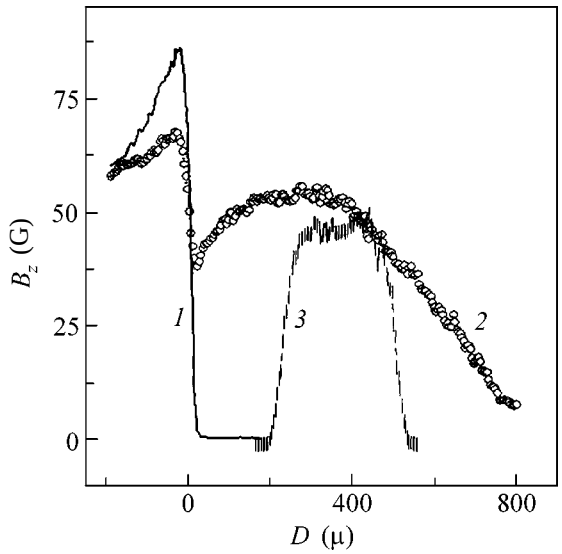

Fig. 2. Profiles of the perpendicular magnetic field in the sample at H_{ab} = 650 Oe, H_z = 60 Oe, and T = 36 K. Profile *1* was recorded in the direction H_{ab} between weak sites; profile *2*, in the same direction in the band corresponding to the penetration of the magnetic flux; profile *3*, in the same band in the direction perpendicular to H_{ab} near the maximum of B_z.

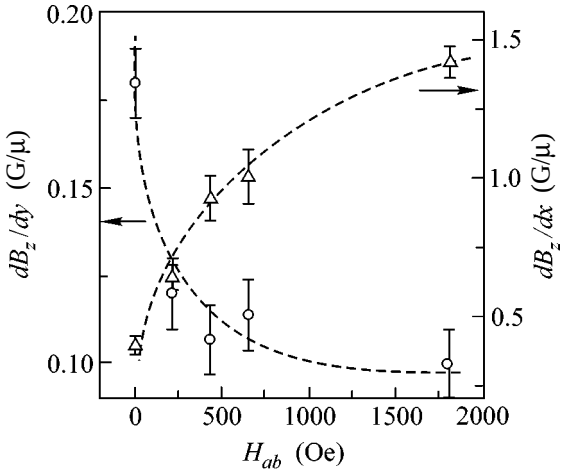

Fig. 3. Dependences of $\partial B_z/\partial x$ and $\partial B_z/\partial y$ on H_{ab} at T = 36 K.

is observed in the temperature range from 12 to 54 K. Note that such a mode of the penetration of the magnetic field is analogous to that observed for single crystals of YBCO [3]. The anisotropy of the penetration of the magnetic flux is larger, the higher the intensity of H_{ab}.

If the temperature exceeds T_m, then, as in the case where H_{ab} = 0, the picture of the penetration of the flux changes sharply (Fig. 1c). The magnetic field penetrates through weak sites and rapidly occupies the entire sample. In this case, the direction of motion of the flux is independent of the direction of the magnetic field $\mathbf{H_{ab}}$ (see arrows in Fig. 1c). Note that in the range of fields studied (H_{ab} = 0–1800 Oe and H_z = 0–300 Oe), the temperature of the crossover $T_m = 54 \pm 2$ K remains unaltered.

Figure 2 displays three profiles of the magnetic field. Profile *1* was recorded in the direction of the field $\mathbf{H_{ab}}$ (x axis) between weak sites, where the penetration of the magnetic flux is screened by the Meissner current. Profile *2* was recorded in the same direction but in the band corresponding to the penetration of the magnetic flux near a weak site. Here, a slight dip caused by the Meissner current can also be seen. In the bulk of the sample, the profile of the penetrating magnetic field has a variable slope similar to that observed at H_{ab} = 0. Profile *3* was recorded in the same band of the penetrating magnetic flux but in the direction perpendicular to the applied magnetic field (y axis) near the maximum of B_z. This profile also consists of a slowly sloping part and two peripheral regions with sharp (almost linear) slopes. The peripheral slope $\partial B_z/\partial y$ is significantly greater than $\partial B_z/\partial x$. The dependences of the derivatives $\partial B_z/\partial x$ and $\partial B_z/\partial y$ on H_{ab} are shown in Fig. 3. It is seen that the screening currents along the x axis increase with increasing magnetic field, whereas the currents along the y axis decrease. Both these currents decrease with temperature. However, their ratio $k_J = (\partial B_z/\partial y)/(\partial B_z/\partial x)$ increases with temperature, saturating at T = 25–30 K. The $k_J(T)$ curve is shown in Fig. 4. The picture of the penetration of the magnetic flux is almost the same in the FC and ZFC regimes.

The anisotropy of the penetration of the magnetic flux into superconductors in crossed magnetic fields has been studied in much detail [3, 7, 8]. Upon the motion perpendicular to the field $\mathbf{H_{ab}}$, the screening currents are directed along $\mathbf{H_{ab}}$ (force-free configuration). Upon the motion of vortices along $\mathbf{H_{ab}}$, the screening currents flow perpendicular to $\mathbf{H_{ab}}$ (force configuration). The density of the screening currents in the case of the force-free configuration is greater; this leads to a preferential propagation of the magnetic flux along the applied field. Moreover, if during the motion the transverse vortices intersect vortices that are located in the *ab* plane, then the cores of the latter are additional centers of pinning that hinder transverse motion and only slightly affect the longitudinal motion. With increasing temperature, the density of the screening currents decreases, as was observed in our experiments as well, but the anisotropy of penetration increases for YBCO because of the increase in the coherency length ξ_c and a corresponding increase in the interplane correlation of the order parameter. Such an increase is also observed in our experiments (Fig. 4). In the force-free configuration, the screening currents increase with

increasing magnetic field; the effective pinning also increases with increasing H_{ab}. Correspondingly, $\partial B_z/\partial y$ increases with H_{ab}. Thus, the results of our observations at $T < T_m$ are qualitatively similar to analogous results for HTSCs of the YBCO type and can be explained in a natural manner in terms of the concepts of vortices with a strong interplane correlation (a 3D-type vortex structure).

The disappearance of coupling between longitudinal and transverse magnetizations in HTSCs with a strong anisotropy is ascribed to the disappearance of correlation between two-dimensional (2D) vortices located in different CuO planes [3, 8]. The magnetic flux produced by the field H_{ab} is concentrated between these planes and the currents that screen the transverse flux flow in the CuO layers. It is obvious that no effective interaction between the longitudinal and transverse magnetic fluxes exists in this case. It is natural that, upon the transition into the phase of uncorrelated 2D vortices, the creep of the flux increases, the efficiency of pinning at defects decreases, and, correspondingly, the density of screening currents decreases as well [2]. Thus, it is natural to ascribe the transition observed at $T = T_m$ to the transition into the phase of uncorrelated 2D vortices. The parameter that characterizes the anisotropy of penetration of the magnetic flux, k_J, increases with temperature, saturates, and then the character of penetration changes discontinuously. Such behavior speaks in favor of a phase transition of the melting type, which was repeatedly discussed for strongly anisotropic HTSCs [1, 2]. Indeed, with increasing temperature, the interplane correlation of the order parameter first increases due to the growth of $\xi_c(T)$; then, thermal fluctuations begin to compete with them, the $k_J(T)$ dependence saturates, and a phase transition occurs.

In such a phase transition, the vortex lattice melts and the columnar structure of isolated vortices disappears [1, 2]. The transition temperature may be estimated from the relation $k_B T_m = a_L C_{66} a_0^2 d_c$ where $a_L \ll 1$ is the Lindemann constant, C_{66} is the shear modulus of the vortex lattice, a_0 is the lattice parameter of the vortex lattice, and d_c is the effective correlation length of vortices along the c axis. For 3D systems, $d_c \sim a_0(C_{44}/C_{66})^{1/2}$, where C_{44} is the flexural modulus of the vortex lattice. For multilayered structures with Josephson coupling between layers, d_c is equal to the thickness of the corresponding superconducting layer. Since in the main approximation we have $C_{66} \propto B$, $C_{44} \propto B^2$, and $a_0 \propto 1/\sqrt{B}$ [1, 2], then d_c and, consequently, T_m are independent of the magnetic field in both the first and second cases, which agrees with our measurements. In the theory of dislocation melting, it is assumed that $a_L = 1/4\pi$. Then, substituting the corresponding values of

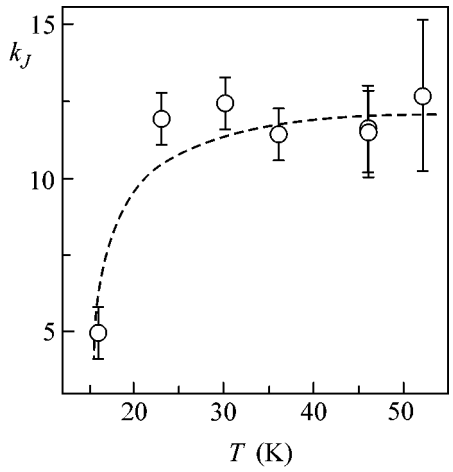

Fig. 4. Temperature dependence $k_J(T)$ at H_{ab} = 1800 Oe.

C_{66} and a_0 into the expression for T_m, we obtain [1]

$$k_B T_m = \phi_0^2 d_c/32\sqrt{3}\pi^2\lambda_{ab}^2(T_m), \quad (1)$$

where ϕ_0 is the quantum of the magnetic flux and λ_{ab} is the London penetration depth in the ab plane. For the estimation, we assume that $\lambda_{ab}(0)$ = 300 nm. Then, we obtain from Eq. (1) that $T_m \sim 50$ K if $d_c \sim$ 1–1.5 nm, which is close to the distance between the CuO planes in the crystal lattice of Bi2212:Pb [4, 5].

The anisotropy parameter $\Gamma = \xi_{ab}/\xi_c$ of Bi2212:Pb is much larger than that of YBCO [4]. It is natural to suppose that for YBCO the parameter d_c characterizing the interplanar correlation of vortices along the c axis also is larger. Then, according to Eq. (1), the transition point T_m for YBCO corresponds to higher temperatures than in the case of Bi2212:Pb and it is even possible that $T_m > T_c$. At the same time, the anisotropy of Bi2212 is much larger than that of Bi2212:Pb [4]. Then, the value of d_c in Bi2212 is smaller than that in Bi2212:Pb and, correspondingly, the transition point T_m is shifted toward lower temperatures. We can suppose that it is for these reasons that the magnetooptical observations do not reveal the phase transition in these systems. In some works (see [9] and references therein), the transition of the type of melting of a vortex lattice is attributed to specific features of the variation of the resistance and magnetic moment, which are observed, e.g., in Bi2212 single crystals in a temperature range from 45 to 85 K. In this case, the transition temperature substantially depends on the magnetic field. However, similar effects cannot represent direct evidence in favor of the disappearance of three-dimensional correlations in the system of vortices. Possibly, they are due to the change in the mode of pinning [10]. At the same time, magnetooptical measurements in crossed fields appear to be more direct evidence for the development of a phase transition of the 3D–2D type in the vortex system.

We are grateful to M.V. Indenbom, V.V. Ryazanov, L.M. Fisher, I.F. Voloshin, A.V. Kalinov, and I.K. Bdikin for fruitful discussions. This work was supported in part by the INTAS (project no. 02-2282), the Russian Foundation for Basic Research (project nos. 02-02-17062 and 00-02-18032), and the Russian Program on Superconductivity (contract no. 40.012.1.1.11.46).

REFERENCES

1. D. Feinberg, J. Phys. III **4**, 169 (1994).
2. G. Blatter, M. V. Feigel'man, V. B. Geshkenbein, *et al.*, Rev. Mod. Phys. **66**, 1125 (1994).
3. M. V. Indenbom, A. Forkl, B. Ludescher, *et al.*, Physica C (Amsterdam) **209**, 259 (1993).
4. T. Motohashi, Y. Nakayama, T. Fujita, *et al.*, Phys. Rev. B **59**, 14080 (1999).
5. A. B. Kulakov, I. K. Bdikin, S. A. Zver'kov, *et al.*, Physica C (Amsterdam) **371**, 45 (2002).
6. L. A. Dorosinskii, M. V. Indenbom, V. I. Nikitenko, *et al.*, Physica C (Amsterdam) **203**, 149 (1992).
7. E. H. Brandt, Phys. Rev. Lett. **68**, 3769 (1992).
8. P. H. Kes, J. Aarts, V. M. Vinokur, *et al.*, Phys. Rev. Lett. **64**, 1063 (1990).
9. D. T. Fuchs, E. Zeldov, D. Majer, *et al.*, Phys. Rev. B **54**, R796 (1996).
10. M. Baziljevich, D. Giller, M. McElfresh, *et al.*, Phys. Rev. B **62**, 4058 (2000).

Translated by S. Gorin

JETP Letters, Vol. 76, No. 3, 2002, pp. 185–188. Translated from Pis'ma v Zhurnal Éksperimental'noĭ i Teoreticheskoĭ Fiziki, Vol. 76, No. 3, 2002, pp. 219–222.

Possible Mechanism of Superconductivity in the CuO–Cu Interface

I. I. Amelin

Mordovian State University, Saransk, 430000 Russia

Received May 13, 2002; in final form, July 8, 2002

Apparently, a two-dimensional CuO lattice is formed on the surface of copper oxide in the CuO–Cu interface. This lattice consists of Cu^{2+} and O^{1-} ions, which form a narrow, partially filled two-dimensional band. In this case, local electron pairs (LEPs) can form in the oxygen subsystem as a result of the fulfillment of the Shubin–Vonsovskii conditions. A crude estimate of the formation temperature of LEPs gives $T^* \sim 10^4$ K. At the concentration in the interface layer $n \sim 1.6 \times 10^{20}$ cm^{-3} and the effective mass of carriers $m^* \sim m_e$, the onset temperature of Bose–Einstein condensation may take a value of $T_c \sim 1000$ K. The estimate obtained for the temperature T_c corresponds to the experimental value by an order of magnitude. © *2002 MAIK "Nauka/Interperiodica".*

PACS numbers: 74.80.Dm; 74.20.-z

The temperature dependence of the electrical conductivity and the current–voltage characteristics of Cu films deposited by thermal evaporation on natural faces CuO single crystals as a substrate were investigated in [1]. It was shown that the electrical conductivity of Cu films measured in the film plane increases in some samples after electrothermal annealing by a factor of several tens, several hundreds, or even more than 150 hundred. The results obtained are explained by the formation of a layer in the CuO–Cu interface with an electrical conductivity that significantly exceeds the electrical conductivity of copper. It was suggested that the high electrical conductivity of the layer can be explained by the formation of some regions in this layer that possess high-T_c superconductivity with a critical temperature T_c that significantly exceeds 400 K. The nature of the high electrical conductivity of the layer is presently unclear. The experimental estimate of 2Δ, where Δ is the band gap, comprises 120 mV, and the estimate of the temperature is $T_c \approx 800$–1100 K [2]. The complicated character of the temperature dependence of the magnetic susceptibility in nanocrystalline samples of the low-dimensional CuO antiferromagnet is explained by the presence of paramagnetic Cu^{2+} ions. The Cu^{2+} ions localized in the surface layers of nanocrystals are noninteracting and behave as a paramagnetic impurity because of the loss of 3D periodicity and the breaking of exchange coupling. The importance of the surface states of Cu ions increases as the crystallite size decreases. From the given experimental facts, it can be inferred that a two-dimensional lattice is likely formed on the CuO surface, in which the Cu^{2+} and O^{2-} ions form a narrow two-dimensional band.

It was found experimentally [4] that localized superconductivity with high T_c is observed only in such copper–oxide systems that exhibit a paramagnetic character of the temperature dependence of magnetic susceptibility. The presence of an impurity paramagnetic phase (or fragments) in antiferromagnetic copper oxide is a necessary condition for the occurrence of impurity localized superconductivity with high T_c. Strong spin correlations and antiferromagnetic order, for example, in monoclinic CuO prevent the occurrence of superconductivity.

An increase in electrical conductivity by six to seven orders of magnitude is observed in $Mg_{1-x}Cu_xO$ systems at $x = 0.15$–0.20, which may indicate that Cu^{2+} ions are acceptors with a comparatively small activation energy, that is, are located relatively close to the top of the oxygen valence band (according to the sign of the thermoelectric coefficient, the charge carriers in $Mg_{1-x}Cu_xO$ are holes). Another characteristic property of electrical conduction in $Mg_{1-x}Cu_xO$ is the occurrence of electrical instabilities observed in some samples, namely, sharp drops in electrical resistance at 230–270 K. Such instabilities may point to the existence of a superconducting impurity in the samples. The authors of [4] came to the conclusion that a localized superconducting layer of the interface type forms in the layer of $Mg_{1-x}Cu_xO$ contacting copper. Thus, the $Mg_{1-x}Cu_xO$ solid solutions ($0 \le x \le 0.20$) with the NaCl crystal structure studied in the temperature range 5–550 K are paramagnetic semiconductors of the *p*-type. Evidently, a two-dimensional lattice composed of Cu^{2+} and O^{2-} ions, which form a narrow two-dimensional band, is formed in this substance on the surface as well.

0021-3640/02/7603-0185$22.00

When Cu atoms are deposited on this surface, electrons will be transferred from O^{2-} anions of the two-dimensional layer to Cu atoms. The Cu atoms near the surface will tend to the $3d^{10}4s^2$ state. This excludes the participation of the deposited Cu atoms in superconductivity. In support of the transfer of electron density, ionization potentials of atoms and anions can be considered. The ionization potentials of Cu and O are, respectively, 7.72 and 13.62 eV [5]. However, the ionization potential of the O^{1-} anion is already equal to 3.55 eV, whereas the ionization potential of the O^{2-} anion equals approximately zero. The transfer of electron density will proceed until the *p* and *d* energies of the O^{1-} and Cu^{1-} anions become equal. Because copper at the CuO surface occurs in the paramagnetic Cu^{2+} state at high temperatures at which a superconducting state is observed, the Cu^{2+} ions of the 2D plane will indirectly participate in the formation of the superconducting state. Evidently, oxygen anions have a dominant role in the formation of the superconducting state. Thus, the Cu–CuO interface will apparently contain a 2D CuO lattice composed of Cu^{2+} and O^{1-} ions, which form a narrow, partially filled 2D band. In this case, local electron pairs (LEPs) can form in the plane in the oxygen subsystem as a consequence of the fulfillment of the Shubin–Vonsovskii conditions. The states of Cu ions deposited on the CuO surface are located near the Fermi level of the 2D lattice, which, evidently, will allow LEPs to move along the surface and to form a superconducting Bose–Einstein condensate with high T_c.

Shubin and Vonsovskii showed [6] that, if the condition

$$ZV > I, \tag{1}$$

where *Z* is the number of the nearest neighbors, *I* is the energy of electrostatic interaction between two collectivized (former valence) electrons on one crystal lattice site, and *V* is the energy of electrostatic interaction between two collectivized electrons of two neighboring lattice sites, is fulfilled in a narrow half-filled metallic band with one electron per site, a polar state arises (referred to in the literature as a charge-density-wave (CDW) state) with the order parameter $m = 2$. The parameter *m* equals the difference in electron density on neighboring sites. The value $m = 2$ corresponds to the formation of LEPs in the system. It was shown in [7] that condition (1) is fulfilled in the CuO_2 planes of the $YBa_2Cu_3O_7$ crystal. These conditions are the reason for the formation of CDW in the anionic *p* subsystem. In this approximation, the maximum formation temperature of LEPs is estimated by the value $T^* \approx 150$ K. In the proposed model of the formation of a high-T_c superconducting state, given an insignificant increase in the number of holes t_1 and a decrease in the number of holes *t* in the *p* and *d* states of the Cu and O ions of the CuO_2 planes, the temperature T^* is bell shaped and corresponds to the experimental dependence $T_c(\delta)$ of the $YBa_2Cu_3O_{6+\delta}$ crystal. Based on the given mechanism of electron pairing, recommendations were given in [8, 9] on obtaining high-T_c superconductors containing carbon, nitrogen, and oxygen anions. Such substances should have partially filled A^K anion states near the Fermi level of a not-too-wide hybridized conduction band (about 1 eV) with a sufficiently large concentration of carriers. These substances should have superconducting monolayers (planes) of anions A and metal ions with more strongly open valence shells as compared with the Cu ions and O anions of the CuO_2 planes in the high-T_c superconductor. In this case, it is possible that there exist the parameters $t_1 = 1$ and $t = 1$, and hence T^* assumes a large value compared to T^* in cuprate high-T_c superconductors [7]. The second necessary condition of the occurrence of LEPs and the superconducting state in new high-T_c superconductors is the existence of a narrow conduction band in these materials. This can be achieved only in deposited monolayers (planes), in which the A^{K-} anions should have a small number of closest neighbors. In order to create partially filled states of A^{K-} anions near the Fermi level, the superconducting layers should be surrounded by layers of carbon, oxides, or metals with high electronegativity. The case in point is the creation of substances that are similar in structure with layered high-T_c superconductors. Evidently, the conditions listed above are fulfilled in the Cu–CuO interface.

The value of T^* of the surface layer of CuO can be estimated as follows. The CuO oxide belongs to the tenorite structure type, which represents a monoclinically distorted type of the NaCl structure. The lattice cell parameters are $a = 4.684$, $b = 3.425$, $c = 5.129$ Å, and $\beta = 99.46°$ [10]. The interatomic distances in the *xy* plane will be equal to $R_x = 2.342$ Å along the *x* axis and $R_y = 1.712$ Å along the *y* axis. The oxygen anion will have four neighboring Cu ions. From atomic calculations it follows that the Coulomb interaction energy of two electrons equals $I_0 = 17.98$ eV for the O^{1-} anion and $I_0 \sim 13.46$ eV for the O^{2-} anion. The Coulomb interaction of two *d* electrons in the Cu atom can be estimated at $I_{Cu} = 6.26$ [7]. The Coulomb interaction energy V_{AB} of two *p* electrons located on atoms A and B was crudely estimated by the Ohno equation [11], which is used in quantum-chemical calculations by the CNDO method

$$V_{AB}(R_{AB}) = \frac{14.3986}{\sqrt{R_{AB}^2 + c^2}} \text{ (eV)}, \tag{2}$$

where $c = 14.3986/2^{-1}(I_A + I_B)$ and R_{AB} is the internuclear distance between atoms A and B in Å. In the *xy* plane, the O^{1-} anion will have two neighboring Cu ions at the distance R_x and two Cu ions at the distance R_y. It was shown in [12] that the energy $E = ZV - I$ corresponds to the electron pair formation energy in a square-planar lattice with the parameter $m = 2$. It is known that the Coulomb potential in metals is

described by the screened potential $\varphi = q\exp(-\lambda r)/r$. Then, the I and $V(R)$ values should be multiplied by $\exp(-\lambda r)$. If it is taken that the concentration $n \sim 10^{20}$ cm^{-3} for the metal planes of CuO, then $1/\lambda \sim 1$ Å [13]. The diameter of the p shell of the O^{1-} and O^{2-} anions equals, respectively, 2.12 and 2.92 Å. The diameter of the d shell of the Cu atom equals 1.4 Å. If there are holes t in the d shell and holes t_1 in the p shell, the energy $E = kT^*$ takes the form

$$E = t_1 t \times 2(V(R_x)\exp(-R_x) + V(R_y)\exp(-R_y)) - I\exp(-d). \quad (3)$$

In the calculation of the formation temperature T^* of LEPs in the subsystem of O^{1-} anions, the following parameters should be taken: $d = 2.12$ Å, $I = 17.98$ eV, $I_0 = 17.98$ eV, $I_{Cu} = 6.26$ eV, $t_1 = 1$, and $t = 1$. In this case, one obtains $T_0^* = 16138$ K. As the number of holes t in the Cu^{2+} d shell decreases, the temperature T_0^* proportionally decreases, and $T_0^* \sim 0$ at $t = 0.61$. It is not inconceivable that LEPs are also formed in the copper subsystem of the Cu^{2+} ions in the plane. However, as it was noted above, the Cu^{2+} ions occur in the paramagnetic state at $T \sim 300$–400 K, and the superconducting state must be in the plane. The formation temperature T_{Cu}^* of LEPs in the subsystem of Cu^{2+} ions can also be calculated. To do this, one should take $d = 1.4$ Å, $I = 6.26$ eV, $t_1 = 1$, and $t = 1$ in Eq. (3). The formation temperature of LEPs in this case equals $T_{Cu}^* = 23269$ K. With decreasing number of holes t_1 in the O^{1-} p shell, the temperature T_{Cu}^* decreases. At $t_1 = 0.44$, $T_{Cu}^* \sim 0$.

Consider the possibility of the formation of LEPs in the subsystem of O^{2-} anions at the CuO surface without the presence of deposited Cu atoms. CuO is a p-type semiconductor with a band gap width of ~ 0.6 eV. CuO, in which the Cu ions have the d^9 structure, is an antiferromagnet with an effective magnetic moment 0.6 μ_B [10]; that is, $t = 0.6$ in the d shell. In this case, the number of holes in the O^{2-} p shell will equal $t_1 = 0.4$; that is, the electron configurations of oxygen are close to the configuration of O^{2-}. Hence, the following parameters should be taken in Eq. (3): $d = 2.92$ Å, $I = 13.46$ eV, $I_0 = 13.46$ eV, $I_{Cu} = 6.26$ eV, $t_1 = 0.4$, and $t = 0.6$. For this case, the parameter $m < 1$ and $kT^* \sim Em/2$ [7]. At $m \sim 0.5$, Eq. (3) gives $T^* \sim 200$ K. For $t_1 \approx 0.36$, the parameter $T_0^* \sim 0$. From here, it follows that the formation of CDW in the oxygen subsystem at the surface of CuO is unlikely for common values of parameters. A similar situation takes place in the copper subsystem.

The Neel temperature T_N (antiferromagnet–paramagnet transition) for CuO was determined to be 230 K, and a very broad maximum centered at ~ 540 K was observed in the temperature dependence [14]. A reasonable explanation for this fact was given in [15], where an agreement between experimental data and theory was obtained within the model of the formation of Cu^{2+}–Cu^{2+} pairs with a shortened internuclear distance below T_N and an increased distance above T_N. This consideration of the reasons for antiferromagnetism in CuO is confirmed experimentally by the facts that the temperature dependence higher than 700 K of the susceptibility of CuO obeys the Curie–Weiss law and the effective magnetic moment equals 1.9μ_B, which is larger than that for the pure spin state. From here, it follows that the state of Cu ions in CuO at high temperatures tends to decrease its d electron density. In this case, the parameter $I = I_{Cu}$ can be increased from 6.26 to 7–8 eV. Substituting this value into Eq. (3) gives the estimate $T_{Cu}^* \sim 0$. Hence, as the temperature increases up to 700 K and above, the formation of LEPs in the copper subsystem of the boundary CuO plane in the Cu–CuO interface becomes unlikely.

Thus, a crude estimate of the formation temperature of LEPs in the oxygen subsystem at the CuO surface in the Cu–CuO interface gives $T^* \sim 10^4$ K. It was shown in [16–18] that a system of LEPs can pass into a superconducting state [19]. In this model, with regard to the interaction of the nearest neighbors, the area of superconductivity is bounded by the inequality [20] $K < K_c \sim t/\nu$ (where $K = N/B$, N is the number of LEPs, B is the number of sites, t is the hopping integral, and ν is the Coulomb repulsion of LEPs on neighboring sites). At $K > K_c$, the system of LEPs is ordered by a charge density wave. With the assumption of the occurrence of a narrow band at the CuO surface, the value $t \sim 0.4$ eV can be taken for this band [21]. In this case, the critical value $K_c \sim 0.04$ for $\nu \sim 10$ eV. In common bivalent metals, the ratio $N/B \sim 1$ and the concentration of carriers $n \sim 5 \times 10^{22}$ cm^{-3}, whereas the concentration of carriers at $K_c \sim 0.04$ in the Cu–CuO interface should be $n \sim 10^{20}$ cm^{-3} for the formation of a Bose–Einstein condensate. Actually, if the concentration in the interface layer equals $n \sim 1.6 \times 10^{20}$ cm^{-3} and the effective mass of carriers $m^* \sim m_e$, the estimation of the onset temperature of Bose–Einstein condensation gives the value $T_c \sim 1000$ K [22]. The obtained estimate of T_c corresponds to the experimental value.

REFERENCES

1. V. V. Osipov and A. A. Samokhvalov, Fiz. Met. Metalloved. **89**, 43 (2000).
2. V. V. Osipov, I. V. Kochev, and S. V. Naumov, Zh. Éksp. Teor. Fiz. **120**, 1246 (2001) [JETP **93**, 1082 (2001)].
3. T. I. Arbuzova, S. V. Naumov, A. A. Samokhvalov, *et al.*, Fiz. Tverd. Tela (St. Petersburg) **43**, 846 (2001) [Phys. Solid State **43**, 878 (2001)].
4. A. A. Samokhvalov, T. I. Arbuzova, N. A. Viglin, *et al.*, Fiz. Tverd. Tela (St. Petersburg) **41**, 293 (1999) [Phys. Solid State **41**, 262 (1999)].

5. L. V. Gurvich, G. V. Karachevtsev, V. N. Kondrat'ev, Yu. A. Lebedev, V. A. Medvedev, V. K. Potapov, and Yu. S. Khodeev, *Bond-Breaking Energies. Chemical. Ionization Potentials and Electron Affinity* (Nauka, Moscow, 1974), p. 226.
6. S. P. Shubin and S. V. Vonsovskii, Proc. R. Soc. London **145**, 159 (1934).
7. I. I. Amelin, Pis'ma Zh. Éksp. Teor. Fiz. **70**, 24 (1999) [JETP Lett. **70**, 23 (1999)].
8. I. I. Amelin, Zh. Fiz. Khim. **73**, 2274 (1999).
9. I. I. Amelin, in *Proceedings of the 32nd All-Russia Conference on Low Temperature Physics, Section "Superconductivity," Kazan', 2000*, p. 159.
10. V. B. Lazarev, V. V. Sobolev, and I. S. Shaplygin, *Chemical and Physical Properties of Simple Oxides of Metals* (Nauka, Moscow, 1983), p. 8.
11. K. Ohno, Adv. Quantum Chem. **3**, 240 (1967).
12. V. I. Spitsin, G. V. Ionova, S. V. Vonsovskiĭ, *et al.*, *Electron Dynamics and Charge-Ordered Crystals* (Chernogolovka, 1985), p. 121.
13. C. Kittel, *Introduction to Solid State Physics* (Wiley, New York, 1976; Nauka, Moscow, 1978).
14. J. B. Goodenough, *Metallic Oxides* (Pergamon, New York, 1971), p. 145.
15. M. O'Keeffe and F. S. Stone, J. Phys. Chem. Solids **23** (2), 261 (1962).
16. A. Alexandrov and J. Ranninger, Phys. Rev. B **24**, 1164 (1981).
17. I. O. Kulik and A. G. Pedan, Zh. Éksp. Teor. Fiz. **79**, 1469 (1980) [Sov. Phys. JETP **52**, 742 (1980)].
18. I. O. Kulik and A. G. Pedan, Solid State Commun. **45**, 971 (1983).
19. M. Schafroth, S. Butler, and J. Blatt, Helv. Phys. Acta **30**, 93 (1957).
20. K. Kubo and S. Takada, J. Phys. Soc. Jpn. **52**, 2108 (1983).
21. H. M. Plakida, *High-Temperature Superconductors* (Mezhdunarodnaya Programma Obrazovaniya, Moscow, 1996), p. 133.
22. V. L. Ginzburg, Usp. Fiz. Nauk **170**, 619 (2000).

Translated by A. Bagatur'yants

JETP Letters, Vol. 76, No. 3, 2002, pp. 189–193. Translated from Pis'ma v Zhurnal Éksperimental'noĭ i Teoreticheskoĭ Fiziki, Vol. 76, No. 3, 2002, pp. 223–228.

Electronic Properties of New $Ca(Al_xSi_{1-x})_2$ and $Sr(Ga_xSi_{1-x})_2$ Superconductors in Crystalline and Nanotubular States

I. R. Shein, V. V. Ivanovskaya, N. I. Medvedeva, and A. L. Ivanovskiĭ

Institute of Solid-State Chemistry, Ural Division, Russian Academy of Sciences, Yekaterinburg, 620219 Russia

e-mail: shein@ihim.uran.ru

Received June 26, 2002; in final form, July 8, 2002

The band structure of new layered (AlB_2 type) $Ca(Al_xSi_{1-x})_2$ and $Sr(Ga_xSi_{1-x})_2$ superconductors is studied by the first-principle full-potential LMTO method. It has been shown that the superconducting properties of ternary silicides are due to the high density of (Ca,Sr)*d* states at the Fermi level, whereas the growth of T_C in going from $Sr(Ga_xSi_{1-x})_2$ to $Ca(Al_xSi_{1-x})_2$ is associated with the increase in phonon frequencies due to the decrease in atomic masses. Simulations are performed for the electronic properties of hypothetical (11,11) and (20,0) CaAlSi and SrGaSi nanotubes. In going from the crystalline to the nanotubular state, the silicide systems retain metal-like properties. The template and "film rolling" techniques can be used for obtaining silicide nanotubes.

PACS numbers: 74.25.Jb; 71.20.Ps; 73.21.-b

Among new superconductors with a wide range of potential applications in various areas of materials science and technologies, two groups of materials have attracted particular attention in recent years. One of them contains quasi-one-dimensional (1D) nanotubular systems. Their best known representatives are carbon nanotubes [1, 2], for which a superconducting transition has been revealed recently ($T_C \sim 0.55$ K) [3, 4] and theoretically interpreted [5].

The second group of promising superconducting materials comprises quasi-two-dimensional (2D) oxygen-free phases, whose investigations were stimulated by the discovery in 2001 [6] of the critical transition in MgB_2 ($T_C \sim 40$ K). It was found (reviews [7, 8]) that the hole-type $2p_{x,y}$ bands in the planes of graphite-like networks of boron atoms play a decisive role in the mechanism of pairing. This fundamental result determined the main line of the current search for new superconductors, which is performed among layered (AlB_2 type) systems.

It is known that the vast majority of non-carbon nanotubes have been synthesized (and predicted) for substances or compounds that, like carbon, have 2D crystalline modifications (review [9]). Therefore, AlB_2-type phases can in their turn become the ground for creating a new class of inorganic nanotubes that are potential superconductors. This possibility was emphasized in [10], where the structural and energy parameters of a number of nanotubes of MgB_2 and ZrB_2 were simulated by the molecular mechanics MM^+ method. The electronic structure of a series of MgB_2, AlB_2, ScB_2, TiB_2, and LiBC nanotubes and a composite (6,6)AlB_2 and (12,12)MgB_2 tube was investigated in [11].

One of the remarkable recent results is the synthesis of the first representatives of a new class of layered superconductors, ternary $Sr(Ga_xSi_{1-x})_2$ ($T_C \sim 3.5$ K) [12] and $Ca(Al_xSi_{1-x})_2$ ($T_C \sim 7.7$ K) [13] silicides isostructural with the MgB_2 superconductor. Their hexagonal sublattice is composed of alkaline-earth metals (AEM = Ca, Sr), and the graphite-like networks are composed of (Ga, Si) or (Al, Si) atoms. Magnetization and electrical conductivity measurements showed that these silicides are type II superconductors [12, 13].

In this work, we report the results of comprehensive investigations of band structure parameters responsible for the superconducting properties of new AlB_2-type ternary silicides and the results of simulations of their hypothetical 1D modifications, whose electronic properties are analyzed using nonchiral armchair (11,11) and zigzag (20,0) nanotubes.

Crystalline silicides were studied by the scalar relativistic full-potential LMTO method [14, 15]. The $Sr(Ga_xSi_{1-x})_2$ (x = 0.375, 0.5, and 0.625) and $Ca(Al_{0.5}Si_{0.5})_2$ compositions were considered within the framework of 12-atomic supercells. The band structure of nanotubes of the $Sr(Ga_{0.5}Si_{0.5})_2$ and $Ca(Al_{0.5}Si_{0.5})_2$ formal stoichiometry was studied by tight-binding band-structure calculations with matrix elements parameterized according to extended Hückel theory [16].

Energy bands and densities of states (DOS) of silicides are given in Figs. 1 and 2. We will discuss their features using $Ca(Al_{0.5}Si_{0.5})_2$ as an example. Its valence band (VB) is determined by (Al,Si)3*p* states, which form four $\sigma(3p_{x,y})$ and two $\pi(3p_z)$ bands, significantly differing in their dispersion relations $E(k)$. The dispersion $E(k)$ for $3p_{x,y}$ bands reaches a maximum in the $k_{x,y}$

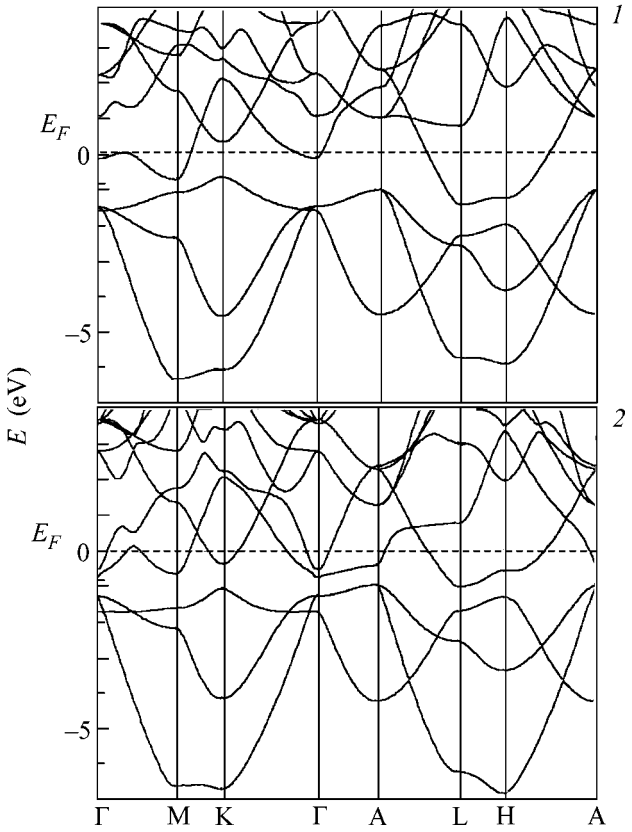

Fig. 1. Energy bands: (*1*) $Ca(Al_{0.5}Si_{0.5})_2$ and (*2*) $Sr(Ga_{0.5}Si_{0.5})_2$. FP LMTO calculations.

(Γ–K) direction. These bands reflects the 2D distribution of (Al,Si)3*p* states in graphite-like networks and form pseudoplanar areas in the k_z (Γ–A) direction. The $2p_{x,y}$ bands make a contribution to DOS over the entire VB width with a maximum at ~2.6 eV below E_F. (Al,Si)p_z states (responsible for interlayer bands) exhibit a significant dispersion in the k_z (Γ–A) direction. The $\sigma(3p_{x,y})$ and $\pi(3p_z)$ bands intersect at the Γ point of the Brillouin zone (BZ). It is important that the (Al,Si)3*p* bands are located below E_F and do not contain hole states as well as those in aluminum diboride, which is isoelectronic to the $Ca(Al_{0.5}Si_{0.5})_2$ silicide (electronic concentration (EC) = 9 electrons per formula unit) and is not a superconductor [7, 8].

The main contribution to the $Ca(Al_{0.5}Si_{0.5})_2$ DOS at the Fermi level $N(E_F)$ is made by the Ca3*d* states (~59%), which determine both the structure of the upper VB edge and the conduction (electronic type) of the given phase. The contributions to $N(E_F)$ of (Al,Si)3*p* states do not exceed ~9 and 10%, respectively, Table 1.

With the general similarity of the band structures of $Ca(Al_xSi_{1-x})_2$ and $Sr(Ga_xSi_{1-x})_2$, their distinctions are associated with a change in the type of intra- and interlayer interactions and are revealed in (i) an increase in the dispersion of the σ and π bands in the A–L–H directions, (ii) the energy separation of these bands at the Γ point, and (iii) the appearance of new occupied states of a mixed Sr4*d*–Ga4*p*–Si3*p* type in the vicinity of the BZ

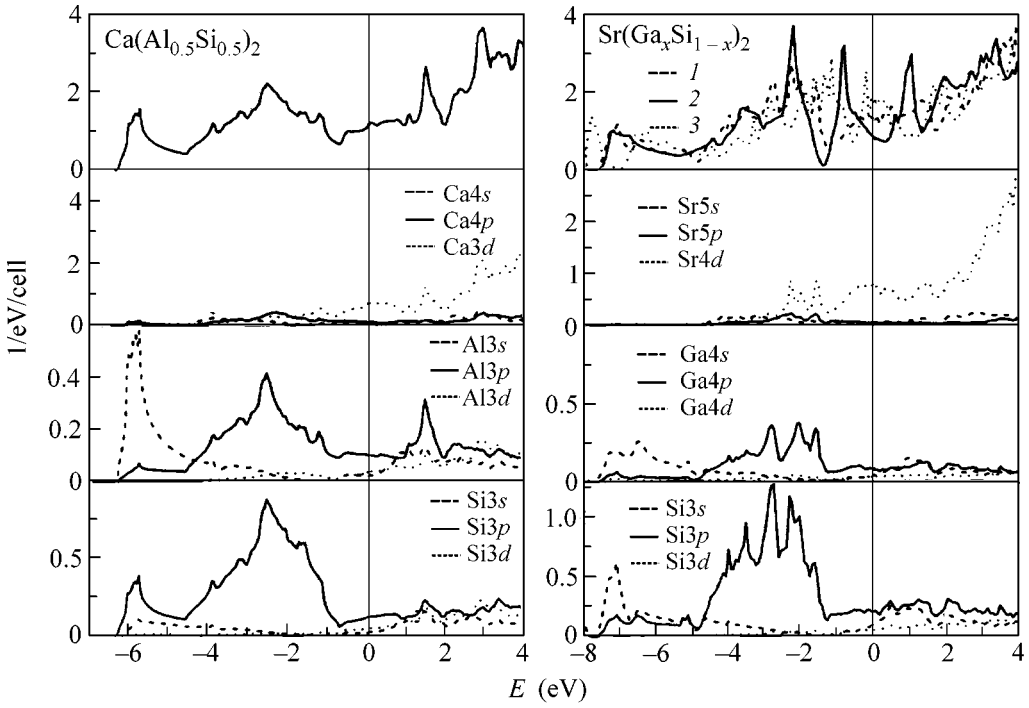

Fig. 2. Total (above) and partial densities of states of $Ca(Al_{0.5}Si_{0.5})_2$ and $Sr(Ga_xSi_{1-x})_2$ for x = (*1*) 0.375, (*2*) 0.5, and (*3*) 0.625.

Table 1. Total and orbital densities of states at the Fermi level ($N(E_F)$, 1/eV) for $Ca(Al_{0.5}Si_{0.5})_2$ and $Sr(Ga_xSi_{1-x})_2$, FP LMTO calculations

Orbital	$Ca(Al_{0.5}Si_{0.5})_2$	$Sr(Ga_xSi_{1-x})_2$		
		$x = 0.375$	$x = 0.5$	$x = 0.625$
Ca(Sr)-*s*	0.030	0.060	0.051	0.059
Ca(Sr)-*p*	0.096	0.041	0.010	0.124
Ca(Sr)-*d*	0.662	0.782	0.516	1.208
Al(Ga)-*s*	0.023	0.033	0.025	0.016
Al(Ga)-*p*	0.101	0.076	0.059	0.297
Al(Ga)-*d*	0.033	0.029	0.015	0.030
Si-*s*	0.023	0.097	0.026	0.010
Si-*p*	0.116	0.208	0.086	0.162
Si-*d*	0.044	0.052	0.034	0.040
Total	1.128	1.378	0.822	1.946

K, Γ, and A points (Fig. 1). The total $Sr(Ga_xSi_{1-x})_2$ VB width increases by ~1.4 eV. The AEM *d* states make the main contribution to $N(E_F)$.

Thus, the band structure of the AlB_2-type silicides has a number of principal distinctions from superconducting MgB_2, which are as follows: (i) the filling of the bonding $p_{x,y}$ bands and the absence of hole σ states, (ii) the growth of covalent interactions between the (Al,Si) or (Ga,Si) and metal layers (due to hybridization of the *p*–*d* states), and (iii) a change in the orbital composition of $N(E_F)$, where the AEM *d* states make the main contribution. The last mentioned fact is characteristic of a wide range of low-temperature metal-like superconducting compounds of *p* and *d* elements (NbN, V_3Si, etc.) [17] for which the values of T_C can be described by the McMillan equation $T_c \approx \langle\omega\rangle \exp\{f(\lambda)\}$, where $\langle\omega\rangle$ is the averaged phonon frequency (inversely proportional to the atomic mass of M) and λ is the electron–phonon coupling constant ($\lambda = N(E_F)\langle I^2\rangle/\langle M\omega^2\rangle$, $\langle I^2\rangle$ is the electron–ion matrix element, $\langle M\omega^2\rangle$ does not depend on mass and is determined by force constants). According to [12, 13], $T_C(Ca(Al_{0.5}Si_{0.5})_2) = 7.7$ K > $T_C(Sr(Ga_{0.37}Si_{0.63})_2) = 3.5$ K. The values of $N(E_F)$ that we obtained for silicides close to each other in composition turn out to be comparable (vary over ~18%) but are in an opposite relationship $N(E_F)(Ca(Al_{0.5}Si_{0.5})_2) < N(E_F)(Sr(Ga_{0.375}Si_{0.625})_2)$ (Table 1). It may be supposed that the higher values of T_C are obtained for the $(Ca(Al_xSi_{1-x})_2)$ silicides, which contain easier atoms, because of the growth of phonon frequencies.

Introducing electron or hole dopants is a widely used technique for modifying the superconducting properties of complex systems, and the result is often predicted based on the rigid-band model [7, 8]. Calculations for $Sr(Ga_xSi_{1-x})_2$ with a variable Ga/Si ratio showed that, as EC increases from 8.75 (for $x = 0.375$) to 9.25 electrons per formula unit ($x = 0.625$), the DOS profile at the Fermi level sharply changes (mainly, on account of the Sr4*d* states, Fig. 2), which results in a nonmonotonic dependence $N(E_F)$ with a minimum at $x = 0.5$. Hence, attempts to optimize the superconducting properties of the $Sr(Ga_{0.37}Si_{0.63})_2$ phase obtained in [12] by its electron doping (at least, up to the

Table 2. Diameters (*D*, Å), total band energies (E_{tot}, eV), Fermi energies (E_F, eV), and interatomic bond indices (COOPs, *e*) for (11,11) and (20,0) CaAlSi and SrGaSi nanotubes. Tight-binding calculations

Nanotube	*D***	$-E_{tot}$	$-E_F$	COOPs***		
				X–*X*	*X*–*M*	*M*–*M*
(11,11)AlSi	25.427		8.450	0.440	–	–
(11,11)GaSi	25.137		8.739	0.451	–	–
(11,11)GaAlSi(I)*	21.028	2403.34	6.492	0.480	0.003	0.181
(11,11)GaAlSi(II)	29.826	2386.62	6.356	0.473	0.034	0.106
(11,11)SrGaSi(I)	20.337	2493.50	6.845	0.493	0.0	0.220
(11,11)SrGaSi(II)	29.937	2479.16	6.863	0.489	0.006	0.178
(20,0)AlSi	26.691		9.046	0.879	–	–
(20,0)GaSi	26.387		9.116	0.884	–	–
(20,0)CaAlSi(III)	22.292	4401.57	6.347	0.894	0.0	0.118
(20,0)CaAlSi(IV)	31.090	4386.73	6.221	0.888	0.0	0.066
(20,0)SrGaSi(III)	21.587	4577.07	6.447	0.917	0.0	0.121
(20,0)SrGaSi(IV)	31.187	4572.45	6.614	0.910	0.0	0.099

* Type of tube configurations: the metal cylinder (II, IV) "outside" or (I, III) "inside" the (AlSi) and (Ga, Si) tubes (Fig. 3).

** Diameters of "pure" (AlSi) and (Ga, Si) tubes and CaSr cylinders for the CaAlSi and SrGaSi nanotubes of various configurations.

*** Bond populations between pairs of atoms: X–X in (AlSi) and (Ga, Si) tubes, M–M in metal tubes, and X–M between these tubes.

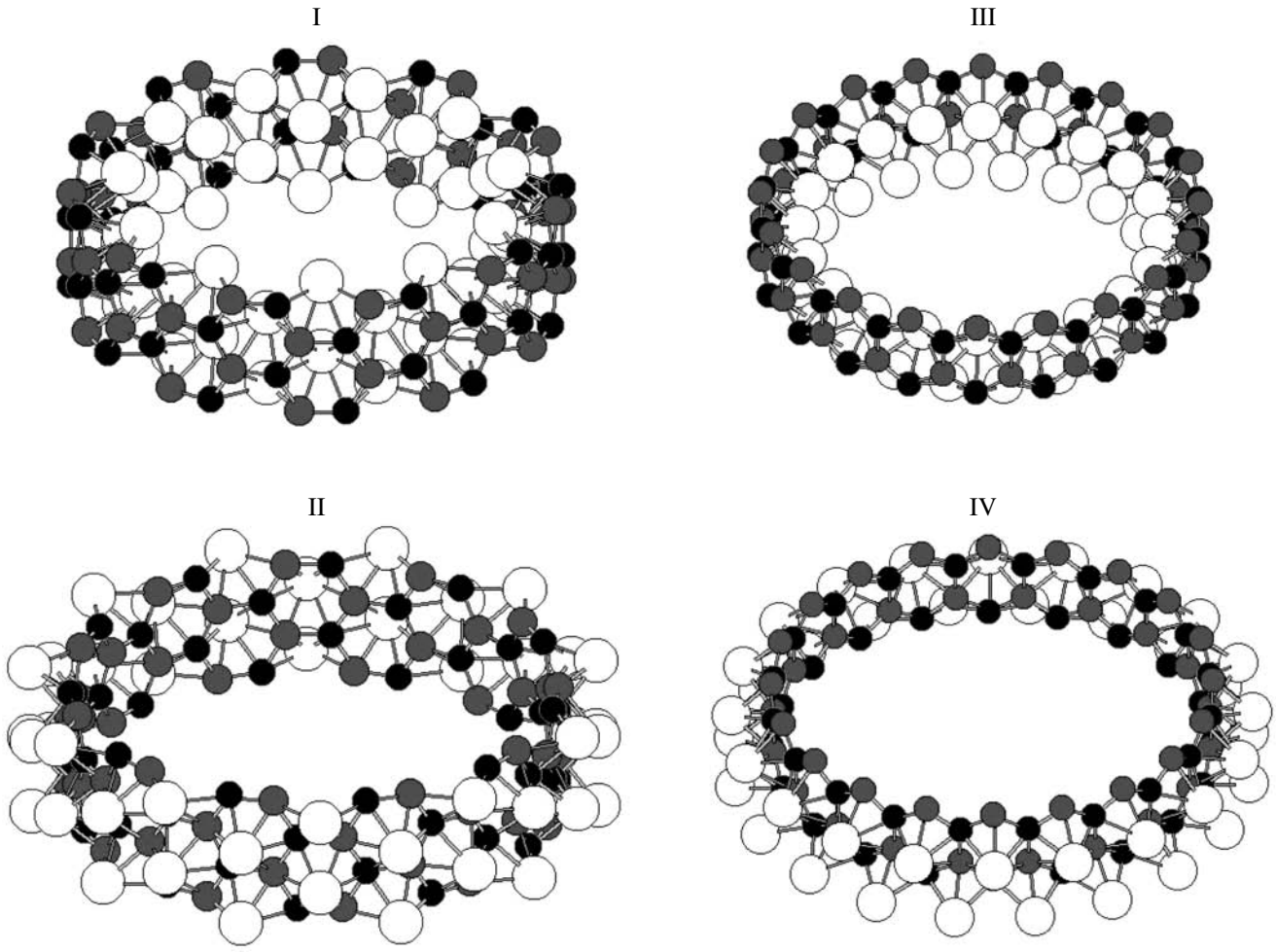

Fig. 3. Models of configurations: (I, II) (11,11) and (III, IV) (20,0) CaAlSi and SrGaSi nanotubes; the metal (Ca, Sr) cylinder is located (I, III) "inside" or (II, IV) "outside" the (Al,Si) and (Ga,Si) tubes.

$Sr(Ga_{0.5}Si_{0.5})_2$ composition) will be unproductive, and the application of the simplified rigid-band model to the description of the given systems is unacceptable.

The tubular forms of silicides were studied using as an example nonchiral (11,11) and (20,0) nanotubes with the formal stoichiometry $Ca(Al_{0.5}Si_{0.5})_2$ = CaAlSi and $Sr(Ga_{0.5}Si_{0.5})_2$ = SrGaSi. The nanotubes consist of two coaxial cylinders formed on the rolling of two neighboring (in the crystal) planar Ca–(AlSi) or Sr–(GaSi) networks. Two possible nanotube configurations were considered: the metal cylinder is arranged either "outside" or "inside" the (AlSi) or (GaSi) tubes (Fig. 3). The interatomic distances were taken equal to the intra- and interlayer distances in the 2D phases [12, 13]. Calculations for the (11,11) and (20,0) nanotubes were performed using 66- and 120-atomic cells; one-layer nanotubes of (AlSi) and (GaSi) monolayers were also calculated (Table 2).

The total DOS of nanotubes presented in Fig. 4 demonstrate that these retain metal-like properties inherent in 2D silicides. However, depending on the geometry and composition of nanotubes, their DOS at the Fermi level sharply change up to the appearance of a pseudogap for the (11,11)SrGaSi nanotube. Estimations of the total band energies (E_{tot}) of nanotube configurations (I–IV, Fig. 3) indicate that the structures containing the metal cylinder "inside" the nanotube of (AlSi) and (GaSi) monolayers are more stable, which can be qualitatively explained by the stronger interatomic bonds for nanotube configurations I and III (Table 2).

An analysis of crystal orbital overlap populations (COOPs) showed that (i) bonds in (AlSi) and (GaSi) nanotubes of CaAlSi and SrGaSi tubes are stabilized with respect to relatively "pure" one-layer tubes through partial Ca⟶(AlSi) and Sr⟶(GaSr) electron transfer; (ii) the main bonds are those in (AlSi) and (GaSi) nanotubes, and comparable bonds are those in Ca and Sr tubes; and (iii) the covalent bonds between coaxial cylinders are very weak. Bonds of certain types depend on the composition and structure of nanotubes. For the tubes of the same type (armchair (11,11) or zig-

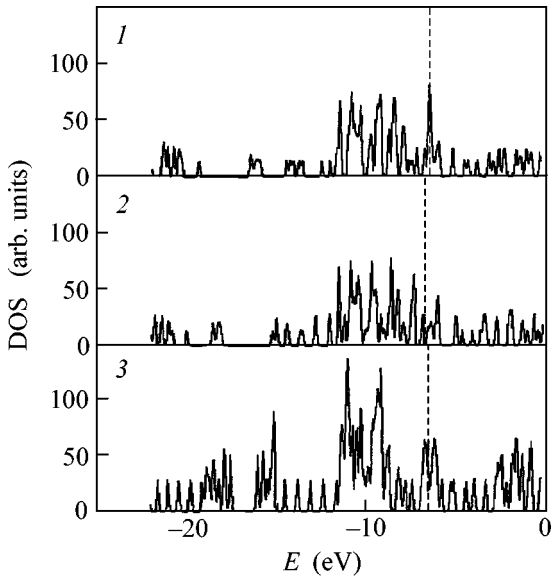

Fig. 4. Total densities of states for (*1*) (11,11) CaAlSi, (*2*) (11,11)SrGaSi, and (*3*) (20,0) SrGaSi nanotubes; tight-binding calculations.

zag (20,0), the X–X and M–M bonds are stronger for the SrGaSi tubes; for armchair (11,11) or zigzag (20,0) nanotubes of a particular composition (CaAlSi or SrGaSi), the bonds in the SrGaSi tubes are significantly stronger, Table 2.

Thus, the analysis of the band structure of new ternary silicides showed that their superconducting properties are associated with the high density of AEM *d* states at the Fermi level, and the growth of T_C in going from $Sr(Ga_xSi_{1-x})_2$ to $Ca(Al_xSi_{1-x})_2$ is evidently due to the growth of the frequencies of the phonon spectrum as a result of the decrease in the atomic masses of the system components. The spectra of $Sr(Ga_xSi_{1-x})_2$ vary nonlinearly as a function of the Ga/Si ratio; an increase in the silicon content (electron doping) will lead (at least, up to Ga/Si = 1) to a deterioration of the superconducting characteristics of the silicide.

Ternary CaAlSi and SrGaSi silicides in the tubular form retain their metal-like properties. The main bonds in nanotubes are those due to "intratubular" interactions, and the "intertubular" bonds are weak as well as those in multilayer carbon nanotubes (of van der Waals type [1, 2]). The configurations of silicide tubes containing AEM layers "inside" the (AlSi) or (GaSi) tubes are more stable; in their turn, the tubes of SrGaSi are more stable than those of CaAlSi.

Experimental data on the synthesis of nanotubes based on AlB_2-type phases have not been reported so far. With regard to the current practice of obtaining inorganic nanotubes (review [10]), it may be expected that the most probable methods for creating CaAlSi and SrGaSi nanotubes will be the template technique (deposition of the surface of carbon nanotube matrices) or the film rolling technique. The first GeSi/Si and InGaAs/GaAs tubes have been obtained recently by this technique [18, 19].

This work was supported by the Russian Foundation for Basic Research, project nos. 01-03-32513 and 02-03-32971.

REFERENCES

1. R. Saito, G. Dresselhaus, and M. S. Dresselhaus, *Physical Properties of Carbon Nanotubes* (Imperial College Press, London, 1998).
2. A. L. Ivanovskiĭ, *Quantum Chemistry in Materials Science: Nanotubular Forms of Substance* (Ural. Otd. Ross. Akad. Nauk, Yekaterinburg, 1999).
3. M. Kociak, A. V. Kasumov, S. Gueron, *et al.*, Phys. Rev. Lett. **86**, 2416 (2001).
4. Z. K. Tang, L. Y. Zhang, N. Wang, *et al.*, Science **292**, 2463 (2001).
5. J. Gonzáles, Phys. Rev. Lett. **88**, 76403 (2002).
6. J. Nagamatsu, N. Nakagawa, T. Muranaka, *et al.*, Nature **410**, 63 (2001).
7. A. L. Ivanovskiĭ, Usp. Khim. **70**, 811 (2001).
8. C. Buzea and T. Yamashita, Supercond. Sci. Technol. **14**, R115 (2001).
9. A. L. Ivanovskiĭ, Usp. Khim. **71**, 203 (2002).
10. L. A. Chernozatonskiĭ, Pis'ma Zh. Éksp. Teor. Fiz. **74**, 369 (2001) [JETP Lett. **74**, 335 (2001)].
11. V. V. Ivanovskaya, N. I. Medvedeva, A. A. Sofronov, *et al.*, J. Mol. Struct.: THEOCHEM (2002) (in press).
12. M. Imai, E. Abe, J. Ye, *et al.*, Phys. Rev. Lett. **87**, 077003 (2001).
13. M. Imai, K. Nishida, T. Kimura, *et al.*, Appl. Phys. Lett. **80**, 1019 (2002).
14. M. Methfessel, C. Rodríguez, and O. K. Andersen, Phys. Rev. B **40**, 2009 (1989).
15. S. Y. Savrasov, Phys. Rev. B **54**, 16470 (1996).
16. R. Hoffmann, *Solids and Surfaces: A Chemist's View of Bonding in Extended Structures* (VCH, New York, 1988).
17. S. V. Vonsovskii, Yu. A. Izyumov, and E. Z. Kurmaev, *Superconductivity of Transition Metals, Their Alloys, and Compounds* (Nauka, Moscow, 1977).
18. S. V. Golod, V. Y. Prinz, V. I. Mashanov, *et al.*, Semicond. Sci. Technol. **16**, 181 (2001).
19. V. Y. Prinz, A. V. Chekhovskiy, V. V. Preobrazhenskii, *et al.*, Nanotechnology **13**, 231 (2002).

Translated by A. Bagatur'yants